DYNAMIC DISTRIBUTED OPTICAL FIBER SENSORS BASED ON DIGITAL OPTICAL COMMUNICATION TECHNIQUES

YAN YAXI

PhD

The Hong Kong Polytechnic University

2021

The Hong Kong Polytechnic University

Department of Electronic and Information Engineering

Dynamic Distributed Optical Fiber Sensors Based on Digital Optical Communication Techniques

Yan Yaxi

A thesis submitted in partial fulfillment of the requirements for the degree of Doctor of Philosophy

June 2021

CERTIFICATE OF ORIGINALITY

I hereby declare that this thesis is my own work and that, to the best of my knowledge and belief, it reproduces no material previously published or written, nor material that has been accepted for the award of any other degree or diploma, except where due acknowledgment has been made in the text.

………………………………………………. (Signed)

…………YAN Yaxi ………………. (Name of student)

To my loving families

and

The memory of my father

Abstract

Dynamic distributed optical fiber sensor (DOFS) appears in the 1970s and has been the subject of remarkable research interest in the last 30 years because of its high sensitivity, long sensing distance, good environmental tolerance, low energy consumption, etc. Signals are extracted as a function of position along the length of the sensing fiber in such dynamic DOFSs, which provides the potential to reduce the cost and the complexity of a dynamic sensing system when a large number of measuring points are required. Dynamic DOFSs are suitable for long-distance and large-scale security tasks, such as leakage detection of oil and gas pipelines, structural health monitoring, perimeter security protection and safety monitoring of communication links. However, the sensing performance of dynamic DOFSs is limited by the bottleneck of the sensing techniques. For example, Rayleigh backscattering noise limits the sensing distance of distributed optical fiber interferometers, and the weak intensity of the backscattering light limits the sensing distance of backscattering light based dynamic DOFSs. Besides, it is difficult to realize wide frequency response and large dynamic range in phase-sensitive optical time-domain reflectometry (φ-OTDR). Moreover, the sensing speed is a problem for dynamic Brillouin optical time-domain analyzer (BOTDA). Inspired by the similarities between the optical fiber communication systems and distributed optical fiber sensing systems, this thesis aims to break the limitations imposed by traditional sensing techniques and thus improve the sensing performance of dynamic DOFSs by applying the advanced digital signal generation and processing techniques used in optical communication systems to distributed optical fiber sensing systems.

First, an ultralong haul unidirectional forward transmission-based distributed optical fiber vibration sensor (DOFVS) is proposed. In this sensing scheme, vibration sensing is implemented by using two fibers that are placed close to each other. A frequency shift optical delay line (FS-ODL) at the far ends of these two fibers is used to loop back the sensing wavelength of the unidirectionally forward transmitted light. At the receiver side, a phase and

polarization diversity coherent receiver is used to retrieve the phase of the continuous-wave light. The location information is obtained by calculating the time delay between two constructed differential phase signals. Thanks to the use of Erbium-doped fiber amplifiers and the elimination of the Rayleigh backscattering noise, over 600 km sensing distance is achieved in this sensing scheme. A lower bound of 5 Hz vibration frequency is detected while the upper bound of the detectable frequency is only limited by the bandwidth of the photodetector and the sampling rate set by the analog to digital converter. Less than 125 m spatial resolution is demonstrated when the vibration frequency is larger than 1 kHz.

Multi-point detection is important for dynamic DOFSs, especially in ultralong haul sensing systems. In order to make the detection of multi-point vibrations easier and reduce the data processing load due to the use of FS-ODL in the above-proposed sensing scheme, a simplified unidirectional forward transmission-based DOFVS is proposed. Loop back configuration is formed by directly splicing the far ends of the two sensing fibers. Location information is obtained by analyzing the null points in the frequency spectrum of the demodulated phase signal. Both K^{th} null frequency determination method and double fast Fourier transform algorithm can be used to determine the null frequency. Location performance of these two methods is investigated in depth. It is experimentally demonstrated that the location errors of single-point vibrations and multi-point vibrations are less than ±100 m and ±200 m over a 500-km sensing range respectively.

Finally, a novel dynamic BOTDA using spectrally efficient frequency division multiplexing (SEFDM) is proposed to overcome the limitation of spatial resolution in orthogonal frequency division multiplexing (OFDM) based BOTDAs due to the requirement of the orthogonality between the symbol duration and subcarrier spacing. In the proposed scheme, the probe signal is composed of SEFDM symbols. The SEFDM symbol is generated by intercepting a time-centralized OFDM symbol, which is mapped by a partial Zadoff Chu sequence. Brillouin gain spectrum is retrieved through channel estimation. Complementary pulse coding is utilized to enhance the signal-to-noise ratio of Brillouin signals. The SEFDM-BOTDA is investigated both

theoretically and experimentally. Intersymbol interference (ISI), which has a strong relationship to the symbol length and the cyclic prefix length, is studied in depth. Three SEFDM symbols with different lengths are used to investigate the sensing performance. Since the orthogonality between subcarriers is violated, the spatial resolution can be largely improved, maintaining a good frequency resolution. 1.294 MHz measurement accuracy is reached over a 10 km sensing range when the spatial resolution is 3.1 m. A dynamic measurement with a vibration frequency of 26 Hz is demonstrated. The use of SEFDM provides higher flexibility for BOTDAs to be used in a wider application area.

Acknowledgements

Time flies. My four-year Ph.D. study is about to end. First, I would like to express my deepest gratitude to Prof. Lu Chao, my supervisor. His invaluable help and generous encouragement helped me overcome the difficulties encountered during my Ph.D. period. His careful guidance led me into the research world of optical fiber communication and sensing. His diligence, persistence and passion for research inspire me not only to do better research but also to keep the enthusiasm of life.

Special thanks should be given to Dr. Guo Changjian, who offered me unconditional help and gave me instructive suggestions during my research process. His critical thinking and profound knowledge in the optical communication area helped me improve the quality of my research work.

Many thanks are given to Dr. Zheng Hua, who helped me to deepen my understanding of Brillouin optical time-domain analysis technique. His expertise in distributed optical fiber sensing impressed me a lot.

I would like to thank Prof. Alan Pak Tao Lau for his useful discussions and suggestions during my research process. His rigorous attitude on research set a good example for me.

I would like to thank Mr. Zhou Gai and Mr. Fan Qirui for their assistance in conducting the forward transmission-based distributed fiber vibration sensing experiment. I would also like to extend my thanks to all the other colleagues in our photonic research center at The Hong Kong Polytechnic University for offering me help during my Ph.D. period. Thanks should be expressed to all of the people I met in Hong Kong Polytechnic University as well. Without them, my Ph.D. life could not be such an enriched and diverse experience.

Last my thanks would go to my beloved family for their loving considerations and always present support all through these years.

Table of Contents

List of Abbreviations

A

AC	Alternating current
ADC	Analog-to-digital converter
AOM	Acousto-optic modulator
ASE	Amplified spontaneous emission
AWG	Arbitrary-waveform generator

B

BCF	Bandwidth compression factor
BFS	Brillouin frequency shift
BGS	Brillouin gain spectrum
BLS	Brillouin loss spectrum
BOTDA	Brillouin Optical Time Domain analyzer
BOTDR	Brillouin Optical Time Domain Reflectometer
BPD	Balanced photodetector
BPF	Bandpass filter
BPS	Brillouin phase spectrum
BPSK	Binary phase shift keying
BT	Bandwidth and observation-time product

C

CP	Cyclic prefix
CW	Continuous wave

D

DAC	Digital-to-analog converters
DAS	Distributed acoustic sensor
DD	Direct detection
DGD	Differential group delay
DC	Direct current
DML	Directly modulated laser
DMZI	Dual MZI
DOFC	Digital optical frequency comb

DOFS	Distributed optical fiber sensing
DOFVS	Distributed optical fiber vibration sensor
DSP	Digital signal processing
DTS	Distributed temperature sensor
DVS	Distributed vibration sensor

E

EDFA	Erbium-doped fiber amplifier

F

FFT	Fast Fourier transform
FRM	Faraday rotation mirror
FS-ODL	Frequency shift optical delay line
FUT	Fiber under test
FWHM	Full width at half maximum

I

I	In-phase
IDFT	Inverse discrete Fourier transform
IF	Intermediate frequency
IM	Intensity modulation
ISI	Intersymbol interference

K

KK	Kramers-Kronig

L

LO	Local oscillator
LSB	Lower sideband

M

MI	Michelson interferometer
MZI	Mach Zehnder interferometer
MZM	Mach Zehnder modulator

O

OC	Optical coupler
OCC	Optical chirp chain
OFDM	orthogonal frequency division multiplexing
OTDR	Optical time-domain reflectometry

P

PAPR	Peak to average power ratio
PBS	Polarization beam splitter
PD	Photodetector
PMD	Polarization mode dispersion
PZT	Piezoelectric transducer
P/S	Parallel to serial

Q

Q	Quadrature

R

RBN	Rayleigh backscattering noise
RF	Radio frequency

S

SA	Slope-assisted
SF	Sweep-free
SBS	Stimulated Brillouin scattering
SEFDM	Spectrally efficient frequency division multiplexing
SNR	Signal to noise ratio
SRS	Spontaneous Raman scattering
SSBI	Subcarriers-to-subcarriers beating interference
SSMF	Standard single-mode fiber
S/P	Serial to parallel

T

TDF	Time delay fiber
TGD-OFDR	Time-gated digital optical frequency domain reflectometry

U

USB	Upper sideband

V

VOA	Variable optical attenuator

W

WDM	Wavelength-division multiplexing

Z

ZC	Zadoff-Chu

#

φ-OTDR	Phase-sensitive optical time-domain reflectometry

List of Figures

List of Tables

Chapter 1

Introduction

In this chapter, an overview of the optical fiber communication technique and distributed optical fiber sensing technique is first given. After that, similarities between optical fiber communication systems and distributed optical fiber sensing systems are introduced. This is followed by a brief review of the research works on dynamic distributed optical fiber sensors (DOFSs) assisted by digital optical communication techniques. Next, the challenges of dynamic DOFSs are introduced. Finally, research motivations and outlines of this thesis are given.

1.1 Overview

With the development of optical fiber technology, optical communication and sensing techniques have experienced tremendous progress over the past decades. In the early 1980s, data transmission was first realized in the multi-mode fiber [1]. However, due to the modal dispersion in the multi-mode fiber, the data transmission rate of early systems was limited to below 100 Mb/s. After that, single-mode fiber operating at 1.3 μm was utilized to solve both the fiber modal dispersion and the chromatic dispersion problem, which largely boosted the transmission speed and extended the transmission distance [2]. Intensity modulation and direct detection (IM/DD) schemes were used in fiber optic communications. IM/DD schemes are simple, cost-effective and are still widely deployed in low-cost optical access networks and short-reach interconnect applications [3]. The silica-based optical fiber has a very low loss of 0.2 dB/km near 1.55 μm (or C band). However, communication in the C band was hindered when operating at a high data rate over a long distance because of the large fiber dispersion and the lack of means to compensate for fiber loss. To improve receiver sensitivity of IM/DD scheme so that loss margin can be increased, homodyne or heterodyne detection, also known as coherent detection, was investigated extensively in the 1980s, mainly because of its high receiver sensitivity obtained by using a local oscillator (LO) at the receiver which essentially enables shot noise limited system performance [4]. However, the invention of Erbium-doped fiber amplifier (EDFA) in 1986 and dispersion compensation fiber has made coherent detection no longer a preferred solution for high data rate long-range optical communication systems [5]. Came to the 1990s, wavelength-division multiplexing (WDM) long-haul optical communication systems with tens of channels in the C-band using simple IM/DD schemes with EDFAs at every 60-80 km enabled a significant increase in transmission capacity per fiber over thousands of kilometers. The per-channel bit rate rapidly increased to 40 Gb/s, where polarization mode dispersion (PMD) would have a significant impact on the signal integrity [6]. In the mid-2000s, further increasing the bit rate of IM/DD systems became very difficult due to PMD and component bandwidth limitations. In this connection, coherent communications have re-surfaced as the technology that can further increase the data rate. Research and development of coherent communications were revived after the telecom bubble in the early 2000s [7]. But this time the focus is on the ability of arbitrary generation, reception and digital processing of optical waveforms to exploit both the amplitude and phase as well as the polarization of an optical signal to maximize transmission capacity. Nowadays, coherent detection and digital signal processing (DSP) have become the defining technology for optical communications.

In a parallel development, optical fiber sensing has attracted great attention in both research and application areas. In the beginning, single-point sensing was realized in optical fibers, where fiber Bragg gratings, fiber interferometers and other specially designed fiber sensor structures were used [8-10]. In single-point fiber sensors, only a short section of fiber can be used to monitor the environmental parameters. However, due to the high cost of optical fiber and related fiber components, it is difficult for fiber sensors to compete with their electronic counterpart unless in applications where electronic solutions do not work well such as in the environment with very high electromagnetic interference.

With the rapid development of optical communication technology, the cost of optical fiber components has dropped significantly. The cost reduction of the optical fiber components and the optical fiber provides the possibility for DOFSs to be extensively studied. In DOFSs, the whole optical fiber is used to obtain the distribution information of external physical parameter variations. Therefore, it is possible for DOFSs to interrogate the characteristics of measurands with spatially resolved information along the sensing fiber. As a result, it can be used to replace hundreds or thousands of sensors. DOFS has advantages like high sensitivity, long detection distance, good environmental tolerance, low energy consumption, etc. In the first few decades of the development of DOFS technology, most research attention was paid to the measurement of slowly varying parameters. These include Raman scattering based distributed temperature sensor (DTS) [11-13], Brillouin Optical Time Domain analyzer (BOTDA) [14-16] and Brillouin Optical Time Domain Reflectometer (BOTDR) [17-19] for distributed sensing of temperature and strain. Because abnormal vibration signals can indicate the fault of infrastructures or the adverse change of structural conditions, driven by the development of oil and gas industries, constructions of infrastructures and geophysical sciences, the demand for DOFS with the capability of dynamic measurement explodes. Therefore, another DOFS, known as dynamic DOFS, has attracted significant interest from researchers worldwide. More and more research effort has been made to improve the sensing performance of such sensing systems in recent years.

1.2 Review of dynamic DOFSs assisted by digital coherent optical communication techniques

Both optical fiber sensing and optical fiber communication are important branches of optical fiber technology. Although optical fiber communication systems and DOFS systems have been developed separately, these two systems actually share a lot of similarities. In a typical optical fiber communication system, the data transmission is realized by modulating the amplitude, phase or polarization of a waveform specially designed for the optical communication channel, which is the optical fiber. At the transmitter side, advanced modulation formats are used for data modulation [20]. At the receiver side, equalization and estimation schemes are used so that the best estimation of phase, amplitude and polarization variation introduced by the transmitter can be realized [21, 22]. In modern optical communication systems, this is typically realized through a polarization diversity coherent receiver [23, 24]. In addition, DSP techniques have been developed to recover phase, amplitude and polarization in the presence of amplified spontaneous emission (ASE) noise introduced by optical amplifier and laser phase noise [7]. All these methods are used to achieve the best transmission performance of optical signals in the optical fiber. In a distributed optical fiber sensing system, the amplitude, phase and polarization of the sensing light is modulated by the change of external parameters such as strain, temperature and pressure at different locations of optical fiber. For example, in the distributed temperature sensor based on Raman effect, the amplitude response of Stoke and anti-Stoke waves will be modified by local temperature along the fiber [25]; in BOTDA, for a given pump and probe wave, the amplitude and phase of the probe signal is a function of both temperature and strain distribution along the fiber [26], while in phase-sensitive optical time-domain reflectometry (φ-OTDR), which is also referred as the distributed acoustic sensor (DAS) or distributed vibration sensor (DVS), the phase of the backscattered signal is modified by local strain for each of the measurement [27]. As a result, a good estimation of amplitude, phase and polarization information of the detected signal will allow us to realize a good sensing system. Therefore, the optical fiber sensing system can be regarded as a special fiber communication system, where the transmission information is generated by the external environment variation. Obviously, it is reasonable to introduce the components and techniques developed for the optical communication system into the sensor system to improve the sensing performance of the dynamic DOFS. A significant amount of research efforts have been put into this area.

Coherent detection was first demonstrated in fiber interferometric sensors to detect phase shift signals in late 1970s, while in fiber interferometers, 3x3 couplers (also known as 120 degree hybrid) based homodyne receiver played the main role. With the development of coherent optical communication, digital coherent detection came out and DSP-based RF receiver as well as 90 degree hybrid phase-diversity homodyne receiver were started to be used. Digital coherent detection was proposed to enable optical communication systems with higher data rate and longer transmission distance, where the signal interferes with an LO so that the phase information of the signal can be extracted by means of DSP. Digital coherent detection has been widely applied in φ-OTDRs for extracting the phase of sensing signal and improve the signal to noise ratio (SNR) of the measurand. Heterodyne detection was early reported in a φ-OTDR in 2010 to enhance the system's detection sensitivity and SNR [28]. In this system, an acousto-optic modulator (AOM) is used to generate pump pulse, and it also shifts the laser frequency. The Rayleigh backscattered signal is then mixed and beat with the LO to produce the electrical output. Later in 2011, the heterodyne detection-based φ-OTDR was improved by using an all polarization-maintaining configuration to eliminate the polarization-induced signal fading and further enhance the SNR [29]. It is demonstrated in [30] that by combining distributed Raman amplification and heterodyne detection, the sensing distance of φ-OTDR can be extended to over 131 km with 8 m spatial resolution. The measurement of the optical phase was first reported by employing the digital coherent detection scheme in φ-OTDR in 2011, where heterodyne detection was applied as well [31]. The amplitude and phase information are sampled and processed in the digital domain. By measuring the optical phase of the Rayleigh backscattering signal, accurate and quantitative measurement of vibration frequency became possible. In the work of time-gated digital optical frequency domain reflectometry (TGD-OFDR) using digital coherent detection [32], it is observed that the measured phase variation trace matches well with the excitation signal, compared with the intensity variation trace obtained using the direct detection. In 2015, G. Tu et al. proposed to apply a statistic calculating algorithm to suppress the measurement uncertainty of optical phase in the heterodyne detection based φ-OTDR. A sensitivity of 200 nε was realized over the 24.61 km sensing range. Homodyne detection based on 90-degree optical hybrid has been proposed to realize the phase measurement of φ-OTDR as well [33, 34]. Both the in-phase (I) and quadrature (Q) components of the backscattering light can be detected. Then the optical intensity and phase of the sensing signal can be obtained using I/Q demodulation. Since the detected electrical signal is in the baseband, high-speed analog-to-digital converter (ADC) is not required. Except for using digital coherent receivers, more recently, the phase retrieval of φ-OTDR using direct detection based on Kramers-Kronig (KK) receiver was demonstrated in [35]. The KK receiver is a newly proposed direct detection scheme that is used in optical fiber communication systems for demodulating the quadrature amplitude modulated signal [36]. It is based on the KK relations, which allows the reconstruction of complex signals through applying Hilbert transform to the single-channel beating signals. Since half of the intensity noise power is removed after applying Hilbert transform to the received signal, 2~3 dB SNR enhancement can be obtained in the KK detection based φ-OTDR.

Digital coherent systems face the polarization induced signal fading problems, which is caused because of the misalignment of the polarization between the signal and the LO at the receiver side. Therefore, polarization diversity is used to solve the polarization-induced signal fading problem in digital optical communication systems. Polarization diversity has been applied in φ-OTDRs as well. The sensing scheme of polarization diversity detection was theoretically and experimentally analyzed in φ-OTDRs in [37]. To mitigate the polarization fading noise, a polarization beam splitter (PBS) was used to separate the optical signals into two orthogonal polarization states. The reference light was launched into the PBS at 45° through adjusting the polarization controller in the reference arm. Two orthogonally polarized signals from the PBS were independently detected by two balanced PDs. Results show that the SNR of the vibration location signal achieved by the polarization diversity receiver is higher than that achieved by the single polarized coherent receiver as the polarization mismatch between the sensing arm and reference arm along the sensing fiber is mitigated by the polarization diversity receiver. A coherent φ-OTDR based on the integrated polarization-diversity coherent receiver and heterodyne detection is also investigated [38]. The amplitude and the phase of the Rayleigh scattering light can be obtained from both polarizations, thus reducing signal fading. More recently, the φ-OTDR using both polarization multiplexing at the transmitter and polarization diversity at the receiver has been investigated [39, 40]. In φ-OTDR, the Rayleigh backscattering process practically is not ideal, which will induce slight polarization crosstalk for the backscattered light from one polarization state to its orthogonal state in each fiber segment (The sensing fiber can be seen as a series of successive fiber segments). As a result, sudden phase variations caused by the polarization crosstalk can appear in φ-OTDRs that only use polarization diversity at the receiver. It is shown that the φ-OTDR appears more sensitive and more reliable by adding polarization multiplexing at the transmitter rather than using polarization diversity at the receiver only, as the effects of polarization can be mitigated completely.

BOTDA is mainly designed for measuring very slow varying temperature and strain due to the need for scanning of probe signal, curve fitting to find Brillouin gain peak and the need of averaging to improve the SNR. Various schemes have been investigated to improve the ability of BOTDAs for dynamic sensing. Digital coherent detection is one of them. Phase demodulation was first realized in BOTDAs using the heterodyne detection scheme in 2010 [41]. Since then, digital coherent detection-based BOTDAs have attracted great research attention. In the early research of coherent BOTDAs, the LO and sub-GHz carriers were simultaneously generated by modulating the phase of the probe light [42-45]. At the receiver, the Brillouin influenced carriers beat with the LO to generate an intermediate frequency (IF) signal, which is then used for phase demodulation. This method is called self-heterodyne detection, which was first proposed in [42]. In BOTDA systems, the maximum usable pump pulse power is limited by modulation instability and spontaneous Raman scattering (SRS), while the maximum usable probe power is restricted by non-local effects [46]. Therefore, coherent detection helps to enhance the SNR of the BOTDA system considerably without the need to increase the pump and probe powers. Results in [42] confirm that the trace using self-heterodyne detection is much cleaner than the trace using traditional direct detection, thanks to the enhanced SNR. Later, researchers from the same group demonstrated that coherent detection-based BOTDAs have the advantage of non-local effect reduction as well [44]. Since multiple subcarriers are generated by phase modulation, the beating between subcarriers leads to coherent and multiple sidebands induced noises, which influences the reconstruction of the Brillouin spectrum. I/Q demodulation was proposed to be employed in coherent BOTDA to reduce the coherent and multiple sidebands induced noises by avoiding high order sidebands using single sideband modulator [47]. The I/Q demodulation is implemented by providing a radio frequency (RF) LO at the receiver side for phase demodulation. In [48], carrier suppressed intensity modulation with the combination of I/Q demodulation was proposed to replace the phase modulation as well. Since the optical carrier is suppressed and much fewer sidebands are generated by intensity modulation, the coherent and multiple sidebands induced noises are greatly reduced. In [49] a complex BOTDA system was validated using coherent detection. Because both the amplitude and phase of Brillouin signals can be retrieved using coherent detection, the Brillouin frequency shift (BFS) estimation accuracy was enhanced by a factor of $\sqrt{2}$. Coherent detection has been widely applied in slope-assisted (SA) BOTDAs, which is a promising approach for fast sensing that can be used to realize dynamic measurement and to extend the linear sensing range [50-52]. SA-BOTDA was proposed by Romeo Bernini in 2009 [53]. By setting the frequency difference between probe and pump at the middle of linear slopes of the Brillouin gain spectrum (BGS), the BFS along the FUT can be detected without frequency scanning. Because the linear bandwidth of the BGS is very narrow, the dynamic range of the traditional SA-BOTDAs is only around 600 $\mu\varepsilon$. However, the Brillouin phase-gain ratio has a wider linear range than either the Brillouin phase spectrum (BPS) or BGS, hence, coherent detection will provide a larger dynamic measurement range. Large dynamic strain measurement with amplitude of 5372.9 $\mu\varepsilon$ was achieved in [50] by using heterodyne detection and multi-slope-assisted technique.

In BOTDA systems, the misalignment of the polarization states between pump and probe will lead to the Brillouin gain fluctuation, which largely degrades the measurement accuracy. To eliminate the polarization-induced Brillouin signal fading and reduce the number of averages, a scheme of polarization-independent BOTDA using balanced detection and orthogonal probe sidebands is proposed [54]. The probe wave composed of the two sidebands with orthogonal polarizations is applied. According to the principle of stimulated Brillouin scattering (SBS), the lower sideband of the probe wave will experience the Brillouin gain process, while the Brillouin loss process for the upper sideband (USB). These two sidebands experience complementary Brillouin response due to the orthogonal polarization state, thus the polarization-dependent fluctuation on time trace can be canceled. Alternatively, the polarization-diversity scheme based on a double orthogonal pump interaction can also be used to suppress polarization fading in BOTDA [55]. The linearly polarized pump pulses are launched into the birefringent material at 45° or 135° with the axis of the differential group delay (DGD) module. After going through the DGD module, relative phase shifts are introduced to two pump sidebands. These two pump waves are made orthogonal by using the

DGD module through properly setting the difference between phase shifts suffered by two pump waves. As a result, the polarization fading can be reduced without requiring any polarization control and averaging. Apart from employing polarization diversity to reduce the polarization-induced Brillouin signal fading, phase and polarization diversity receiver was proposed to reduce the receiver-side polarization fading between LO light and signal light in coherent BOTDAs [56].

Multicarrier signaling technique together with coherent detection has been widely used in BOTDA systems to remove the need for frequency scanning to realize fast sensing signal detection. A scheme of scanning-free BOTDA using ultra-fine digital optical frequency comb (DOFC) as probe signal was proposed [57]. A wideband pulsed DOFC probe generated by orthogonal frequency division multiplexing (OFDM) technique is launched into the FUT, while a single tone pump is introduced from the opposite direction. The multi-tone optical probe signal distributes symmetrically around BFS in a frequency range of 1 GHz. After interacting with the pump pulse, the selected frequency component will be amplified. Therefore, the distributed BFS can be obtained by detecting the amplitude, phase and polarization of each frequency comb line of DOFC. Distributed sensing was experimentally demonstrated with a 51.2 m spatial resolution over a 10 km standard single-mode fiber. The measurement speed of the scanning-free BOTDA can be improved about 100 times compared with the conventional BOTDA. However, due to the poor SNR, beyond hundreds of averaging times are inevitable to enhance the measurement precision. To address this problem, a single-measurement sweep-free BOTDA sensor based on phase detection was proposed [58]. Brillouin phase spectrum of DOFC probe induced by Brillouin interaction is measured using coherent detection in a single acquisition without any frequency scanning and data averaging. Single-measurement BOTDA was achieved in a 10 km long fiber with a response time of 100 μs, which is limited only by the fiber length. Dynamic measurement up to 1 kHz vibration frequency has been demonstrated. OFDM-BOTDA systems based on channel estimation have also been demonstrated using both coherent detection and IM/DD schemes [59-62]. Coherent detection based OFDM-BOTDA using channel estimation was first proposed by J. Fang et al. in [59] and [60]. In these works, a BOTDA system using dual-polarization OFDM signals and polarization diversity coherent detection was demonstrated. Both BGS and Brillouin loss spectrum (BLS) were recorded from USB and lower sideband (LSB) signals, respectively, due to the fact that these two sidebands are modulated orthogonally on two polarizations. The BLS profile was then flipped and combined with the BGS profile to generate an overall BGS. The proposed scheme eliminates the use of frequency scanning, polarization scrambling and averaging, thus has a significantly higher sensing speed compared with conventional BOTDA systems. To further simplify the sensing system, C. Zhao et al. reported an IM/DD BOTDA system based on OFDM signaling to avoid frequency scanning, where only one intensity modulator and single photodetector (PD) are required [61]. Selected binary phase shift keying (BPSK) signals were mapped to a set of subcarriers before Hermitian symmetry was conducted to generate a real-valued signal after inverse discrete Fourier transform (IDFT). In [62], complementary pulse coding techniques were incorporated in the IM/DD based OFDM BOTDA system to further enhance the SNR of the BGS and BPS profile.

1.3 Challenges of dynamic DOFSs

A dynamic DOFS is normally evaluated by the following parameters:

1) Spatial resolution: the smallest spacing magnitude that can be resolved by the sensor
2) Sensitivity: the minimum unit for the measurand that can be detected
3) Measurement accuracy: the deviation between the measurement value and the true value
4) Dynamic range: the largest detectable range of the measurand
5) Sensing distance: the maximum distance that can be reached when other sensing requirements are ensured.
6) Frequency response: the largest range of the dynamic frequency that can be detected

Among all the dynamic DOFS systems developed over the past decades, including distributed optical fiber interferometers and optical scattering based DOFSs, there are many technical hurdles for each already known DOFS technique. Table 1.1 shows the comparisons among different dynamic DOFS and it will be detailly discussed in chapter 2.

Table 1.1. Comparisons among different dynamic DOFS

<table>
<tr><td rowspan="2"></td><td colspan="3">Forward transmission light</td><td colspan="2">Backward scattering light</td></tr>
<tr><td>SI</td><td>MI</td><td>MZI</td><td>φ-OTDR</td><td>BOTDA</td></tr>
<tr><td rowspan="2">Advantages</td><td colspan="3" rowspan="2">• Long sensing distance
• Wide frequency response
• High sensitivity
• Large dynamic range</td><td colspan="2">• High spatial resolution
• Low-frequency detection
• Multiple-point detection</td></tr>
<tr><td>• High sensitivity</td><td>• Large dynamic range</td></tr>
<tr><td rowspan="2">Limitations</td><td colspan="3" rowspan="2">• Nonlinear mapping between measurand and measured parameters
• Low spatial resolution
• Limited sensing distance
• Polarization fading
• Low system stability
• Null frequency problem for SI and MI</td><td colspan="2">• Tradeoff between the spatial resolution and sensing distance
• Tradeoff between the sensing distance and frequency response</td></tr>
<tr><td>• Small dynamic range
• Interference fading</td><td>• Low sensitivity
• Polarization fading
• Low sensing speed</td></tr>
</table>

Although configurations based on the combination of two or three dynamic distributed fiber sensing schemes [63-69] have been proposed to overcome the limitations of individual sensing scheme and the dynamic DOFS has seen tremendous development in recent years with the help of optical communication techniques discussed above, some problems remain to be solved. For example, in real applications such as health monitoring of civil structures like steel bridges, oil and gas pipelines, etc., the repeated loads, corrosion, thermal shocks cause dynamic events with vibration frequency up to MHz. But in other applications such as seismic sensing, crack detection of concrete bridges and railway tunnel monitoring, the vibration frequency of these events is usually in the order of Hz. Therefore, a dynamic DOFS, which has a wide frequency response with a large sensing distance is highly desirable. Moreover, the amplitudes of these vibrations are usually very large, hence, a large dynamic range is required as well.

1.4 Research motivations

The research work in this thesis aims to improve the sensing performance of dynamic DOFSs by applying some advanced modulation and demodulation methods used in digital coherent optical fiber communication systems to distributed optical fiber sensing systems. To be more specific, the research motivations include

- Extend the sensing distance and enlarge the frequency response by using unidirectional forward transmission based distributed optical fiber vibration sensor (DOFVS). Since the light is unidirectionally forward transmitted, the Rayleigh backscattering noise (RBN) problem, which limits the sensing distance of distributed optical fiber interferometers can be solved. Besides, EDFAs can be cascaded to form a chain to compensate the signal loss along propagation, hence, the long range or ultralong range fiber sensing can be easily achieved. Moreover, the vibration event is continuously sampled by the continuous wave light, the upper limit of the frequency response can be largely extended, which is only determined by the performance of the data acquisition device.
- Overcome the tradeoff between spatial resolution and the frequency spacing set by the orthogonality conditions in OFDM BOTDAs by using the spectrally efficient frequency division multiplexing (SEFDM) technique. In SEFDM systems, the orthogonality between subcarriers is intentionally violated. Consequently, the symbol period of SEFDM signals can be much compressed, which means a dynamic BOTDA with high spatial resolution can

be realized while the frequency spacing is maintained.

1.5 Organization of the thesis

This thesis is divided into six chapters, the content of specific chapters is arranged as follows:

In Chapter 1, the connections and similarities between the optical communication and sensing techniques are first summarized. After that, research works on dynamic DOFSs assisted by optical communication techniques are reviewed. This is followed by introducing the challenges that remain to be faced by dynamic DOFSs. Next, the research motivations of this thesis are described. Finally, the thesis outlines are given.

Chapter 2 gives the classifications of dynamic DOFSs and introduces the fundamental principle of each dynamic DOFS technique. First, the sensing principles of distributed optical fiber interferometers, including Sagnac interferometer, Mach Zehnder interferometer (MZI), and Michelson interferometer (MI), are described. Then, the backscattering light-based dynamic DOFS is introduced. The Rayleigh scattering process and the principle of Rayleigh backscattering based dynamic DOFS are first discussed. Next, the Brillouin scattering process, the sensing principles of Brillouin scattering-based fiber sensors, and the principles of dynamic BOTDA techniques are introduced. The pros and cons of each dynamic DOFS technique are given as well.

Ultralong sensing distance is always the pursuit of dynamic DOFS and it is desirable to break the technical bottleneck to develop the ultralong haul dynamic DOFS. In Chapter 3, a novel DOFVS using the unidirectionally forward transmitted light and coherent detection is proposed to realize the ultralong haul sensing. Two fibers that are placed close to each other are used for vibration sensing. Through looping back the unidirectional forward transmitted signal by using a frequency shift optical delay line (FS-ODL) at the far ends of two sensing fibers and using the coherent detection scheme, the external vibration signals can be detected and located. The principle of the phase and polarization diversity coherent receiver is first given. Then, the construction of two differential phase signals and the time delay estimation based location algorithm are elaborated. To investigate the sensing performance under the circumstance of ultralong sensing distance, vibrations with three different frequencies (low, medium and high) are applied at the beginning and end of a 1230 km fiber link as well as the loop center of the fiber link. Less than 125 m spatial resolution is obtained over the 615 km (half of 1230 km) sensing range. Detection of vibrations with frequencies from infrasound (5 Hz) to ultrasound (only limited by the experimental devices) is demonstrated.

In chapter 4, aiming to make the multi-point vibration detection easier and solve the problem of large data processing load, the unidirectional forward transmission-based ultralong DOFVS is further simplified by removing the FS-ODL structure. Two sensing fibers are directly spliced to form a loopback configuration. Due to the loopback configuration, null points appear in the frequency spectrum of demodulated phase signals, which can be used to localize the vibration. There are two methods for determining the frequency of the null point. One directly determines the frequency of K^{th} null point through curve fitting. The other obtains the null frequency through applying a second time fast Fourier transform (FFT) to the frequency spectrum of the demodulated phase signal. The localization performance using these two methods has been compared for both single-point and multi-point vibrations. Results show that the location error of single-point vibrations is less than ±100 m and the location error of multi-point vibrations is less than ±200 m, over a 500-km sensing range.

Due to the orthogonality between subcarriers, the tradeoff between the spatial resolution and subcarrier spacing imposes a fundamental limitation for OFDM-BOTDAs to achieve a high spatial resolution. To address this problem, a novel SEFDM BOTDA is presented in chapter 5. Different from OFDM signals. the orthogonality between subcarriers is violated for SEFDM signals. In that case, the period of the SEFDM symbol can be largely reduced, which in turn improves the spatial resolution significantly. The generation and characteristics of the SEFDM symbol are first elaborated in detail. Then the proposed sensing scheme is theoretically analyzed through simulation. Theoretical analysis of the influence of intersymbol interference (ISI) is conducted by adjusting the lengths of the cyclic prefix (CP) that is used to provide a guard interval to eliminate the ISI from the previous symbol. Finally, the experiment is conducted to study the sensing performance of the proposed SEFDM-BOTDA. Three SEFDM symbols with different lengths are designed to investigate the influence of ISI when different spatial resolutions are required. Results show that a 3.1 m spatial resolution with 1.294 MHz measurement accuracy is achieved over a 10 km sensing range. A dynamic measurement with a vibration frequency of 26 Hz is demonstrated.

In chapter 6, a summary of the works presented in this thesis and suggestions about prospected works are given.

Chapter 2

Sensing principle of dynamic DOFS

In this chapter, various schemes proposed for dynamic DOFS are reviewed. Dynamic DOFS can be classified into two main types. One is the forward transmission light based dynamic DOFS, the other is the backscattering light based dynamic DOFS. The forward transmission light based dynamic DOFS, also known as distributed optical fiber interferometers, are first introduced. Sensing principles of different interferometric structures, including Sagnac interferometer, MZI and MI are described in detail. Next, the mechanism of light scattering is explained. This is followed by introducing sensing principles of two common types of backscattering light based dynamic DOFS: φ-OTDR and dynamic BOTDA. Besides, the advantages and disadvantages of each dynamic DOFS technique are discussed as well.

The reported dynamic DOFSs can be classified as in Figure 2.1. One uses the interferometric technique, including Sagnac interferometer, MZI and MI, to interrogate the vibration and location information carried by the forward transmission light. The other kind of dynamic DOFSs is based on the measurement of backscattering light, which includes DASs/DVSs based on Rayleigh scattering [28, 70-74] and dynamic DOFSs based on Brillouin scattering [53, 75-77].

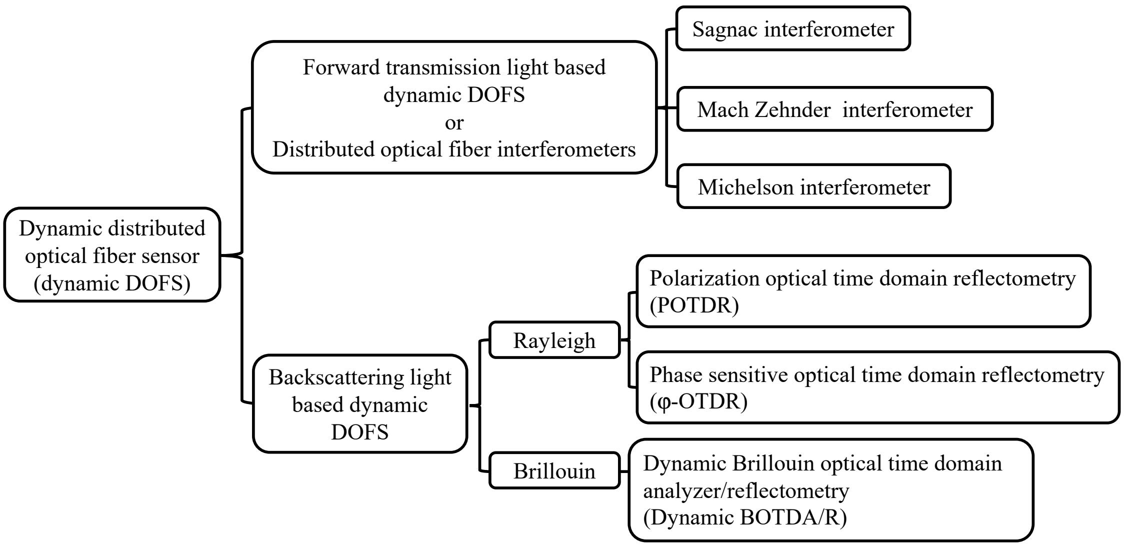

Figure 2.1 Classifications of distributed optical fiber vibration sensors.

2.1 Distributed optical fiber interferometers

2.1.1 Sensing model

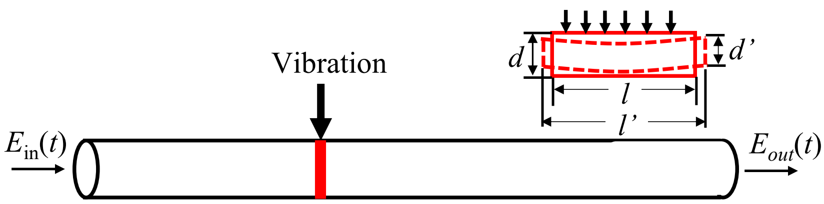

Figure 2.2 The schematic diagram of the fiber pressure induced by the external vibration.

Assuming that there is no vibration applied on the optical sensing fiber, the electrical field of the optical wave after passing through the sensing fiber can be written as

$$E_{out}(t) = A_0 \exp\left[j\omega_0 (t - nL / c) + \varphi_0 \right] \tag{2.1}$$

where A_0, ω_0 and φ_0 are amplitude, angular frequency and phase of the light wave, respectively. n is the refractive index of the fiber core; L is the length of the sensing fiber and c is the velocity of light in vacuum. When an external vibration occurs near the optical sensing fiber, the optical fiber will be stretched or bent, which is schematically shown in Fig. 2.2.

The fiber length, the core refractive index and the core diameter will change, which as a result introduces a phase change into the transmission light. In that case, the output signal light should be written as

$$E_{out}(t) = A_0 \exp\left[j\omega_0 (t - nL / c) + \varphi_0 + \varphi_v \right] \tag{2.2}$$

where φ_v is the external vibration-induced phase change, which has a form as

$$\varphi_v = \Delta l \beta + \Delta \beta l = \beta l \frac{\Delta l}{l} + l \frac{\partial \beta}{\partial n} \Delta n + l \frac{\partial \beta}{\partial d} \Delta d \tag{2.3}$$

where l is the length of fiber affected by the vibration, β is the propagation constant, d is the fiber core diameter. Noting that the change of core diameter caused due to the Poisson effect is neglectable compared to the change of fiber length induced by the strain effect and the change of core refractive index induced by the photo elastic effect, Eq. (2.3) can be simplified as [78]

$$\varphi_v = \frac{\beta l N}{E} (1 - 2\kappa) \left\{ \frac{n^2}{2} (p_1 + 2p_2) - 1 \right\} \tag{2.4}$$

where N is pressure applied to the fiber, which is linearly related to the amplitude of the external vibration, E is the young modulus, is the Poisson ratio, p_1 and p_2 are photo elastic coefficients of the optical fiber. From Eq. (2.4), it is obvious that the phase change is linearly related to the amplitude of the vibration applied to the optical fiber. Therefore, by measuring the phase change of the propagating light, the detection of external vibrations can be realized.

In an optical fiber interferometer, the optical wave is normally divided into two equal-power beams through a beam splitter. One beam serves as the probe light and the other serves as the reference light. After passing through the fiber under test (FUT), the external vibration information is encoded on the phase of the propagating light beams. At the receiver side, these two light beams are coupled together to generate a beating signal, which is then detected by the PD. In an intensity detection based optical fiber interferometer system, the received signal can be expressed as

$$I = I_1 + I_2 + 2\sqrt{I_1 I_2}\cos(\Delta\varphi_0 + \Delta\varphi_v)\cos(\zeta) \tag{2.5}$$

where ζ is the angle between the polarization states of two light beams, I_1 and I_2 are intensities of two light beams, $\Delta\varphi_0$ is the intrinsic phase difference between two light beams and $\Delta\varphi_v$ represents the phase difference between two light beams induced by external vibrations. Normally $\Delta\varphi_0$ is manually set to $\pi/2$ (quadrature point). After removing the direct current (DC) component in Eq. (2.5), the alternating current (AC) signal is linearly related to the phase signal $\Delta\varphi_v$ under the small signal approximation, which means the intensity of the beating signal can be used to identify the external vibration. It should be noted that if $\zeta = \pi / 2$, which means the polarization states of two light beams are orthogonal, the AC signal is zero. This phenomenon is called polarization-induced signal fading. In practical optical fiber systems, the state of polarization (SOP) of the propagation light randomly varies with time because of the changes of fiber birefringence. As a result, the misalignment of the polarization between two beating lights will lead to signal attenuation. Polarization-induced fading is an important factor that influences the sensing performance of distributed optical fiber interferometers [79, 80]. In distributed optical fiber interferometers, the phase of the beating signal can also be directly obtained based on the phase carrier generation method [81, 82] or using a 3×3 coupler at the receiver side [83-85] although the related phase demodulation algorithm is complex. There are three basic structures for distributed optical fiber interferometers, which are Sagnac interferometer, MZI and MI.

2.1.2 Sagnac interferometer

The schematic diagram of a Sagnac interferometer [86] is shown in Figure 2.3. A ring structure is formed by connecting the two outputs of a 2×2 coupler using an optical fiber. The output of a wideband light source is injected into the fiber ring through the 2×2 coupler, being divided into two beams. These two beams transmit along two opposite directions (clockwise and counterclockwise) and interfere with each other at the 2×2 coupler after propagating through the fiber. When an external vibration occurs at a certain point of the sensing fiber, these two counterpropagating beams pass through the disturbance point at different times. Thus, the external vibration-induced phase difference between the clockwise and counterclockwise signals at the receiver side can be written as

$$\varphi_{sr} = \varphi_v(t - n(L_{sr} - R_{sr})/c) - \varphi_v(t - nR_{sr}/c) \quad (2.6)$$

where $\varphi_v(\bullet)$ represents the external vibration induced phase variation, L_{sr} is the length of the Sagnac fiber ring, R_{sr} is the distance between the optical coupler (OC) and the vibration point.

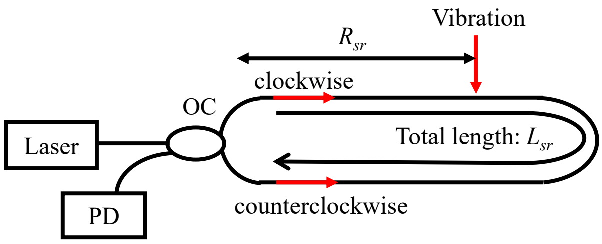

Figure 2.3 The schematic diagram of Sagnac interferometer. PD: photodetector.

Assuming that the vibration signal is a sinusoidal wave with a frequency of f_v, Eq.(2.6) can be written as

$$\begin{aligned}\varphi_{sr} &= \sin[2\pi f_v(t - nR_{sr}/c)] - \sin[2\pi f_v(t - n(L_{sr} - R_{sr})/c)] \\ &= 2\cos[2\pi f_v(t - nL_{sr}/2c)]\sin[\pi f_v n(L_{sr} - 2R_{sr})/c]\end{aligned} \quad (2.7)$$

When , . That means the signal power of some specific frequencies is zero. These frequencies are called the null frequencies, which satisfy

(2.8)

Therefore, in Sagnac interferometers, the vibration position can be determined by the null frequencies as

$$R_{sr} = \frac{\left(L_{sr} - \frac{mc}{nf_{s,null}} \right)}{2} \tag{2.9}$$

Due to the symmetric structure of the ring Sagnac interferometer, only half of the optical fiber is used for sensing [87, 88]. The other half must be shielded from the external environment because environmental variations degrade the sensing performance greatly, especially for long-distance sensing, which makes the system complex. Besides, the cost of the system increases accordingly. To solve this problem, Sagnac interferometers with inline configuration were proposed [89]. Fig.2.4 shows the basic structure of the inline Sagnac interferometer.

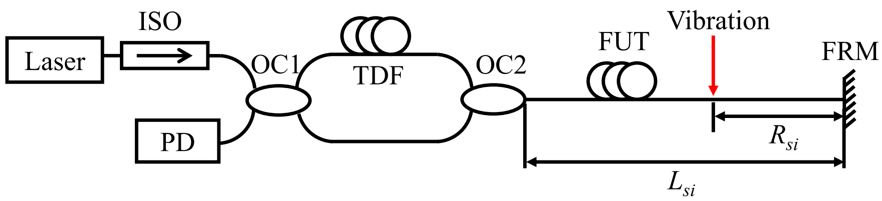

Figure 2.4 The basic structure of the inline Sagnac interferometer. ISO: isolator, PD: photodetector, OC: optical coupler, TDF: time delay fiber, FUT: fiber under test, FRM: Faraday rotation mirror.

There are four possible optical paths for light to go through,

path1: $\mathrm{OC1} \rightarrow \mathrm{TDF} \rightarrow \mathrm{OC2} \rightarrow \mathrm{FUT} \rightarrow \mathrm{FRM} \rightarrow \mathrm{FUT} \rightarrow \mathrm{OC2} \rightarrow \mathrm{TDF} \rightarrow \mathrm{OC1}$

path2: $\mathrm{OC1} \rightarrow \mathrm{TDF} \rightarrow \mathrm{OC2} \rightarrow \mathrm{FUT} \rightarrow \mathrm{FRM} \rightarrow \mathrm{FUT} \rightarrow \mathrm{OC2} \rightarrow \mathrm{OC1}$

path3: $\mathrm{OC1} \rightarrow \mathrm{OC2} \rightarrow \mathrm{FUT} \rightarrow \mathrm{FRM} \rightarrow \mathrm{FUT} \rightarrow \mathrm{OC2} \rightarrow \mathrm{TDF} \rightarrow \mathrm{OC1}$

path4: $\mathrm{OC1} \rightarrow \mathrm{OC2} \rightarrow \mathrm{FUT} \rightarrow \mathrm{FRM} \rightarrow \mathrm{FUT} \rightarrow \mathrm{OC2} \rightarrow \mathrm{OC1}$.

Since the length of the time delay fiber (TDF) is longer than the coherent length of the light source, interference only occurs between the light beams going through paths 2 and 3. In the inline structured Sagnac interferometer, the transmission light goes through the vibration position twice, hence, the external vibration-induced phase change of the interference signal can be written as

$$\begin{aligned}\varphi_{si} &= \varphi_v(t - n(L_{si} - R_{si})/c) + \varphi_v(t - n(L_{si} + R_{si})/c) \\ &\quad - [\varphi_v(t - n(L_{si} - R_{si} + L_d)/c) + \varphi_v(t - n(L_{si} + R_{si} + L_d)/c)]\end{aligned} \tag{2.10}$$

where L_{si} is the length of FUT in the inline structured Sagnac interferometer; L_d is the length of the TDF; R_{si} is the distance from the vibration point to the Faraday rotation mirror (FRM). Similarly, when the vibration signal is a sinusoidal wave with a frequency of f_v, Eq.(2.10) can be written as

$$\begin{aligned}\varphi_{si} &= \sin[2\pi f_v(t - n(L_{si} - R_{si})/c)] + \sin[2\pi f_v(t - n(L_{si} + R_{si})/c)] \\ &\quad - \{\sin[2\pi f_v(t - n(L_{si} - R_{si} + L_d)/c)] + \sin[2\pi f_v(t - n(L_{si} + R_{si} + L_d)/c)]\} \\ &= 4\cos(2\pi f_v n R_{si}/c)\sin(2\pi f_v n L_d/c)\cos(2\pi f_v(t - n(2L_{si} + L_d)/c)\end{aligned} \tag{2.11}$$

Obviously, when $f_v n R_{si}/c = \frac{1}{4} + \frac{m}{2}$, $\varphi_{si} = 0$. Therefore, in the inline structured Sagnac interferometer, the location of vibration is calculated from the null frequencies by

$$R_{si} = \frac{(1 + 2m)c}{4nf_{s,null}} \tag{2.12}$$

Sagnac interferometers have advantages like

1) Zero optical path difference, hence low requirements for the coherence of light sources [90].
2) The use of FRM in the inline Sagnac structure eliminates the influence of polarization-induced signal fading [91, 92].

However, the disadvantages include

1) In the inline structure, the use of the delay fiber introduces the item $\sin(2\pi f_v n L_d/c)$. As a result, the number of null frequencies increases. The existence of null frequencies makes the detection of vibrations with certain frequencies invalid.
2) The existence of the item leads to the signal intensity of low-speed vibrations weakened as the length of the delay fiber is usually less than 1 kilometer.
3) The vibration location is determined by the null frequencies, which highly depends on the frequency property of the external vibration. Besides, in the ring structure, when $R_{sr} \rightarrow L_{sr}/2$,

$f_{s,null} \to \infty$, which means vibrations occurring near the middle point of the fiber ring cannot be located.

4) The Rayleigh backscattering light acts as noise in the interferometer system, which influences the SNR of the received signal and as a result degrades the sensing performance.

2.1.3 Mach-Zehnder interferometer (MZI)

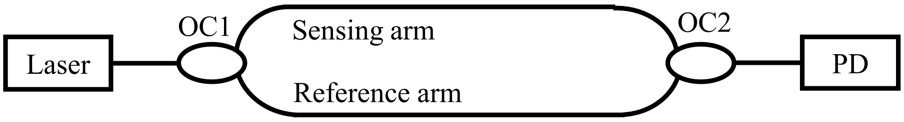

Figure 2.5 The basic structure of the single Mach-Zehnder interferometer. OC: optical coupler; PD: photodetector.

The basic structure of an MZI is shown in Figure 2.5. The output of a laser is divided into two beams by an OC. One serves as the sensing light and the other serves as the reference light. A PD is used to detect the interference signal output from the second coupler. The location information cannot be obtained using the single MZI. As a result, dual MZI (DMZI) architecture [93-96] is usually applied to localize the vibration. Figure 2.6 shows the schematic diagram of a dual MZI with an inline structure.

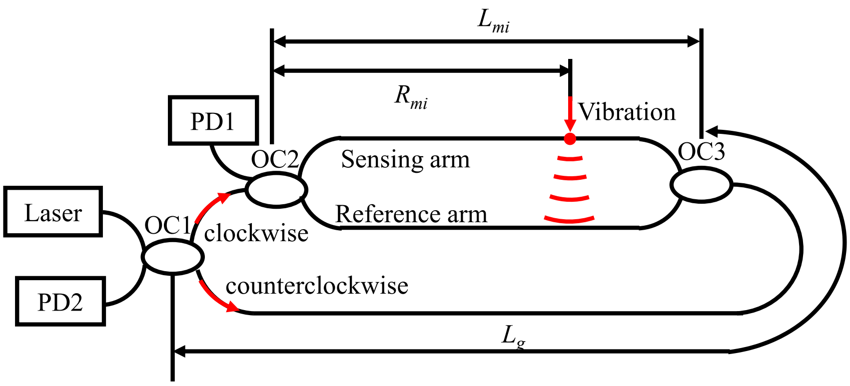

Figure 2.6 The schematic diagram of the dual MZI with inline structure. OC: optical coupler; PD: photodetector.

The laser output is split into two beams by OC1. The upper beam propagates in the clockwise direction. OC2 divides the upper beam into two branches. One beam is sent into the sensing fiber and the other beam is launched into the reference fiber. One port of OC3 outputs the interference signal of these two clockwise light beams, which is finally detected by PD2. The lower beam propagates in the counterclockwise direction, which is divided into two branches by OC3. After passing through the sensing arm and reference arm, these two counterclockwise beams are combined in OC2. PD1 is used to detect the beating signal. Assuming that the fiber length between OC1 and PD2 and the fiber length between OC2 and PD1 are both zero, the phase variations of two interference signals detected by PD1 and PD2 can be written as

$$\varphi_{PD1} = \Delta\varphi_v(t - nR_{mi} / c) + \varphi_{nccw}(t) \tag{2.13}$$

$$\varphi_{PD2} = \Delta\varphi_v(t - n(L_g + L_{mi} - R_{mi}) / c) + \varphi_{ncw}(t) \tag{2.14}$$

where L_{mi} is the length of the sensing fiber; R_{mi} is the fiber length from OC2 to the vibration position and L_g is the length of the guiding fiber from OC3 to OC1. $\Delta\varphi_v(*)$ represents the phase difference between the sensing arm and reference arm caused by the external vibration. $\varphi_{nccw}(t)$ and $\varphi_{ncw}(t)$ respectively represent the phase noise of the counterclockwise signal and the clockwise signal, which are induced due to the laser source linewidth and environmental fluctuations. In DMZI systems, the highly coherent laser is used as the light source, therefore, the carrier phase noise is neglectable compared to the vibration-induced phase change. Besides, under the assumption that the sensing distance is not too long, the background environmental fluctuation is usually slowly varying, which can be regarded as a constant during the period of external disturbance. Thus after removing the constant component, Eq. (2.13) and (2.14) can be simplified as

(2.15)

(2.16)

Obviously, there is a time delay between these two signals as

(2.17)

Therefore, the vibration can be localized by determining the time delay and the location is calculated by

$$R_{mi} = \frac{1}{2}(L_g + L_{mi} - c\tau_{mi} / n) \tag{2.18}$$

In inline MZI structures, a guiding fiber is needed to connect OC1 and OC3. The loss introduced by the guiding fiber reduces the SNR of the output signal. Moreover, the use of the guiding fiber increases the system cost. Therefore, the dual ring MZI structure as shown in Fig.2.7 has been proposed to eliminate the use of guiding fiber [84, 97, 98].

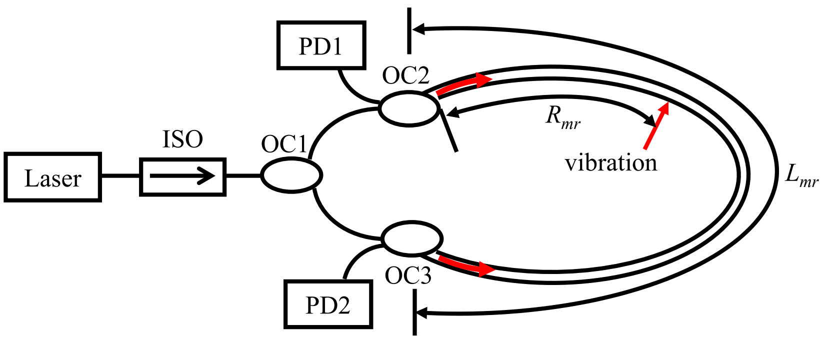

Figure 2.7 The schematic diagram of the dual ring MZI. ISO: isolator; OC: optical coupler; PD: photodetector.

In the dual ring MZI system, fibers are loop back to form a fiber ring. PD1 and PD2 are used to detect the clockwise and counterclockwise interference signals, respectively. Assuming that fiber lengths between OCs and PDs are zero, it is obvious that there is a time delay between two interference signals, which is described as follows:

$$\tau_{mr} = n(L_{mr} - 2R_{mr}) / c \tag{2.19}$$

where L_{mr} is the fiber length of the ring MZI between OC2 and OC3, R_{mr} is the distance from the vibration position to OC2. By calculating the time delay between two signals, the location information can be obtained.

The dual MZI structures have been widely applied in the distributed optical fiber interferometers because of the following advantages

1) The disadvantages of the null frequency-based localization method are overcome because the time delay estimation method is used to locate the vibration. Besides, compared to Sagnac interferometer there is no dead zone of localization.
2) No frequency information of the external vibration is lost as there are no null frequency

points in the spectrum.

However, there are some disadvantages of the dual MZI sensing structure

1) It is hard to make the length of the sensing arm and the length of the reference arm completely equal, therefore, a highly coherent laser is needed, which increases the system cost.
2) In long-distance sensing systems, the environment-induced phase noise will decrease the SNR greatly, which degrades the location accuracy.
3) The polarization-induced signal fading problem.
4) RBN causes SNR degradation.

2.1.4 Michelson interferometer (MI)

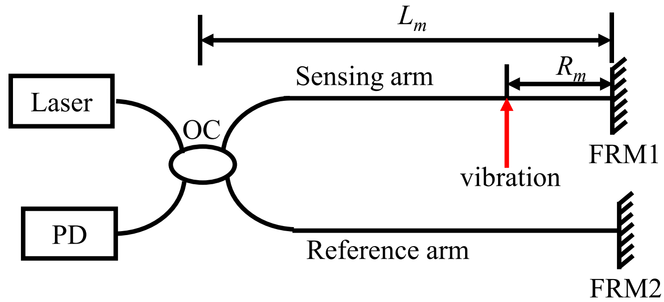

Figure 2.8 The configuration of the Michelson interferometer. PD: photodetector, FRM: Faraday rotation mirror.

The MI is schematically shown in Fig. 2.8. The light source is divided into two beams with the same power by an OC. One beam is launched into the sensing arm and the other is launched into the reference arm. The sensing fiber is placed in the external environment for vibration measurement while the reference arm is isolated from the external environment. Two FRMs are used to reflect the sensing light and reference light at the end of each optical fiber, respectively. Finally, these two reflected beams are combined at the OC, generating the interference signal. The interference signal is detected by a PD. In the MI , the sensing light is modulated by the external vibration twice, hence, the phase change of the interference signal can be written as

$$\varphi_m = \varphi_v(t - n(L_m - R_m)/c) + \varphi_v(t - n(L_m + R_m)/c) \tag{2.20}$$

where L_m is the distance from the OC to FRM1, R_m is the distance from the vibration position to FRM1. Here the fiber length between the OC and the PD is assumed to be zero as well. The location algorithm of the MI is similar to that of the Sagnac interferometer, which is based on the null frequencies. When the vibration signal is a sinusoidal wave with a frequency of f_v, Eq.(2.20) can be written as

$$\begin{aligned}\varphi_m &= \sin[2\pi f_v(t - n(L_m - R_m)/c)] + \sin[2\pi f_v(t - n(L_m + R_m)/c)] \\ &= 2\sin[2\pi f_v(t - nL_m/c)]\cos(2\pi f_v nR_m/c)\end{aligned} \tag{2.21}$$

Obviously, there are a series of null frequency points in the spectrum of the interference signal, which can be used for the vibration localization.

MIs have advantages as

1) Simple sensing structure
2) The use of FRMs helps to solve the polarization-induced signal fading problem.

But the disadvantages include

1) The disadvantages resulted from the null frequency-based localization algorithm. It should be noted that the location of vibration can also be obtained in a dual MI sensing structure by calculating the time delay between two phase signals [99]. Hence, the drawbacks of the null frequency-based localization algorithm can be eliminated. But the location demodulation algorithm is very complex, which is not detailed in this thesis.
2) To ensure the sensing performance, the reference fiber needs to be isolated, which increases the system complexity and cost.
3) The RBN problem.

From the above discussions, it can be concluded that optical fiber interferometers have common advantages like high sensitivity and simple sensing structure. In addition, since light is forward transmitted in the optical fiber, the sensing distance of optical fiber interferometers can easily reach over 100 km without any relay amplification [95], and a record of 320km sensing length was reported for MZI DOFVS [100]. But the bi-directional transmission of light in a single fiber makes distributed optical fiber interferometers suffer from the RBN problem, which limits the sensing distance. Besides, polarization-induced fading is a problem in most distributed optical fiber interferometers. In addition, due to the cosine relationship, the relationship between the vibration signal and the detected signal is not linear unless the signal is very small.

2.2 Scattering light-based dynamic DOFS

2.2.1 Light scattering process in the optical fiber

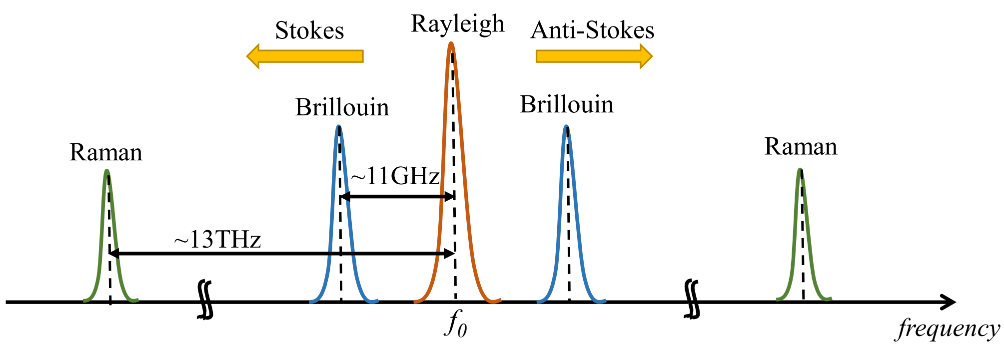

Figure 2.9 Illustration of the light scattering spectrum.

Light scattering is an interactive process between the incident light and the particles in the optical fiber, due to the random density fluctuations within the optical fiber caused by the inherent inhomogeneity of the silica fiber [101]. The incident light is partially scattered in all directions when traveling through the optical fiber. There are three scattering processes in optical fibers known as Rayleigh scattering, Brillouin scattering, and Raman scattering. Among them, Rayleigh scattering is an elastic process, which keeps the energy of photons before and after scattering the same. Brillouin scattering and Raman scattering are inelastic processes, where the energy transfer between the incident photon and the scattering medium shifts the frequency of the scattering light. If the energy of the incident photon is partially absorbed by the medium, the frequency of the scattering light is red-shifted. This process is called the Stokes scattering. Conversely, if the photon absorbs some energy from the medium, the frequency of the scattering light is blue-shifted. This process is called the anti-Stokes scattering. Fig. 2.9 shows the typical spectrum of Rayleigh, Brillouin, and Raman scattering light. Since Raman scattering light can only be used to obtain the temperature information, it is not discussed in this thesis. However, Rayleigh scattering and Brillouin scattering can be used for dynamic sensing. Therefore, in the following sections of this chapter, the sensing principles of Rayleigh and Brillouin scattering-based dynamic DOFSs will be discussed.

2.2.2 Rayleigh scattering and φ-OTDR

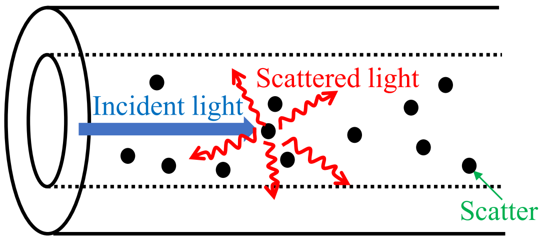

Figure 2.10 The mechanism of Rayleigh scattering in the optical fiber.

The fundamental mechanism of Rayleigh scattering is schematically shown in Fig. 2.10. Rayleigh scattering arises from the elastic collision between the incident light and silica molecules in the optical fiber. An oscillating dipole is induced by the oscillating electromagnetic field when light is incident upon the molecules in the optical fiber. The oscillating dipole then acts as a second-time radiating source, generating the radiation at the same frequency as the incident light [102]. In optical fibers, Rayleigh scattering light is generated in all directions. However, only a small portion of the scattering light is coupled into the fiber and propagated in the backward direction. Rayleigh scattering dominates the fiber loss near the wavelength of 1550 nm, which limits the fiber loss to a lower bound of around 0.2 dB/km.

Based on the backward Rayleigh scattering light, the optical time-domain reflectometry (OTDR) is developed [103]. The configuration of an OTDR is shown in Fig.2.11. In the OTDR system, a pulsed light is injected into the sensing fiber through a circulator. The circulator is also used to output the Rayleigh backscattering light, which is finally detected by a PD. The Rayleigh backscattering wave at position z is a summation of optical waves reflected by the scatters at position z, which can be written as

$$E_{RB}(z) = A_{in}e^{-\alpha z}\sum_{i} r_i e^{j(\phi_i+\varphi_{in})} \tag{2.22}$$

where r_i stands for the reflectivity of the i^{th} scattering center at position z, A_{in} is the amplitude of the incident light, α is the attenuation coefficient of the optical fiber, ϕ_i is the phase shift induced by the i^{th} scatter, φ_{in} is the phase of the incident light.

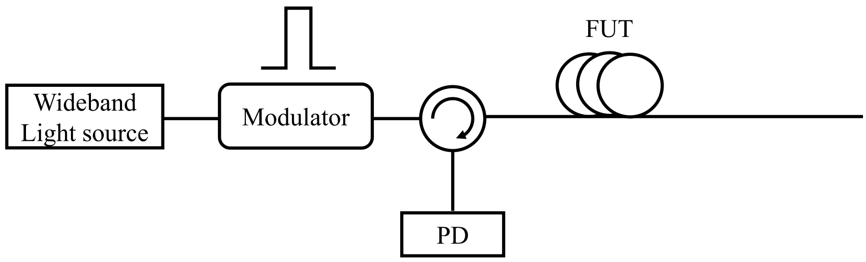

Figure 2.11 The schematic diagram of optical time-domain reflectometry. PD: photodetector; FUT: fiber under test.

In OTDR systems, an incoherent light source is used to generate the probe pulse, hence, the phase of the scattering light $(\phi_i + \varphi_{in})$ changes randomly. Since the size of scatters is much smaller than the wavelength of the probe light, there are a large number of scatters within an interval that is comparable to the wavelength of the probe light at position z. Assuming that the spatial distribution of scatters is uniform and dense, in that case, the phase item in Eq.(2.22) can be ignored. Eq.(2.22) then becomes

(2.23)

where is the Rayleigh backscattering coefficient of the optical fiber at position z. Since the pulsed light is used as the probe, the received optical wave is the summation of Rayleigh backscattering waves from a region determined by the pulse width. Therefore, the electrical field of the Rayleigh backscattering light detected by the PD is expressed as

$$E_r(z) = A_{in} \int_{z}^{z+cW/2n} e^{-2\alpha x}\Re(x)dx \tag{2.24}$$

where W is the width of the light pulse. Due to the incoherent property of the light source, the phase information of the Rayleigh backscattering light is erased, which makes OTDR only capable of detecting the intensity information along the fiber [104-106]. Fig.2.12 shows a typical time-domain OTDR trace.

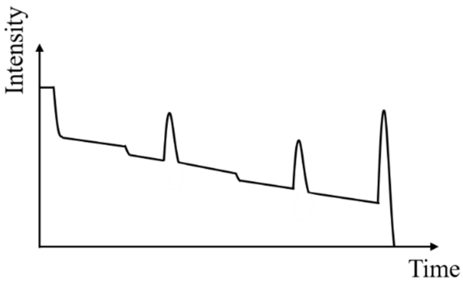

Figure 2.12 An example of the OTDR trace.

Besides the fiber loss caused decreasing tendency of the OTDR signal, there are some sharp slopes or large peaks shown in this signal, which reflects the abnormal conditions along the fiber link, such as splice loss and fiber breakpoint. The location of the abnormal point is determined through time to distance mapping, which is calculated by

$$z = c\Delta t / 2n \tag{2.25}$$

where Δt is the time difference from the beginning of the trace to the abnormal point. Besides, Eq.(2.24) tells that the spatial resolution of an OTDR is determined by the width of the probe pulse as $cW/2n$.

Figure 2.13 The basic structure of a phase-sensitive optical time-domain reflectometry. PD: photodetector; FUT: fiber under test.

To retain the phase information of the Rayleigh backscattering light, φ-OTDR is proposed by replacing the incoherent light source with a highly coherent light source [71]. The basic structure of the φ-OTDR is shown in Fig.2.13. A narrow linewidth laser is employed as the light source. As a result, taking the time evolution into consideration, the backscattered optical wave at position z can be expressed as

$$E_{RB}(z,t) = A_{in}(t)e^{-az}e^{-j[\omega_{in}(t-nz/c)+\varphi_{in}(t-nz/c)]}\sum_i r_i e^{j\phi_i} \tag{2.26}$$

where ω_{in} is the angular frequency of the incident light. Since the spatial distribution of scatters is assumed as uniform and dense, the individual scatters at position z can be modeled as a single scattering center. Consequently, Eq. (2.26) can be written as

$$E_{RB}(z,t) = A_{in}(t)e^{-az}e^{-j[\omega_{in}(t-nz/c)+\varphi_{in}(t-nz/c)]}r(z)e^{j\phi(z)} \tag{2.27}$$

where $r(z)$ is the reflectivity of the scattering center and $\phi(z)$ is the phase shift of the lightwave induced by the scattering center. The electrical field of the Rayleigh backscattering light at the receiver side is then expressed as [70]

$$E_r(z,t) = A_{in}(t)\int_z^{z+cW/2n} e^{-2ax}e^{-j[\omega_{in}(t-nx/c)+\varphi_{in}(t-nx/c)]}r(x)e^{j\phi(x)}dx \tag{2.28}$$

Eq.(2.28) indicates that the Rayleigh backscattering optical waves coming from different scattering centers within the pulse width interfere with each other. Therefore, the φ-OTDR trace presents a jagged interference pattern as shown in Fig. 2.14.

Figure 2.14 An example of the φ-OTDR intensity trace.

The jagged pattern remains unchanged if the optical fiber does not suffer from any external perturbations. However, in case an external vibration occurs at a certain position of the optical fiber, the phase of the light backscattered from the relative position varies due to the vibration-induced change of fiber length, fiber core diameter and fiber reflective index. The intensity of the Rayleigh backscattering light related to the position of disturbance varies accordingly, making φ-OTDRs capable of monitoring external perturbations.

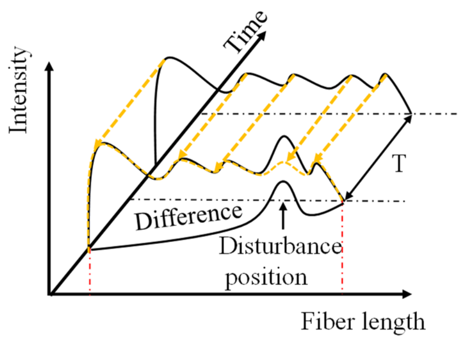

Figure 2.15 The sensing principle of the intensity detection-based phase-sensitive optical time-domain reflectometry.

Figure 2.15 schematically shows the sensing principle of φ-OTDR for locating the external perturbation. By subtracting the intensity traces obtained before and after perturbation, the abnormal point corresponding to the external perturbation can be obtained. The location is calculated using Eq.(2.25), which is the same as OTDRs. The discussion in section 2.1.1 shows that the phase of the light is linearly related to the external vibration while the optical intensity has a nonlinear response to the external vibration. Hence, phase demodulation approaches, including coherent detection, unbalanced Michelson interferometer assisted detection scheme and phase generated carrier demodulation scheme, are widely applied to retrieve the phase of the Rayleigh backscattering signal, and thus the external vibration can be characterized accurately.

Figure 2.16 shows the phase change of the Rayleigh backscattering light when external vibration is applied to the fiber. Due to the external vibration, a phase change is added to the forward propagating probe light. Therefore, the optical wave backscattered from the position right after the vibration point is described as

$$E_{RB}(z,t)=A_{in}(t)e^{-az}e^{-j\Delta\varphi_v(z)}e^{-j[\omega_{in}(t-nz/c)+\varphi_{in}(t-nz/c)]}r(z)e^{j\phi(z)} \quad (2.29)$$

where $\Delta\varphi_v(z)$ is the phase change induced by the external vibration at a certain position of the optical fiber. The backscattering light will go through the vibration point again, picking up the vibration-induced phase change. Assuming that the external vibration varies slowly, and the vibration range is small, the phase change experienced by the backscattering light, therefore, can be seen as the same as that experienced by the probe light, which leads to the received Rayleigh backscattering light scattered from the position right after the vibration point be expressed as

$$E_r(z,t)=A_{in}(t)e^{-j2\Delta\varphi_v(z)}\int_{z}^{z+cW/2n}e^{-2ax}e^{-j[\omega_{in}(t-nx/c)+\varphi_{in}(t-nx/c)]}r(x)e^{j\phi(x)}dx \quad (2.30)$$

By comparing the phase of the light backscattered from the position right before and right after the vibration point. The phase change $\Delta\varphi_v(z)$ can be demodulated.

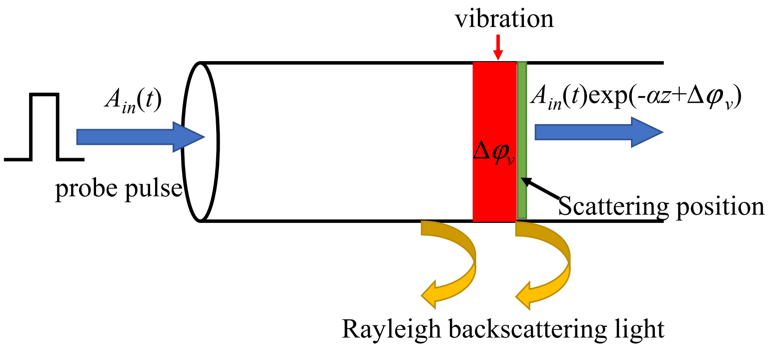

Figure 2.16 Illustration of the phase change experienced by the backscattered light when external vibration occurs.

φ-OTDR has advantages like

1) Simple structure. The single-end transceiver is realized.
2) High sensitivity and capable of quantifying the vibration since the sensing principle is based on measuring the phase change of the Rayleigh backscattering light.
3) Capable of multi-point detection.

However, φ-OTDR also suffers from the following disadvantages

1) The tradeoff between the spatial resolution, sensing distance, and frequency response. The spatial resolution of a φ-OTDR is related to the width of the light pulse used. The narrower the light pulse is, the higher the spatial resolution of the system is. However, a larger intensity of the Rayleigh backscattering signal can be achieved by using a wider pulse, which helps to extend the sensing distance. Besides, in traditional φ-OTDRs, in order to prevent the signal overlapping between two consecutive signal traces, the maximum event sampling rate is limited to $c/2nZ$, which is inversely proportional to the sensing distance Z. Therefore, in long haul sensing systems, the detectable frequency range is largely limited.
2) The Rayleigh backscattering signal has a problem of low signal strength. The SNR of the detected signal is typically very small. This has limited the performance of the sensing system. The sensing distance of the φ-OTDR is usually less than 100 km. Even though in [28], a hybrid amplification scheme was proposed to extend the sensing distance of OTDR based DVS and finally 175km sensing range was obtained with 25m spatial resolution. The system structure is very complex.

2.2.3 Brillouin scattering and dynamic BOTDA

A Spontaneous Brillouin scattering

The Brownian motion of atoms, ions or molecules induces variations in thermodynamic quantities, like temperature or density, which contributes to the fluctuations of the dielectric constant $\Delta\varepsilon$ in the optical fiber. The fluctuations of dielectric constant can be expressed as [107]

(2.31)

where means the density fluctuation of the material and ΔT means the temperature fluctuation. The density fluctuation $\Delta\rho$ is determined by the entropy fluctuation Δs and the pressure fluctuation Δp inside the optical fiber. Moreover, the contribution of temperature fluctuation is neglectable compared to the contribution of density fluctuation, Eq.(2.31) is hence written as [107]

$$\Delta\varepsilon=\left(\frac{\partial\varepsilon}{\partial\rho}\right)_T\left(\frac{\partial\rho}{\partial p}\right)_s\Delta p+\left(\frac{\partial\varepsilon}{\partial\rho}\right)_T\left(\frac{\partial\rho}{\partial s}\right)_p\Delta s \tag{2.32}$$

where the second right-hand side term corresponds to the entropy fluctuations, which is the origin of Rayleigh scattering. The first right-hand side term represents the fluctuations induced by the moving pressure wave (also known as the acoustic wave), which gives rise to the Brillouin scattering. The wave equation of the pressure wave can be described as

$$\frac{\partial^2\Delta\vec{p}}{\partial t^2}-\Gamma\nabla^2\frac{\partial\Delta\vec{p}}{\partial t}-v_a\nabla^2\Delta\vec{p}=0 \tag{2.33}$$

where Γ is the acoustic wave damping factor and v_a is the velocity of the acoustic wave in the optical fiber, which is determined by

$$v_a=\sqrt{\frac{K_s}{\rho}}=\sqrt{\frac{1}{C_s\rho}} \tag{2.34}$$

where ρ is the density of the fiber material, K_s is the bulk modulus and C_s is the adiabatic compressibility. A solution of Eq.(2.33) can be expressed as

$$\Delta\vec{p}=Q_0\exp[i(\vec{q}\cdot\vec{z}-\Omega_a t)]+c.c. \tag{2.35}$$

where Q_0 and Ω_a are the amplitude and angular frequency of the acoustic wave, respectively. $\vec{q}$ is the wavevector of the acoustic wave. *c.c.* represents conjugate complex. The electrical field of the light injected into the optical fiber can be described as

(2.36)

where represents the electric field of light wave, is the wavevector of the light wave. The evolution of the light wave propagating in the optical fiber can be described by a perturbed wave equation derived from the Maxwell equations as

$$\nabla^2\vec{E}-\frac{n^2}{c^2}\frac{\partial^2\vec{E}}{\partial t^2}=\mu_0\frac{\partial^2\vec{P}}{\partial t^2} \tag{2.37}$$

where μ_0 is the magnetic permittivity in the vacuum, $\vec{P}$ is the polarization field induced by the dipole, which is influenced by the electrical field. Since the spontaneous Brillouin scattering is a linear process, the polarization field is linearly proportional to the electrical field as

$$\vec{P}=\Delta\varepsilon\vec{E} \tag{2.38}$$

According to Eq. (2.32)., the polarization field influenced by the acoustic wave can be expressed as

$$\vec{P}=\varepsilon_0\left(\frac{\partial\varepsilon}{\partial\rho}\right)\left(\frac{\partial\rho}{\partial p}\right)_s\Delta\vec{p}\vec{E}=\varepsilon_0\gamma_e C_s\Delta\vec{p}\vec{E} \tag{2.39}$$

where ε_0 is the dielectric constant in vacuum, γ_e is the electrostrictive constant. From Eq.(2.35), Eq. (2.36), Eq. (2.37) and Eq. (2.39), we can derive the wave equation that describes the spatial and time evolution of the spontaneous Brillouin scattering as

$$\nabla^2\vec{E}-\frac{n^2}{c^2}\frac{\partial^2\vec{E}}{\partial t^2}=-\frac{\gamma_e C_s}{c^2}\begin{Bmatrix}(\omega_{in}-\Omega_a)^2 A_{in}Q_0^*\exp[i(\vec{k}-\vec{q})\cdot\vec{z}-i(\omega_{in}-\Omega_a)t]\\+(\omega_{in}+\Omega_a)^2 A_{in}Q_0\exp[i(\vec{k}+\vec{q})\cdot\vec{z}-i(\omega_{in}+\Omega_a)t]\end{Bmatrix}+c.c. \tag{2.40}$$

Eq. (2.40) indicates that due to the influence of the acoustic wave, the frequency of the Brillouin scattering light is either downshifted or upshifted. The first right-hand side term of Eq. (2.40) refers to the Stokes component, and the second right-hand side term of Eq. (2.40) refers to the anti-Stokes component. From Eq.(2.40) we can see that momentum and energy conservations are satisfied during the Brillouin scattering process. Fig. 2.17(a) schematically illustrates the generation process of the Stokes spontaneous Brillouin scattering light. The generation of the Brillouin scattering light requires the satisfaction of strict phase-matching conditions as shown in Fig. 2.17(b), which can be written as

(2.41)

$$\overrightarrow{k_b} = \vec{k} - \vec{q} \tag{2.42}$$

where ω_b and k_b are angular frequency and wavevector of the Brillouin scattering lightwave, respectively.

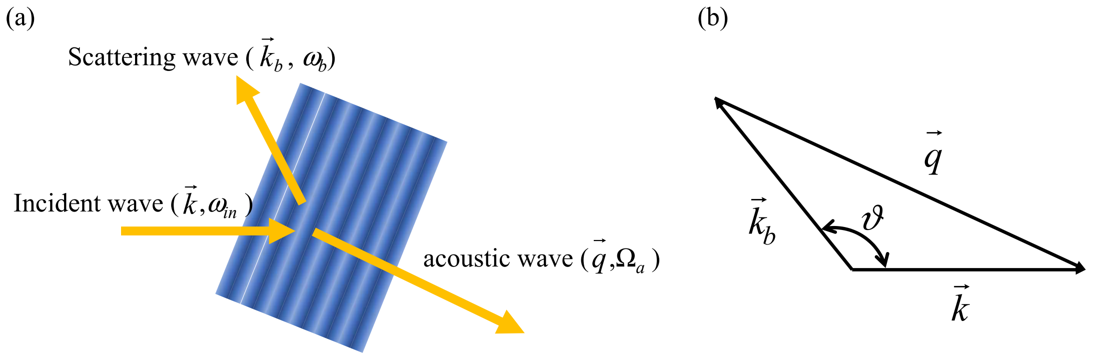

Figure 2.17 (a) The generation process of the stokes wave through Brillouin scattering, (b) the phase-matching condition.

Since both the light wave and the acoustic wave satisfy the dispersion relations as

$$\left|\overrightarrow{k_b}\right| = \omega_b \frac{n}{c}, \tag{2.43}$$

$$\left|\vec{k}\right| = \omega_{in} \frac{n}{c}, \tag{2.44}$$

$$\left|\vec{q}\right| = \frac{\Omega_a}{v_a} \tag{2.45}$$

and the speed of the acoustic wave is much smaller than that of the light wave, we have the approximation as

(2.46)

Then, referring to Fig. 2.17, the momentum conversation can be expressed as

(2.47)

where   is the angle between the incident light and the scattering light. From Eq. (2.45) and

Eq.(2.47), the angular frequency shift of the Brillouin Stokes component is derived as

$$\Omega = \omega_{in} - \omega_b = 2v_a \left|\vec{k}\right| \sin(\vartheta / 2) \tag{2.48}$$

In optical fibers, the light propagates either forward or backward, which means the angle ϑ can only be valued as π or 0. According to Eq.(2.48). when $\vartheta=0$, Ω = 0, which means there is no Brillouin scattering light. The Brillouin scattering light occurs when $\vartheta=\pi$, and the corresponding angular BFS is given by

$$\Omega_B = 2\pi \upsilon_B = 2v_a \left|\vec{k}\right| = \frac{2n\omega_{in}v_a}{c} \tag{2.49}$$

where υ_B is the BFS of the optical fiber. The typical BFS of light in the C-band is around 11 GHz.

The spontaneous Brillouin scattering process can be simplified as the interaction between the incident light and the moving acoustic wave. At room temperature, elastic vibrations of molecules make the fiber density periodically modulated, resulting in the generation of the acoustic wave. The motion of the acoustic wave leads to the moving modulation of the refractive index, which forms a moving Brillouin grating in the optical fiber. Due to the Doppler effect, the Stokes light reflected by the Brillouin grating is downshifted in frequency as the incident light and the acoustic wave propagate in the opposite direction. From the point of quantum mechanics, Brillouin scattering can be seen as a process that a pumping photon is annihilated to generate a Stokes photon and an acoustic phonon.

B. Stimulated Brillouin scattering (SBS)

With the increase of the power of the incident light, the intensity of the Brillouin scattering light increases accordingly. The Brillouin scattering light will interfere with the incident light, forming an interference light field. All the dielectric materials, such as optical fiber, have a property called electrostriction. Electrostriction in the optical fiber is a process that the force formed by the electrical field of the interference light drives the molecules moving toward regions of a high electric field, so as to maximize the potential energy. Due to the influence of electrostriction, the density fluctuation in the optical fiber is intensified, which in turn will stimulate the generation of the acoustic wave. Stronger acoustic waves make the intensity of the Brillouin scattering light strengthened. Furthermore, stronger Brillouin scattering light leads to stronger interference and stronger electrostriction. Therefore, in the stimulation process, the Brillouin scattering light is continuously amplified until a dynamic balance is established between the incident wave (usually called the pump wave), the Brillouin scattering wave (usually called the signal wave) and the acoustic wave. Fig. 2.18 shows the cycle of the stimulated Brillouin scattering process when Stokes light is generated [108].

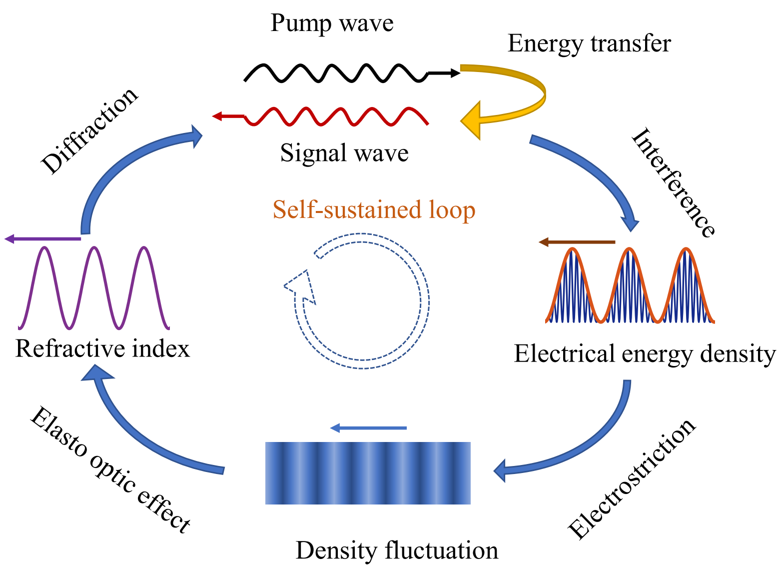

Figure 2.18 the schematical diagram of the stimulated Brillouin scattering process.

There are two Stimulated Brillouin processes in the optical fiber known as the SBS generation and the SBS amplification. Figure 2.19 depicts these two processes. In the SBS amplification process, a weak signal is injected into the fiber as the probe wave. The frequencies of the probe, pump and acoustic waves satisfy the energy conservation condition set by Eq. (2.41) while the wavevectors of probe, pump and acoustic waves satisfy the momentum conservation condition set by Eq. (2.42). Therefore, in Stokes process, the power of the pump light is transferred to the probe light through the SBS, making the intensity of probe wave amplified. However, in the SBS generation process, the probe wave is removed. The Brillouin scattering lightwave initially generated by the thermal motion of phonons in a small region of the optical fiber serves as the probe wave. The Brillouin scattering lightwave is gradually amplified through the SBS process then. It should be noted that in SBS generation process, the frequency difference between the probe wave and pump wave equals to the BFS of the optical fiber. In both processes, the electrical field of the pump wave $\overrightarrow{E_p}$ and the probe wave $\overrightarrow{E_s}$ can be expressed as

$$\overrightarrow{E_p} = e_p A_p(z,t)\exp[j(\omega_p t + k_p z)] + c.c. \tag{2.50}$$

$$\overrightarrow{E_s} = e_s A_s(z,t)\exp[j(\omega_s t + k_s z)] + c.c. \tag{2.51}$$

where e_p and e_s represent the polarization states of the pump and the probe waves, respectively. For simplicity, e_p and e_s are set as 1. $A_p(z,t)$ and $A_s(z,t)$ are slow-varying amplitudes of the pump wave and probe wave, respectively. ω_p and ω_s are angular frequencies of the pump wave and probe wave, respectively. k_p and k_s are wavevectors of the pump wave and probe wave, respectively.

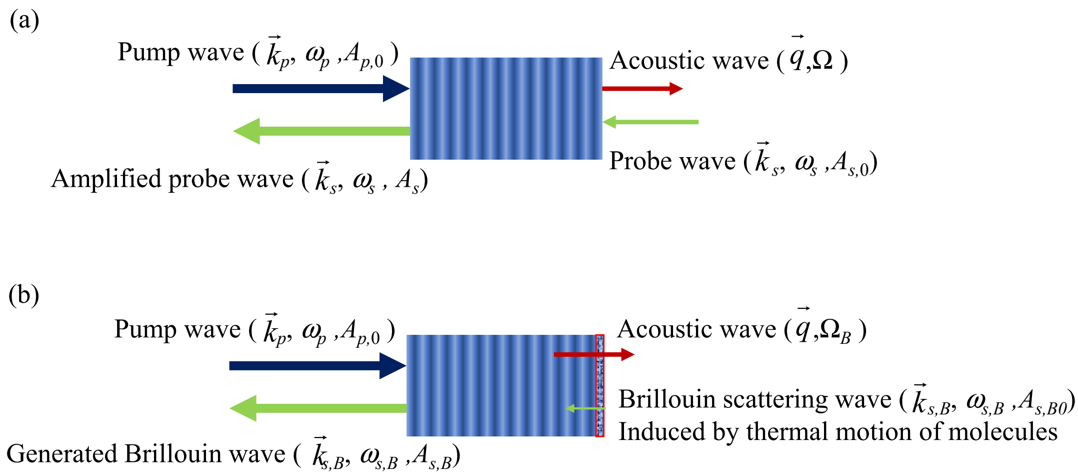

Figure 2.19 Illustration of (a) the stimulated Brillouin scattering amplification process and (b) the stimulated Brillouin scattering generation process.

The acoustic wave can also be described as

$$\Delta p(z,t) = Q(z,t)\exp[j(\Omega_a t + qz)] + c.c. \tag{2.52}$$

where $Q(z,t)$ is the amplitude of the acoustic wave. The spatial and temporal evolution of the acoustic wave under the influence of the driving force induced by electrostriction effect can be written as

$$\frac{\partial^2(\Delta p)}{\partial t^2} - \Gamma\nabla^2\frac{\partial(\Delta p)}{\partial t} - v_a^2\nabla^2(\Delta p) = \nabla \cdot f_d \tag{2.53}$$

where f_d is the driving force that is determined by

$$f_d = -\frac{1}{2}\varepsilon_0\gamma_e\nabla^2\left\langle\left|\overrightarrow{E_f}\right|^2\right\rangle \tag{2.54}$$

And

$$\overrightarrow{E_f} = \overrightarrow{E_p} + \overrightarrow{E_s} \tag{2.55}$$

Since SBS is a nonlinear process, the spatial and temporal evolutions of the pump wave and the probe wave are described as

$$\nabla^2\overrightarrow{E_p} - \frac{n^2}{c^2}\frac{\partial^2\overrightarrow{E_p}}{\partial t^2} = \mu_0\frac{\partial^2\vec{P}_{NL,p}}{\partial t^2} \tag{2.56}$$

$$\nabla^2\overrightarrow{E_s} - \frac{n^2}{c^2}\frac{\partial^2\overrightarrow{E_s}}{\partial t^2} = \mu_0\frac{\partial^2\vec{P}_{NL,s}}{\partial t^2} \tag{2.57}$$

where $\vec{P}_{NL}$ is the polarization field induced by the nonlinear process, which has a general form as

(2.58)

Through respectively replacing , , and Δp in Eqs. (2.53-57) by Eq.(2.50), Eq.(2.51) and Eq.(2.52), we can derive the three-wave coupling equations of the SBS as

$$\frac{\partial A_p(z,t)}{\partial z} + \frac{1}{v_g}\frac{\partial A_p(z,t)}{\partial t} = \frac{1}{2} i g_2 A_s(z,t) Q(z,t) \tag{2.59}$$

$$\frac{\partial A_s(z,t)}{\partial z} - \frac{1}{v_g}\frac{\partial A_s(z,t)}{\partial t} = -\frac{1}{2} i g_2 A_p(z,t) Q^*(z,t) \tag{2.60}$$

$$\frac{\partial Q(z,t)}{\partial t} + \Gamma_A Q(z,t) = i g_1 A_p(z,t) A_s^*(z,t) \tag{2.61}$$

$$\Gamma_A = i\frac{\Omega_B^2 - \Omega_a{}^2 - i\Omega_a\Gamma_B}{2\Omega_a} \tag{2.62}$$

where v_g is the group velocity of light, $\Gamma_B = \Gamma q^2$ is the acoustic damping coefficient, λ_p is the pump wavelength. The angular BFS $\Omega_B = 2\pi\upsilon_B = 2\pi(2nv_a/\lambda_p)$. From Eq.(2.62), we have $\Gamma_A = \Gamma_B/2$ when $\Omega_a = \Omega_B$. g_1 and g_2 are the electrostrictive and elasto-optic coupling constants, respectively. $g_1 = \varepsilon_0\gamma_e q^2$ and $g_2 = \gamma_e\omega_p / cn\rho_0$, ρ_0 is the average density of the fiber material.

Let us consider the acoustic wave first. Assuming that the pump light is a rectangular pulse with a width of W_p and peak power of $A_{p,0}$, the probe light has a constant power as $A_{s,0}$ and the amplitude of the acoustic wave is zero at the initial time. From Eq. (2.61) and Eq. (2.62), the time evolution of the acoustic wave at a certain position can be solved as

$$Q(\Omega_a, t) = \begin{cases} \dfrac{i g_1 A_{p,0} A_{s,0}^*}{\Gamma_A}[1 - \exp(-\Gamma_A t)], & 0<\mathrm{t} \le W_p \\ \dfrac{i g_1 A_{p,0} A_{s,0}^*}{\Gamma_A}\exp(-\Gamma_A t)[\exp(\Gamma_A W_p) - 1], & \mathrm{t}>W_p \end{cases} \tag{2.63}$$

Eq. (2.63) tells us that the acoustic wave is stimulated and strengthened over time when the pump light interferes with the probe light. However, the stimulated acoustic wave decays with time when pump light disappears, and the intensity of the acoustic wave decays exponentially with time as

(2.64)

where τ_A is the average lifetime of the acoustic phonon, which has a relationship with the acoustic damping coefficient as

$$\tau_A = \frac{1}{\Gamma_B} \tag{2.65}$$

When the interaction time between the pump light and the probe light is long enough, the acoustic wave is in a steady state. As a result, the temporal derivative of the amplitude of the acoustic wave is approximated to zero.

Now we consider the steady state of Brillouin scattering process, which is reasonable as in real traditional Brillouin scattering-based distributed optical fiber sensors, the width of pump pulse is usually longer than the lifetime of the acoustic phonon, then temporal derivatives in Eqs. (2.59-61) become zero. Eqs. (2.59-61) can be simplified as

$$\frac{\partial A_p(z,t)}{\partial z} = \frac{1}{2} i g_2 A_s(z,t) Q(z,t) \tag{2.66}$$

$$\frac{\partial A_s(z,t)}{\partial z} = -\frac{1}{2} i g_2 A_p(z,t) Q^*(z,t) \tag{2.67}$$

$$\Gamma_A Q(z,t) = i g_1 A_p(z,t) A_s^*(z,t) \tag{2.68}$$

From Eq. (2.68) we can easily get the expression of the acoustic wave as

$$Q(z,t) = \frac{i g_1(z) A_p(z,t) A_s^*(z,t)}{\Gamma_A(z)} \tag{2.69}$$

Then we have

(2.70)

(2.71)

where

$$I_p(z,t) = A_p(z,t)A_p^*(z,t) \tag{2.72}$$

$$I_s(z,t) = A_s(z,t)A_s^*(z,t) \tag{2.73}$$

From Eq.(2.71) we can get the expression of the probe wave as

$$A_s(z) = A_{s,0}\exp(-\frac{g_1 g_2 I_p}{2\Gamma_A}z) = A_{s,0}\exp[-g_B(\Omega_a)I_p z] \tag{2.74}$$

Eq. (2.74) verifies the counter-propagation of the probe wave and the pump wave. Besides, the intensity of the probe wave is exponentially amplified along '-z' direction. Here, g_B is known as the complex Brillouin gain, which is written as

$$\begin{aligned} g_B(\Omega_a) &= g_1 g_2 \frac{1}{\Gamma_A} = \frac{\varepsilon_0 \gamma_e^2 q^2 \omega_p}{cn\rho_0\Gamma_B}\frac{\Gamma_B}{2i(\Omega_a - \Omega_B) + \Gamma_B} \\ &= g_0 \frac{\Gamma_B}{2i(\Omega_a - \Omega_B) + \Gamma_B} \end{aligned} \tag{2.75}$$

where g_0 is the Brillouin gain coefficient, which is expressed as

$$g_0 = \frac{\varepsilon_0 \gamma_e^2 q^2 \omega_p}{cn\rho_0\Gamma_B} \tag{2.76}$$

The complex Brillouin gain is usually written in a form as

$$g_B(\Delta\upsilon) = G(\Delta\upsilon) + i\varphi_B(\Delta\upsilon) \tag{2.77}$$

The real part of the complex BGS is known as the BGS that represents the energy transfer between the pump light and the signal light. It is written as

(2.78)

where is the full width at half maximum (FWHM) of the BGS, is the frequency detuning. Fig.2.20(a) shows the BGS. It is seen that because the acoustic phonon has a lifetime, the BGS is broadened to have a Lorentz line shape.

Besides, the Brillouin gain reaches to the maximum when the frequency difference between the pump and probe light equals to the BFS. The imagine part of the complex BGS is known as the Brillouin phase spectrum that represents the phase shift of the signal light caused because of the nonlinear process. It is written as

$$\varphi_B(\Delta\upsilon) = -\frac{2g_0\Delta\upsilon_B\Delta\upsilon}{\Delta\upsilon_B^2 + 4\Delta\upsilon^2} \tag{2.79}$$

The Brillouin phase spectrum shown in Fig.2.20(b) indicates that no Brillouin phase shift occurs when the frequency difference between the pump and signal equals to BFS.

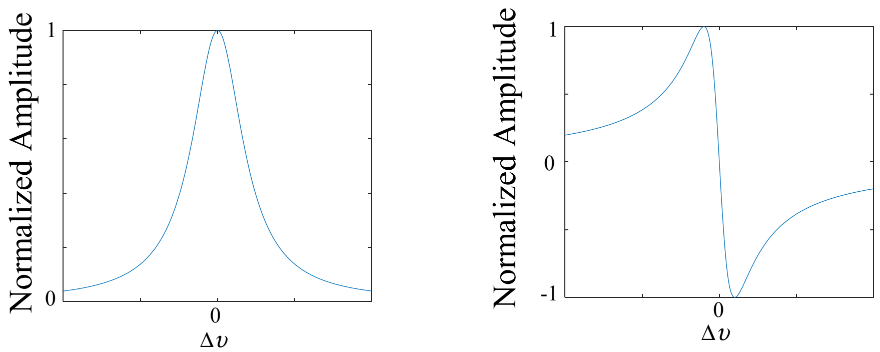

Figure 2.20 (a) Brillouin gain spectrum and (b) Brillouin phase spectrum.

In real Brillouin scattering-based DOFSs, the intensity information of the Brillouin scattering wave is usually used for sensing and fiber loss has to be considered. As a result, to obtain the intensity evolution of the probe wave along with the sensing fiber, Eq.(2.70) and Eq.(2.71) need to be modified as

(2.80)

(2.81)

In a short sensing range, the Brillouin scattering induced pump power loss is small enough that can be neglected, the intensity of the pump light then can be written as

$$I_p(z) = I_{p,0}e^{-\alpha z} \tag{2.82}$$

where $I_{p,0}$ is the intensity of the pump pulse at the incident port. By solving Eq.(2.80-82), the evolution of the probe intensity along the sensing fiber can be finally achieved as

$$I_s(z) = A_s(z)A_s^*(z) = I_{s,0}e^{G(\Delta\upsilon)I_{p,0}\exp(-\alpha z)L_{eff} - \alpha(L-z)} \tag{2.83}$$

where $I_{s,0}$ is the intensity of the probe wave at the launching end $z = L$. L_{eff} is the effective fiber length that is calculated by

$$L_{eff} = (1 - e^{-\alpha(L-z)}) / \alpha \tag{2.84}$$

C. The effects of temperature and fiber strain on BFS

BFS has the form as

$$\upsilon_B = \frac{2n\nu_a}{\lambda} \tag{2.85}$$

from which, we can see that the BFS is linearly related to the refractive index of the fiber core and the velocity of the acoustic wave while inversely proportional to the light wavelength. The velocity of the acoustic wave in the optical fiber is given by

$$\nu_a = \sqrt{\frac{E(1-\kappa)}{(1+\kappa)(1-2\kappa)\rho}} \tag{2.86}$$

Since young's module E, fiber density ρ and passion ratio κ change with the variations of temperature and strain, when external temperature or strain changes, the velocity of the acoustic wave changes. Besides, the refractive index of the fiber core is also influenced by the fiber strain. Consequently, by measuring BFS, the temperature or strain can be sensed.

Eq.(2.85) can be written in a form of the evolution of temperature and strain as

(2.87)

It is assumed that the variation of physical parameters is small enough. Then through Taylor expansion, BFS has a relationship with temperature as

$$
\begin{aligned}
&\upsilon_B(\varepsilon_0,T) \approx \upsilon_B(\varepsilon_0,T_0)[1+\Delta T\frac{\partial \upsilon_B(\varepsilon_0,T)}{\partial T}\Big|_{T=T_0}] \\
&=\upsilon_B(\varepsilon_0,T_0)[1+\Delta T(\Delta n_T+\Delta\kappa_T+\Delta E_T+\Delta\rho_T]
\end{aligned}
\tag{2.88}
$$

Here, the fiber strain is considered a constant. Similarly, the relationship between BFS and fiber strain can be derived as

$$
\begin{aligned}
&\upsilon_B(\varepsilon,T_0) \approx \upsilon_B(\varepsilon_0,T_0)[1+\Delta\varepsilon\frac{\partial \upsilon_B(\varepsilon,T_0)}{\partial \varepsilon}\Big|_{\varepsilon=\varepsilon_0}] \\
&=\upsilon_B(\varepsilon_0,T_0)[1+\Delta\varepsilon(\Delta n_\varepsilon+\Delta\kappa_\varepsilon+\Delta E_\varepsilon+\Delta\rho_\varepsilon]
\end{aligned}
\tag{2.89}
$$

From Eq. (2.88) and Eq(2.89), the influence of the strain and temperature on BFS can be derived as

$$
\Delta\upsilon_B = \mathrm{C}_{\nu,T}\Delta T + C_{\nu,\varepsilon}\Delta\varepsilon \tag{2.90}
$$

where $C_{\nu,T}$ and $C_{\nu,\varepsilon}$ respectively represent the temperature and strain coefficient of the Brillouin frequency in standard optical fibers. It is measured that at the wavelength of 1550 nm, $\mathrm{C}_{\nu,T} \approx 1.07\mathrm{MHz}/^{\circ}C$ and $\mathrm{C}_{\nu,\varepsilon} \approx 0.046$ MHz/$\mu\varepsilon$.

D. Sensing scheme of BOTDA

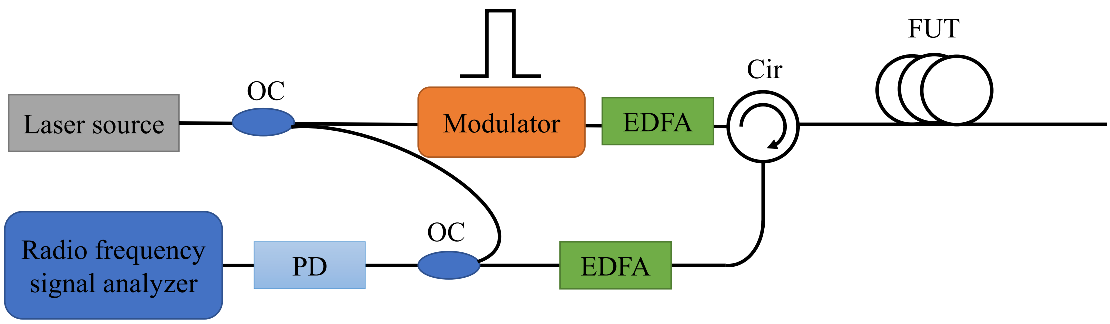

Figure 2.21 The structure of Brillouin optical time-domain reflectometry.

Since fiber strain is changed in case of external vibrations and BFS linearly depends on the fiber strain, Brillouin scattering light can be used for vibration sensing. Based on the scheme of spontaneous Brillouin scattering, BOTDR is proposed [109-112]. The structure of BOTDR shown in Fig. 2.21 is similar to that of the OTDR. The output of laser is divided into two beams by an OC. One beam is modulated into the pump pulse before launching into the FUT. The pulse is amplified by an EDFA to ensure the peak power is high enough to generate the Brillouin scattering light. The spontaneous Brillouin backscattering light is obtained through the circulator. Since the intensity of the spontaneous Brillouin backscattering light is usually very weak, an EDFA is usually placed after the circulator to amplify the signal. The other beam serves as the reference, which is used to beat with the signal light. The beating signal is detected by a PD and then analyzed by an RF signal analyzer to retrieve the BGS.

BOTDR suffers from disadvantages, like low SNR, small sensing range and limited spatial resolution, resulted from the weak spontaneous Brillouin backscattering signal. Therefore, to enhance the signal intensity, another sensing scheme based on the SBS amplification process is proposed, which is known as BOTDA [113, 114]. The basic sensing structure of a BOTDA system is shown in Fig. 2.22.

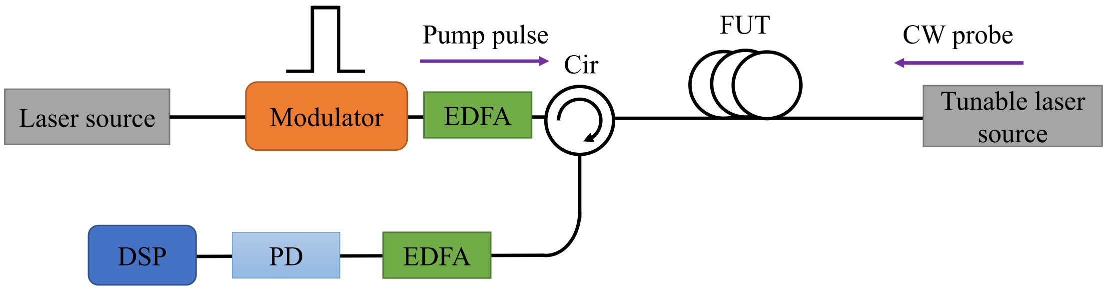

Figure 2.22 The basic sensing structure of Brillouin optical time-domain analyzer.

In the BOTDA system, pump pulses and the continuous wave (CW) probe light are injected into the FUT from two ends of the FUT, separately. SBS process occurs when the pump pulse meet the counterpropagating probe wave, which leads to the energy transferred from the pump light to probe light (giving rise to a gain to the probe light) or from the probe light to pump light (giving rise to a loss to the probe light). After interacting with the pump light, the probe light containing the Brillouin information is output from the FUT through the circulator and then detected by a PD. The detected signal is analog to digital converted and finally sent to the computer for further signal processing. The intensity change of the probe light reflects the Brillouin gain or loss along the fiber. As discussed in the above section, the gain or loss of the probe signal is related to the energy of acoustic phonons in the FUT, which is determined by the frequency detuning between the pump and probe lightwaves in comparison to the BFS. Therefore, in order to reconstruct the BGS along the entire fiber, the frequency of the probe light (or pump light) has to be swept over a frequency range near the BFS step by step.

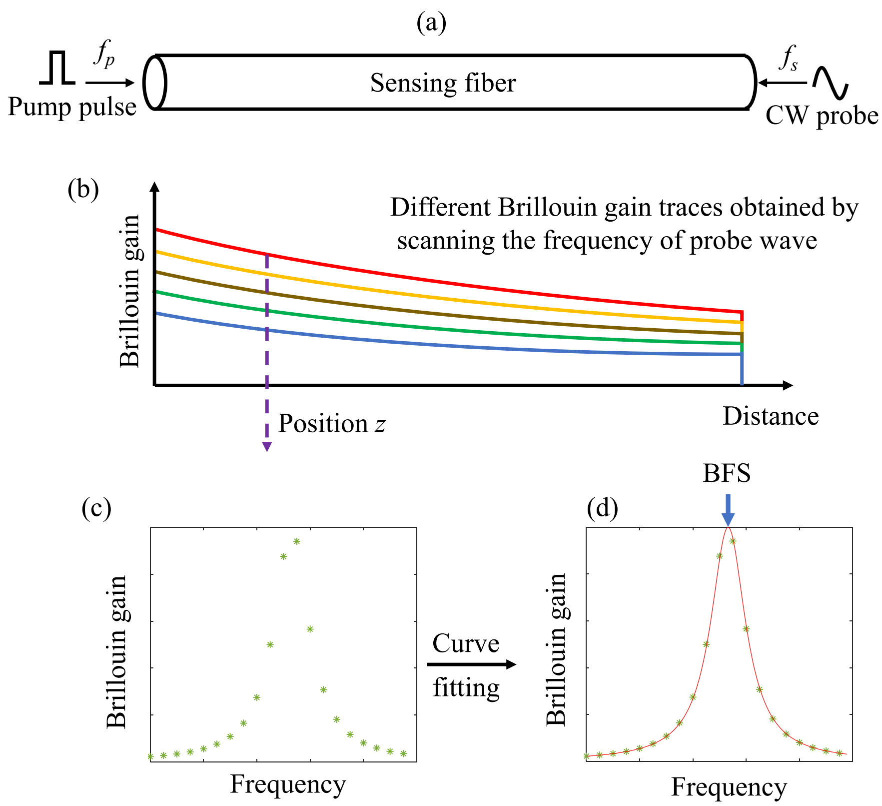

Figure 2.23 the sensing scheme of Brillouin optical time-domain analyzer.

Fig. 2.23 shows the sensing scheme of the BOTDA. Each time after tuning the frequency of the probe light, the spatial distribution of the Brillouin gain can be obtained, which is shown as in Fig. 2.23(b). After the frequency sweeping process, the Brillouin gain corresponding to the frequency detuning between the pump-probe frequency difference and the BFS can be obtained. Fig. 2.23(c) shows the Brillouin gain variation during frequency sweeping. The BGS can be obtained by fitting discrete points in Fig. 2.23(c) using the Lorentz line shape. Finally, distribution information of the BGS along the entire fiber is obtained. Since BFS is related to the temperature and fiber strain, by demodulating the distribution of BFS along the entire fiber, the abnormal strain (temperature is not the case in this thesis) point can be discovered. In both BOTDR and BOTDA systems, the abnormal strain point or vibration point is localized through the time to distance mapping algorithm, which is the same as the OTDR scheme given in section 2.2.2. Therefore, the spatial resolution of the BOTDA system is limited by the width of the pump pulse.

In dynamic BOTDA systems, the disturbance event is sensed by detecting the variations of fiber strain through the above discussed Brillouin spectrum reconstruction process. The factors that influence the measurement time of a traditional BOTDA includes

- The period of the pump pulse. To avoid signal aliasing, it is needed to ensure the single pump pulse interacting with the probe light each time in the sensing fiber. As a result, the minimum period of the pump pulse is determined by the length of the sensing fiber as $T_r=2nL/c$.
- The average number N_{ave}. The measurement time when averaging is considered is given by $N_{ave}T_r$.
- The number of sweeping frequencies N_f. The Brillouin spectrum reconstruction requires the frequency of the probe or pump light is swept
- Frequency switching time T_s.

Therefore, the measurement time of BOTDA can be calculated by

$$T_{total} = N_f(T_s + N_{ave}T_r) \tag{2.91}$$

Eq.(2.91) indicates that the measurement time is elongated with the increase of the number of sweeping frequency, the number of averages and the sensing distance. However, a large number of averages are usually used in BOTDAs to improve the SNR as the Brillouin signal is small. Besides, the number of the sweeping frequency cannot be largely reduced as an appropriate frequency interval is needed to ensure the Brillouin spectrum is well reconstructed. Normally, the measurement time of a BOTDA is in the order of a minute, which is quite time-consuming.

Therefore, in order to realize the vibration measurement in BOTDAs, the sensing speed has to be accelerated.

E. Techniques for accelerating the BOTDA sensing speed

Equation (2.91) tells us that the measurement time can be compressed by reducing the frequency switching time, which gives rise to the fast BOTDA techniques. In fast BOTDAs, the radio scanning frequency signal used to modulate the probe wave is generated by an arbitrary waveform generator (AWG) rather than a traditional microwave generator as the switching time of a fast speed AWG is only the order of *ns*, compared to the *ms* switching time needed by a microwave generator. Even so, the sensing speed is still limited by the time-consuming frequency sweeping process. To accelerate the sensing speed, various sweeping-free BOTDA techniques have been proposed, which include slope-assisted BOTDA (SA-BOTDA) [50-52, 115], optical frequency comb based sweep-free BOTDA (SF-BOTDA) [57-62, 116] and optical chirp chain based BOTDA (OCC-BOTDA) [117-119].

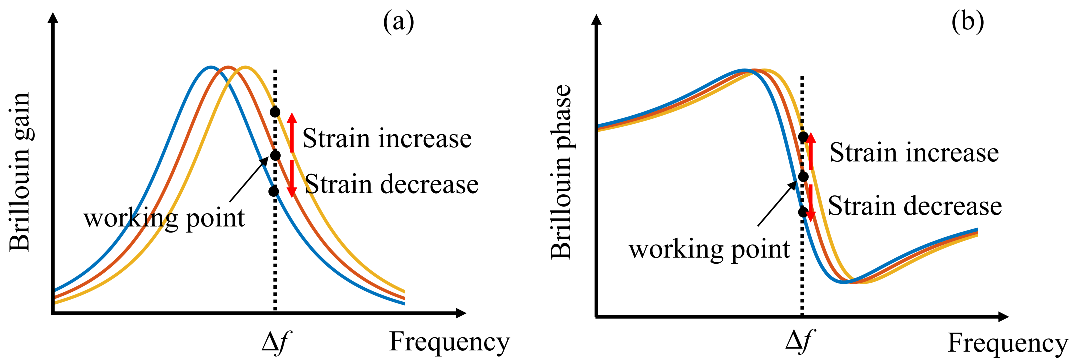

Figure 2.24 The sensing principle of slope-assisted BOTDA.

The sensing principle of SA-BOTDA is shown in Figure 2.24. There is a linear rising/falling range in either the BGS or the Brillouin phase spectrum. Figure 2.24 shows that the Brillouin gain or phase spectrum has good linearity at the half peak of the rising/falling edge. Therefore, in the SA-BOTDA, the frequency difference between the pump and probe light is fixed at the half peak of the rising/falling edge, which is called the working point. If the fiber is affected by external vibration, BFS is changed because of the change of fiber strain. Since the frequency between the pump and probe light is fixed, the Brillouin gain or phase shift of the probe light changes accordingly. By detecting the intensity change of the probe light or demodulating the phase change of the probe light, the corresponding BFS can be easily calculated since the relationship between the BFS and Brillouin gain/phase is approximated to be linear. The slope assist method eliminates the need for frequency sweeping in the BOTDA, making the measurement time largely reduced to be only limited by the length of the FUT and average times. However, when the strain applied to the fiber is large, the variation of the BFS can easily exceed the linear range. As a result, the limited bandwidth of the BGS or phase spectrum makes the dynamic range of the SA-BOTDA very small. To increase the dynamic range of the SA-BOTDA, multiple SA-BOTDA is proposed, where multiple probe tones are launched into the sensing fiber simultaneously [50, 52, 115]. By combining the slopes of these probe tones, a wider dynamic range can be reached. It should be noted that in multiple SA-BOTDAs, the computational size and the system complexity increase accordingly.

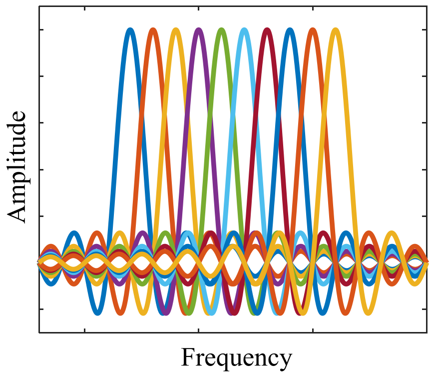

Figure 2.25 Frequency spectrum of the OFDM signal.

A more direct way to solve the frequency sweeping problem is to send an optical comb into the sensing fiber as the probe light. A powerful tool to generate the optical comb is to use the OFDM technique. OFDM is a multi-carrier signaling technique widely applied in optical communication systems. In OFDM systems, the information to be transmitted is loaded on S subcarriers for parallel transmission, thus greatly reducing the symbol rate. The OFDM subcarriers overlap in the frequency domain but are orthogonal to each other. Fig. 2.25 shows a typical spectrum of the OFDM signal. To maintain the orthogonality between each subcarrier, the following conditions should be met for the frequency interval of each subcarrier Δf_c:

$$\Delta f_c = m / T_{OFDM} \tag{2.92}$$

where T_{OFDM} is the symbol period and m is a positive integer. Assuming that time-domain OFDM symbol is sampled with a sampling period of T_s, then the minimum frequency interval is given by $\Delta f_c = 1/ST_s$. The time-domain discrete waveform of each OFDM symbol can then be expressed using a S-point IDFT as

$$E_{OFDM}(uT_s) = \frac{1}{\sqrt{S}} \sum_{x=0}^{S-1} c_x \exp(\frac{j2\pi xu}{S}) \tag{2.93}$$

where c_x, $x = 0, \ldots, S-1$, are information symbols encoded on the S subcarriers. After IDFT, the output time-domain signal $E_{OFDM}(uT_s)$, which is typically complex, is parallel to serial (P/S) converted, and sent to a pair of digital-to-analog converters (DAC) to generate both the I and Q parts of the signal. An optical I/Q modulator is then needed for field modulation to the optical carrier.

OFDM signaling can also be implemented in IM/DD systems where real-valued electrical signals are required. This can be done by imposing Hermitian symmetry on the subcarriers in the frequency domain so that the IDFT output $E_{OFDM}(uT_s)$ can be real-valued. In this case, only one DAC is needed for electrical signal generation. The DAC output can then be used to modulate either a directly modulated laser (DML) or to drive an intensity modulator biased at the quadrature point. Either way, a large optical carrier exists along with the modulated OFDM signal. At the receiver side, a single PD is used for square-law detection of the received optical signals which can be written as

(2.94)

where R_D is the responsivity of the PDs. The first term is the DC component introduced because of the existence of the optical carrier; the second term is the subcarriers-to-subcarriers beating interference (SSBI) while the third term is the signal of interest. The SSBI serves as noise to the OFDM signal and can be mitigated using various techniques [120, 121].

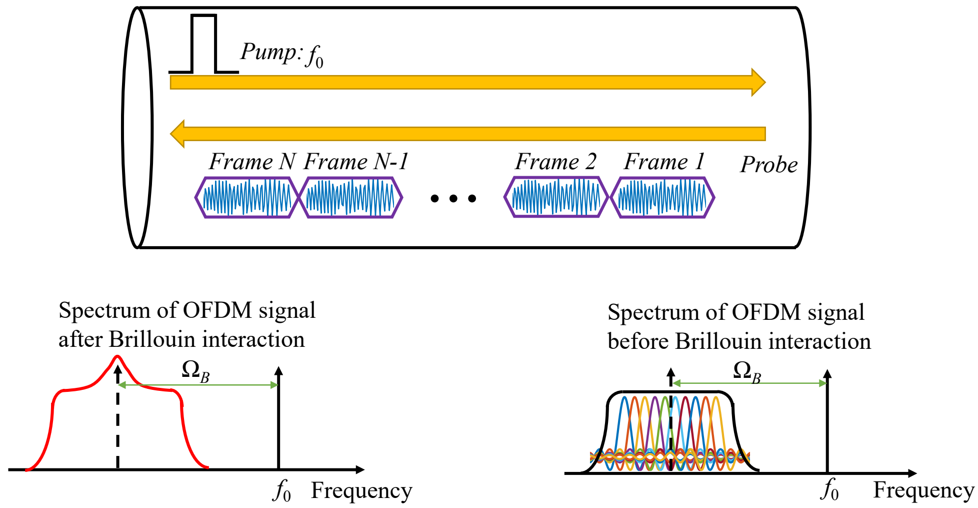

Figure 2.26 The sensing principle of OFDM-BOTDA

Since OFDM signals are transmitted blockwisely, the probe light is pulsed in OFDM-BOTDA systems. The sensing principle is shown in Fig 2.26. A wideband pulsed OFDM probe is launched into the FUT, while a single tone pump is introduced from the opposite direction. The multi-tone optical probe signal distributes symmetrically around BFS with a certain frequency spacing. After interacting with the pump pulse, the selected frequency component will be amplified. By comparing the frequency spectrum of the OFDM signal before and after the SBS process, the BGS can be obtained. The Brillouin phase spectrum can be obtained by demodulating the phase of the OFDM signal as well, which is not detailed here Normally to make the reconstructed BGS/BPS symmetric, the difference between the pump frequency and the center frequency of the OFDM probe signal is set near the BFS. The use of the wideband probe light makes it possible for OFDM-BOTDAs to retrieve the Brillouin gain or phase spectrum in a single-shot measurement. Besides, the bandwidth of the OFDM probe light is only limited by the performance of the equipment, which means a wide dynamic range can be easily obtained. However, the main drawback of OFDM-BOTDA is the spatial resolution, which is linearly proportional to the probe frame duration. There is a trade-off between the probe frame duration and the frequency spacing of the optical comb due to the orthogonal condition. The spatial resolution increases with the decrease of the frequency interval. Since a good BPS and BGS profile is needed to ensure good measurement accuracy, the frequency interval cannot be very large, resulting in the spatial resolution usually limited to a few tens of meters.

More recently, a novel dynamic BOTDA using the optical chirp chain (OCC) has been proposed taking the advantage of the frequency agility technique, where the probe wave is composed of cascaded optical chirp segments as shown in Fig. 2.27. The frequency of each optical chirp segment is rapidly tuned from $f_{occ,1}$ to $f_{occ,2}$ with the tuning range covering the BFS, such that the traditional frequency sweeping process can be eliminated. After interacting with the pump, the Brillouin gain information is carried by the frequency tones of the OCC probe, which can be used to reconstruct the BGS. In an optical chirp segment, a frequency tuning range of several hundred MHz is usually completed within tens of nanoseconds. Therefore, the interaction time between the pump light and each frequency tone is much smaller than the lifetime of the acoustic phonon, leading to a transient SBS interaction. In the transient SBS interaction process, the steady state is not satisfied. As a result, the BGS no more has a Lorentz line shape.

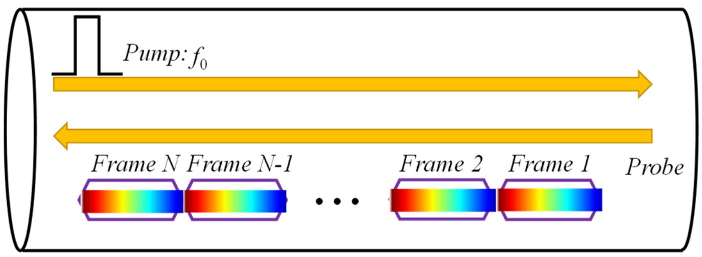

Figure 2.27 Interactions between the pump light and OCC probe light in OCC-BOTDA.

Figure 2.28 shows the comparison between the BGS reconstructed using the ‘sawtooth’ like OCC and the intrinsic BGS with a Lorentz line shape. The reconstructed BGS is asymmetric with the peak frequency shifted. Besides, since an equivalent frequency near the BFS is generated when the frequency sharply decreased from the highest frequency component v_N to the lowest frequency component ν_1 at the frequency discontinuity position, a "ghost peak" appears beside the main peak [117]. The spatial resolution of the OCC-BOTDA is limited by the duration of the OCC segment. However, the transient SBS interaction and OCC modulation noise limit the sensing performance of the OCC-BOTDA, high measurement accuracy of BFS is difficult to be reached. Besides, in OCC-BOTDA, the frequency sweeping time is compressed as short as the duration of an OCC segment. Since a higher dynamic range leads to a large frequency sweeping rate, resulting in a large noise induced by the transient SBS interaction and OCC modulation, there is a tradeoff between the dynamic range and spatial resolution.

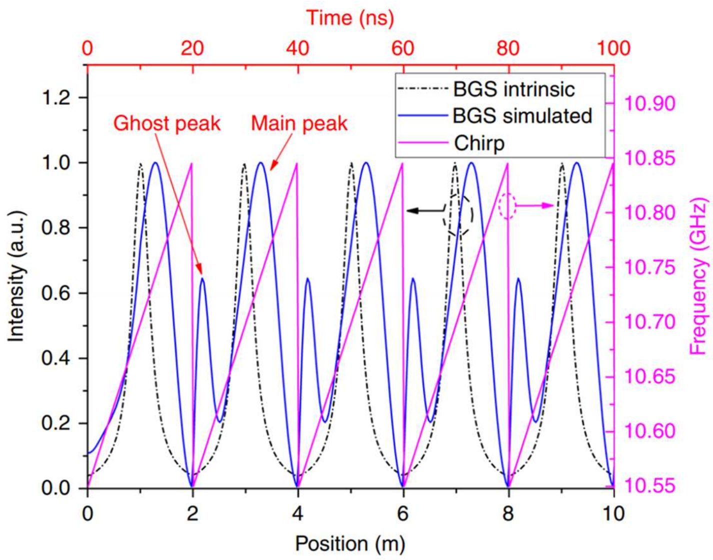

Figure 2.28 The distributed BGSs along the fiber for the intrinsic case (black dashed-dotted line), "sawtooth" mode (blue line), and distributed chirp frequency (magenta line) [117].

In section 2.2.3, we have introduced the mechanism of the Brillouin scattering and the applications of Brillouin backscattering light in the distributed optical fiber vibration sensing area. The advantage of the Brillouin backscattering based dynamic DOFSs can be concluded as

1) Capable of measuring the vibrations with large fiber strain. The fiber strain of larger than a thousand με can be sensed by the BOTDA.
2) Capable of detecting infrasound vibrations.

However, the disadvantages of dynamic BOTDA include the following.

1) Compared to φ-OTDRs that have strain sensitivity in the order of tens of nε. The strain sensitivity of the BOTDA is much lower, which is usually in the order of ten με because the measurement accuracy of BFS is in the order of MHz.
2) The tradeoff between the spatial resolution, measurement accuracy and dynamic range is a problem for dynamic BOTDAs.

In all backscattering based dynamic DOFS systems, the general problem is the limited SNR due to the weak intensity of the backscattered signal detected by the PD, which as a result limits the sensing range. At the same time, since the time of flight is used for obtaining location information, the event sampling rate is inversely proportional to the sensing distance. This has limited the maximum vibration frequency that can be detected.

Chapter 3

Unidirectional forward transmission-based ultralong DOFVS

In this chapter, an ultra-long DOFVS system using unidirectional forward transmission of a CW light and coherent detection with DSP is presented. Two optical fibers, which are close to each other, are deployed for sensing. An FS-ODL consisting of an AOM and a TDF is used at the far ends of two sensing fibers to form a loop-back configuration. Coherent detection is used to retrieve the vibration-induced phase fluctuations of the baseband signals as well as the IF signals generated by the FS-ODL. Two phase differential signals can be constructed from the obtained phase signals, which can then be used to localize the vibration events by correlation operations. Thanks to the nature of unidirectional forward transmission, the RBN can be avoided. Meanwhile, forward transmission enables optical amplifiers to compensate for the signal loss and hence fundamentally overcome the sensing range limit. Localization of a few hundred Hz, around 1 kHz and tens of kHz vibrations has been experimentally demonstrated over a total length of 1230 km sensing fiber. Less than 125 m spatial resolution can be obtained over the 615 km sensing range for vibrations with larger than 1 kHz frequency by using averaging of 30 times tests due to the nature of asynchronous operation. Detection of frequencies from infrasound to ultrasound is realized.

3.1 Introduction

With the development of fiber technology, there is an increasing demand for the long-haul and ultralong-haul fiber vibration sensing in various industrial areas. Since the intensity of backscattering light is normally very weak, it is difficult to realize the ultralong haul sensing in backscattering light-based DOFVSs. To solve this problem, sights are set in the forward transmission light. As aforementioned in section 2.1, the forward transmission light has been the basis of distributed optical fiber interferometers, however, light beams are bidirectionally transmitted in a single fiber in distributed optical fiber interferometers. As a result, the RBN is a problem for bidirectional transmission systems, which degrades the sensing performance of long-haul or ultralong-haul distributed fiber interferometers greatly. In [94], WDM was utilized to reduce the influence of RBN in the MZI. However, the sensing structure is much complex. Besides, in WDM MZI systems, the optical delay is wavelength dependent. As a result, the deviation of the location obtained using the time delay estimation method increases with the increase of the sensing distance. Recently, an MI using PBS and FRM was reported [122]. 2/3 of the RBN can be separated, however, the residual RBN still degrades the SNR. Moreover, in direct detection based distributed fiber interferometers, the directly detected signal may exhibit a nonlinear phase to amplitude conversion, referring to Eq. (2.5), which may result in a serious distortion of the sensing signal when the vibration amplitude is very large or the interferometer sensor is not fixed at the quadrature working point [123]. Therefore, phase demodulation techniques are needed to solve this problem. Polarization-induced fading is also a problem for MZI or ring structured Sagnac interferometers. In these cases, additional polarization control is necessary, which increases the complexity of the system.

In optical fiber communication systems, the transmission distance can easily reach one thousand kilometers [124, 125]. The reason is that communication signals are unidirectionally forward transmitted in the optical fiber, which makes it possible for optical amplifiers to be cascaded to form a chain to compensate for the signal loss along propagation. Moreover, in unidirectional transmission systems, the RBN problem is completely eliminated. Besides, phase and polarization diversity coherent detection has been widely used in optical communication systems [126] to retrieve both the amplitude and phase of the received signal and as well to solve the polarization fading problem. Inspired by these characteristics of optical communication systems, we propose a new DOFVS system, which uses the unidirectional forward transmission light for sensing. Compared with the reported DOFVSs, the sensing distance is largely extended. Besides, the phase and polarization diversity homodyne coherent detection is used to realize the phase demodulation and solve the polarization fading problem simultaneously. An FS-ODL placed at the far ends of two sensing fibers, consisting of two couplers, an AOM and a TDF is used to generate two signals of different frequencies with a fixed time delay. Two differential phase signals are constructed from the phase information of these two signals of different frequencies, which can be used to determine the vibration position. Localization of such vibrations is achieved by calculating the time delay between two constructed differential phase signals using correlation operations. Averaging is used to further improve localization accuracy.

3.2 Principle of the phase and polarization diversity homodyne coherent detection

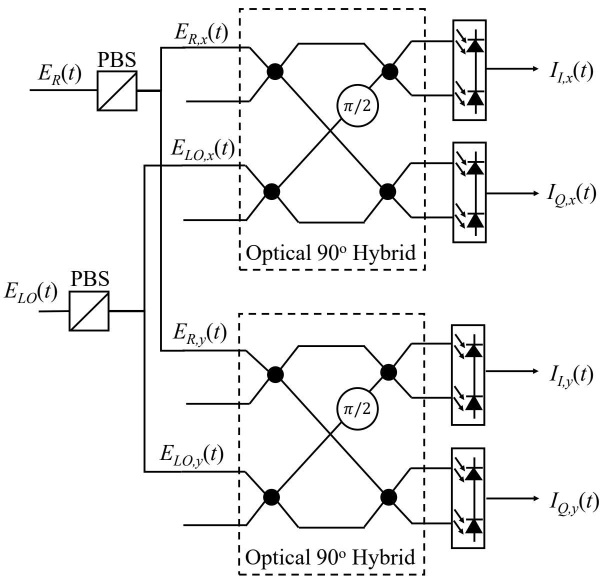

Figure 3.1 Schematic diagram of a phase and polarization diversity coherent receiver.

The structure of a phase and polarization diversity coherent receiver is shown in Fig.3.1.

Either the signal or the LO is divided by the PBS into two beams along two perpendicular polarizations named x polarization and y polarization. The LO light and the signal light in the same polarization are injected into an optical 90-degree hybrid, which is composed of four 3dB optical couplers and a $\pi/2$ phase shift component. A pair of balanced photodetectors (BPDs) are used to detect four mixing signals of the signal and LO generated by the optical 90-degree hybrid. The transfer matrix $H_{2\times2}$ of an ideal 3dB coupler can be expressed as

$$H_{2\times2} = \frac{1}{\sqrt{2}}\begin{bmatrix} 1 & \mathrm{j} \\ \mathrm{j} & 1 \end{bmatrix} \tag{3.1}$$

Therefore, there exist a 180° phase shift between two optical signals launched into the same BPD and a 90° phase difference between two electrical signals output from the pair of BPDs. These two electrical signals contain the I and Q components of the homodyne beating signal between the signal light and the LO. Considering two polarizations of the signal light and the LO, the four-channel electrical outputs of the phase and polarization diversity coherent receiver can be written as

$$I_x = R_D\sqrt{\frac{\eta P_S P_{LO}}{2}}\cos\left(\theta_x(t) - \theta_{LO}(t) + \psi\right) \tag{3.2}$$

$$Q_x = R_D\sqrt{\frac{\eta P_S P_{LO}}{2}}\sin\left(\theta_x(t) - \theta_{LO}(t) + \psi\right) \tag{3.3}$$

$$I_y = R_D\sqrt{\frac{(1-\eta) P_S P_{LO}}{2}}\cos\left(\theta_y(t) - \theta_{LO}(t)\right) \tag{3.4}$$

(3.5)

where P_S and P_{LO} are the powers of the signal light and LO, respectively; η is the power ratio of the two polarization components while is the phase difference between them; $\theta_x(t)$, $\theta_y(t)$; and $\theta_{LO}(t)$ are the phases of the signal along x-polarization, the signal along y-polarization and LO, respectively. Clearly, one can restore the baseband complex signal in the x-polarization through Eq. (3.2) and Eq (3.3) as

$$I_x(t) = I_{I,x}(t) + jI_{Q,x}(t) \tag{3.6}$$

Through Eq. (3.4) and Eq. (3.5), the complex signal in the y-polarization can be written as

$$I_y(t) = I_{I,y}(t) + jI_{Q,y}(t) \tag{3.7}$$

The phase information can be obtained by calculating the angle of the complex signal $I_x(t)$ or $I_y(t)$. Since two orthogonally polarized signals cannot simultaneously fall to zero, at each time the signal from the polarization state with a better SNR can be used, thus polarization-induced fading can be suppressed.

3.3 Sensing principle

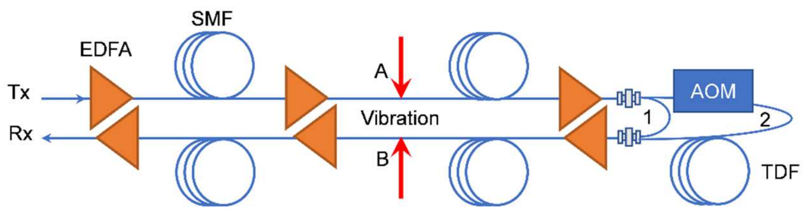

Figure 3.2 Schematic diagram of the localization principle.

In this experiment, by using the phase and polarization-diversity homodyne coherent receiver, the phase signal can be obtained using the I/Q demodulation algorithm as mentioned in section 3.2. Therefore, we can not only realize the event sensing (e.g., intrusion detection) but also quantify the event, such as measuring the exact frequency and amplitude of the external vibrations. The sensing scheme is shown in Fig. 3.2. The FUT consists of two fibers placed together along the sensing area. At the far end of the FUT, the forward transmitted light is split into two beams. Beam 1 goes directly to the coupler. Meanwhile, beam 2 goes through an AOM followed by a TDF which is used as a frequency shifter and a fixed time delay, respectively. Beam 1 and beam 2 are coupled into the FUT again and finally detected by a commercial phase- and polarization-diversity coherent receiver. When there is no external vibration, the phase of the light at the receiver will vary slowly due to the carrier phase noise and other phase noises resulting from environmental fluctuations (wind flow, acoustic, thermal variations, etc.). When an external vibration occurs at a certain position of the FUT, the refractive index of the fiber core and the fiber birefringence will change accordingly, which in turn will induce a phase change in the transmission light. Due to the loop-back configuration, a single external vibration will affect two different positions of the FUT, marked as positions A and B in Fig. 3.2. Because two fibers are very close to each other, when light passes through position A and position B, the phase shift caused by the external vibration will be the same. The light at the receiver contains baseband and IF components due to the far-end FS-ODL structure.

From Fig.3.2, the propagation path for the baseband signal is path$_b$: Tx→A→1→B→Rx， and the baseband signal can be expressed as

$$E_b = \sqrt{P_b}\cos[\omega_0 t + \varphi_{nb}(t) + \varphi_v(t) + \varphi_v(t - \tau_{AB1})] \tag{3.8}$$

The propagation path for the IF signal is path$_{if}$: Tx→A→2→B→Rx, and the IF signal can be expressed as

$$E_{if} = \sqrt{P_{if}}\cos[(\omega_0 + \Delta\omega)(t - \Delta\tau) + \varphi_{nif}(t) + \varphi_v(t) + \varphi_v(t - \tau_{AB2})] \tag{3.9}$$

where P_b and P_{if} are the powers of the baseband signal and the IF signal, respectively. ω_0 is the angular frequency of the incident light. $\Delta\omega$ is the frequency shift caused by the AOM. $\varphi_{nb}(t)$ and $\varphi_{nif}(t)$ are phase noises of the baseband signal and IF signal, respectively. $\varphi_v(t)$ is the external vibration-induced phase change. τ_{AB1} is the time for light to propagate from A to B along path: A→1→B. τ_{AB2} is the time for light to propagate from A to B along path: A→2→B. $\Delta\tau$ is the time difference for light to propagate along path$_b$ and path$_{if}$, which is determined by the length of the TDF. It is obvious that

(3.10)

After beating with the LO, four-channel output signals of the receiver contain in-phase (*Ix, Iy*) and quadrature (*Qx, Qy*) components of the beating signal between the forward transmitted light and the LO, in both *x*- and *y*- polarizations. Phase information of the baseband signal and

IF signal can be extracted since the whole optical field is obtained using coherent detection. The demodulated phase of the baseband signal can be written as

$$\varphi_b(t) = \varphi_{nb}(t) + \varphi_v(t) + \varphi_v(t - \tau_{AB1}) - \varphi_{LO}(t) \tag{3.11}$$

The demodulated phase of the IF signal can be written as

$$\varphi_{IF}(t) = -(\omega_0 + \Delta\omega)\Delta\tau + \varphi_{nif}(t) + \varphi_v(t) + \varphi_v(t - \tau_{AB2}) - \varphi_{LO}(t) \tag{3.12}$$

where $\varphi_{LO}(t)$ is the phase of the LO. After removing the DC component $(\omega_0 + \Delta\omega)\Delta\tau$ through subtracting the average power of the signal, $\varphi_{IF}(t)$ can be written as

$$\varphi_{IF}(t) = \varphi_{nif}(t) + \varphi_v(t) + \varphi_v(t - \tau_{AB2}) - \varphi_{LO}(t) \tag{3.13}$$

We can construct two differential signals as

$$\Delta\varphi_1(t) = \varphi_b(t) - \varphi_{IF}(t) = \varphi_v(t - \tau_{AB1}) - \varphi_v(t - \tau_{AB2}) + \varphi_{nb}(t) - \varphi_{nif}(t) \tag{3.14}$$

$$\begin{aligned}\Delta\varphi_2(t) &= \varphi_{IF}(t + \Delta\tau) - \varphi_b(t) \\ &= \varphi_v(t + \Delta\tau) - \varphi_v(t) + \varphi_{nif}(t + \Delta\tau) - \varphi_{nb}(t) + \varphi_{LO}(t) - \varphi_{LO}(t + \Delta\tau)\end{aligned} \tag{3.15}$$

Under conditions that the linewidth of the light source is ultranarrow and the length of the TDF is negligible compared to the coherent length of the light source, we can have approximations below

$$\varphi_{nb}(t) - \varphi_{nif}(t) \approx 0 \tag{3.16}$$

$$\varphi_{nif}(t + \Delta\tau) - \varphi_{nb}(t) \approx 0 \tag{3.17}$$

(3.18)

Therefore, Eq. (3.14) and Eq. (3.15) can be rewritten as

(3.19)

(3.20)

It is obvious that

$$\Delta\varphi_1(t)=\Delta\varphi_2(t-\tau_{AB2}) \tag{3.21}$$

By measuring the time delay between $\Delta\varphi_1(t)$ and $\Delta\varphi_2(t)$, the distance from point A to point B along path: A→2→B can be calculated through $L = c\tau_{AB2}/n$. As the total fiber length of the sensing system is already known, the vibration position can thus be located.

3.4 Time delay estimation based on cross-correlation

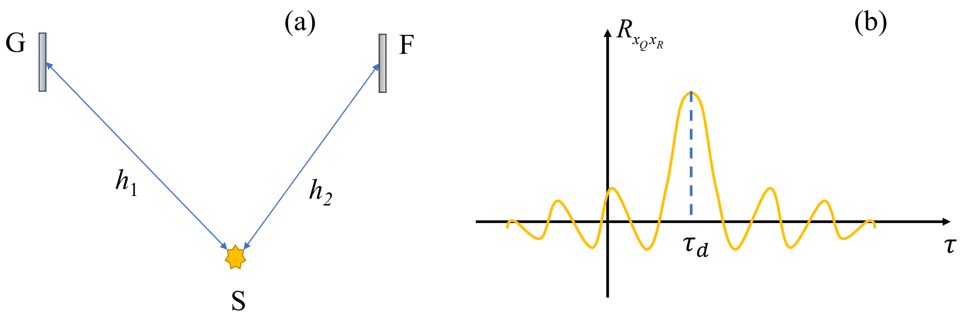

Figure 3.3 (a) The basic model of a time-delay system. (b) The cross-correlation curve of $R_{x_Q x_R}$.

The time delay between $\Delta\varphi_1(t)$ and $\Delta\varphi_2(t)$ can be obtained through time delay estimation, which is a signal processing technique that has been extensively investigated in fields like radar, sonar, wireless communications, etc. to determine the time differences of arrivals between homologous signals received by different detectors due to different signal transmission distances. Among all the methods of determining the time delay, cross-correlation is the most classical one. The basic model of a time-delay system is shown in Fig.3.3 (a). F and G are signal receivers. S is the signal source. The signals detected by F and G can be written as

(3.22)

(3.23)

where $s(t)$ is the time-domain signal, r represents the amplitude difference between two received signals; τ_d is the time delay between two received signals, and is determined by the distance difference ; $n_1(t)$ and $n_2(t)$ are noise items. Generally speaking, the signal item and noise items are uncorrelated. Therefore, by comparing the time-domain similarity of two received signals through correlation analysis, the time delay between two signals can be obtained. The cross-correlation of two signals can be expressed as

$$R_{x_F x_G} = \int_{-\infty}^{\infty} x_F(t) x_G(t+\tau) dt \tag{3.24}$$

Fig. 3.3 (b) schematically shows characteristics of the '$R_{x_F x_G}$—τ' cross-correlation curve. It is obvious that the cross-correlation function has a maximum value when $\tau = \tau_d$. Therefore, through searching the peak of '$R_{x_F x_G}$—τ' curve, the time delay τ_d can be determined.

In the discrete system, the detected signals are expressed as

$$X_F(T) = S(T) + N_1(T) \tag{3.25}$$

$$X_G(T) = rS(T-D) + N_2(T) \tag{3.26}$$

where D is the discrete time delay. It is obvious that in the discrete system the system sampling rate limits the minimum time resolution.

3.5 Experimental setup

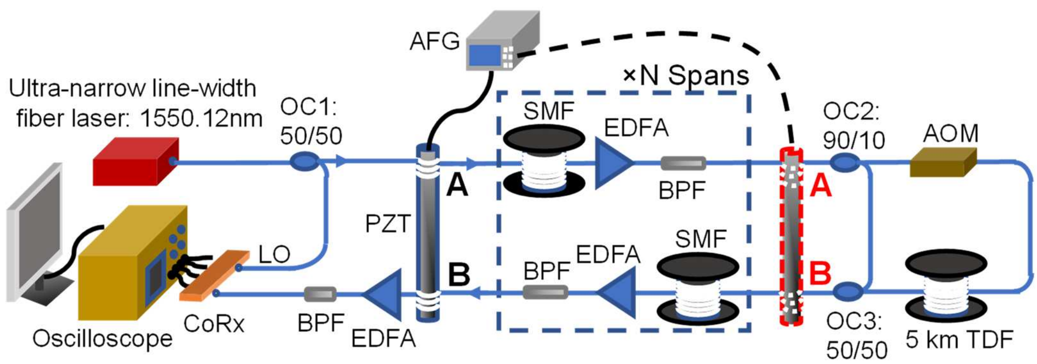

Figure 3.4 The configuration of the proposed system. AFG: arbitrary function generator, SMF: single-mode fiber, OC: optic coupler, AOM: acoustic-optic modulator, PZT: piezoelectric ceramic transducer, BPF: bandpass filter, CoRx: coherent receiver.

Figure 3.4 shows the experimental setup of the ultra-long-range unidirectional transmission-based DOFVS system. The output of an ultra-narrow-linewidth CW tunable fiber laser (NKT

X15 with 100 Hz linewidth) operating at 1550.12 nm was split into two branches by a 50/50 coupler. The lower branch was sent to the CoRx serving as the LO. The upper branch was launched into the FUT directly. The total length of the FUT was around 1230 km, containing 15 fiber spans. Standard single-mode fiber (SSMF, G.652D) was used in all cases. An EDFA (Huawei C-band OAU) was utilized in each span of the 1230-km fiber link to compensate for the fiber loss. Because the sensing system is based on the measurement of the phase, nonlinear phase shift will influence the performance significantly. To depress the nonlinear effect, the signal power output from the EDFA after each fiber span is controlled. Also, to reduce the influence of ASE, a 4 nm bandwidth filter is used after each fiber span. Two 60-m fibers were wrapped around the same piezoelectric transducer (PZT) to cause external vibrations. The modulation constant of the PZT is 8.3 rad/V at 1550 nm, corresponding to a strain-voltage coefficient of 23 nε/V. At the far end of the fiber link, the light was split into two beams by a 90/10 coupler. 90 percent of light went through an AOM, which induced a 100 MHz frequency shift to the light, and a 5-km TDF. Meanwhile, 10 percent of the light passed directly. These two branches were then recombined and looped back using another fiber. To investigate the sensing performance, two cases were considered in this experiment: 1) vibrations occur at both the beginning and end of the fiber link., and the corresponding positions are marked as points A and B in black as shown in Fig.3.4. In this case, the distance from point A to point B is 1230 km; 2) vibrations occur at the middle of the fiber link, and the corresponding positions are marked as points A and B in red as shown in Fig.3.4. Meanwhile, the distance from point A to coupler 2 and the distance from point B to coupler 3 are both 500 m. A polarization-diversity CoRx, consisting of an optical 90° hybrid mixer (PHOTOP C-band 2×8) and four BPDs (Finisar BPDV2150RQ), was used for the detection of the received sensing signals. The output signals from the BPDs were then sampled by a real-time oscilloscope (Keysight DSAZ634A). The sampling rate has a linear relationship with the spatial resolution: the higher the sampling rate is, the higher the spatial resolution can be obtained. Limited by the memory size of the oscilloscope, the sampling rate was set to 400 MSa/s in our case. As a result, the sampling rate limited spatial resolution is 0.5 m. Offline DSP was then used to analyze the collected data.

3.6 Experimental results

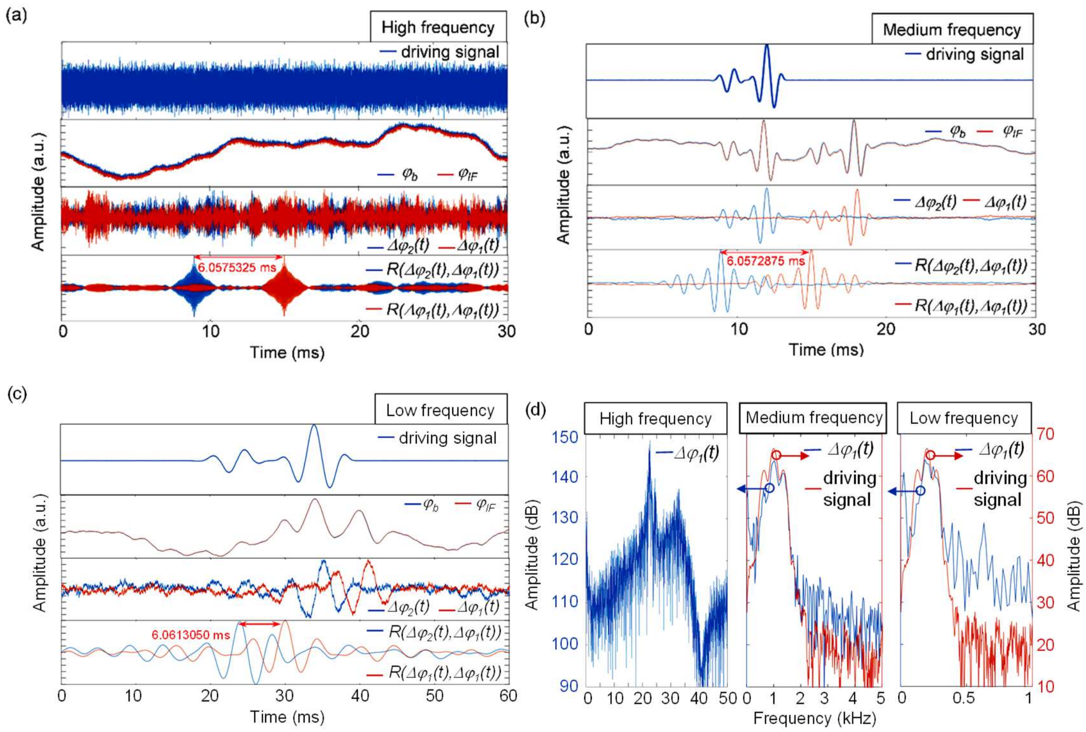

Figure 3.5 Electrical driving signals, demodulated phase curves, constructed differential phase curves and the cross correlation curves when (a) high-frequency, (b) medium-frequency and (c) low-frequency signals are applied at the beginning and end of the fiber link. (d) The retrieved frequency spectra after FFT of the constructed differential phase signals when three vibration signals are applied and spectra of medium-frequency and low-frequency electrical driving signals.

Firstly, the localization performance when vibration events occur at both the beginning and end of the fiber link is investigated. Three different vibration signals are applied on the PZT to emulate the practical vibrations with high, medium and low frequencies. The first one is a Gauss white noise like vibration signal with a frequency range in the order of tens of kHz (high-frequency case), which is generated using the noise function of an AWG (Agilent 33120A) with a peak-to-peak voltage of 20 V. Because the frequency response of PZT is not uniform, especially in the ultrahigh-frequency region, the actual vibration signal applied on the fiber is the Gauss white noise signal superimposed with the frequency response of the PZT. Another two electrical driving signals are user-defined signals with vibration frequency ranges of around 1 kHz (medium-frequency case) and a few hundred Hz (low-frequency case), respectively. The peak to peak voltage of these two signals is 60 V. That means the fiber strain is 1.38 με.

Fig. 3.5(a), (b) and (c) show the electrical driving signals, demodulated phase curves, constructed differential signals $\Delta\varphi_1(t)$ and $\Delta\varphi_2(t)$, and their cross-correlation curves, respectively. Fig.3.5 (d) shows the spectra calculated from the constructed differential signal $\Delta\varphi_1(t)$ of three vibrations (blue lines) and spectra of the medium-frequency and low-frequency electrical driving signals (red lines). Before calculating the cross-correlation of $\Delta\varphi_1(t)$ and $\Delta\varphi_2(t)$, a low pass digital filter was used to remove the noise. Specifically, a 40-kHz bandwidth filter is used for the noise like high-frequency vibration signal; a 2-kHz bandwidth filter is used for the medium-frequency vibration signal and a 400 Hz bandwidth filter is used for the low-frequency vibration signal. From Fig.3.5, the following observations can be made: i) External vibrations induce obvious fluctuations on the phase curve. However, the background phase noise makes the phase curve slowly fluctuate. ii) By constructing two differential signals: $\Delta\varphi_1(t)$ and $\Delta\varphi_2(t)$, according to Eq. (3.19) and Eq.(3.20), the influence of the phase noise can be significantly reduced. iii) The SNR decreases with the decrease of frequency as shown in Fig. 3.5 (d). For the high-frequency case, the SNR for the frequency component from 22 kHz to 25 kHz is 32 dB. For the medium-frequency case, the SNR is 24dB. For the low-frequency case, the SNR is 16dB. One factor is the differential effect. In case a sinusoidal vibration is applied on the fiber, the corresponding modulated phase term can be written as , where is the amplitude of the phase change and is the frequency of the vibration signal. Therefore, the constructed differential signal can be written as

. (3.27)

Since $\Delta\tau$ is related to the length of TDF, which is 5 km in this experiment, $\Delta\tau$ is 2.45×10^{-5} s. As a result, $\Delta\varphi_2(t)$ is very small when a low-frequency vibration occurs. Eq. (3.27) indicates that due to the differential effect, the differential phase signals have low sensitivity to low-frequency vibrations. Another factor is the fiber link noise, which is inversely proportional to the frequency [127, 128]. From Fig. 3.5(a), the time delay measured is 6.0575325 ms. Therefore, the fiber length $L_f = c\tau_{AB2}/n$ = 1235376 m, where c = 299792458 m/s and n = 1.47.

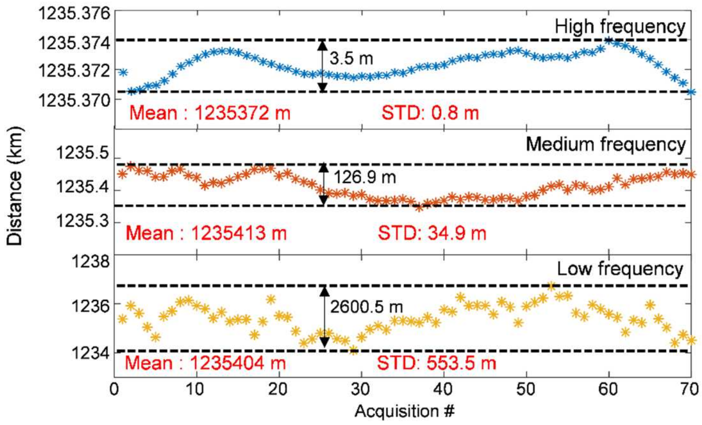

Figure 3.6 Localization results when vibrations occur at both the beginning and end of the fiber link. STD: standard deviation.

In order to investigate the location accuracy of the sensing system, 70 data sets averaged by 30 times were acquired for each vibration. The localization accuracy is defined as the measurement accuracy of the fiber length between two vibration points. Fig. 3.6 shows the localization results. One can see that the calculated mean of the fiber length is 1235372 m with a difference of 3.5 m for the high-frequency vibration. However, the calculated mean of the fiber length for the medium-frequency vibration is 1235413 m with a difference of 126.9 m, and the calculated mean of the fiber length for the low-frequency vibration is 1235404 m with a difference of 2600.5 m. According to the theory of time delay estimation, the SNR influences the location accuracy significantly [96, 129]. If the SNR is lower than a threshold, the location error increases dramatically with the reduction of SNR. Due to the differential effect mentioned above, the SNR decreases when the vibration frequency decreases. Besides, the effective bandwidth and observation-time product (BT) of the differential signals influence the location accuracy as well. The effective bandwidth refers to the bandwidth of the vibration signal, and the observation time refers to the time period from the occurrence of one vibration signal to the disappearance of both two vibration signals as shown in Fig. 3.7(b). The BT value should be larger than 100 to ensure a good location estimation. Therefore, the proposed scheme has very high localization accuracy when vibration frequency is larger than 10 kHz, while the location accuracy decreases largely when lower vibration frequencies are considered.

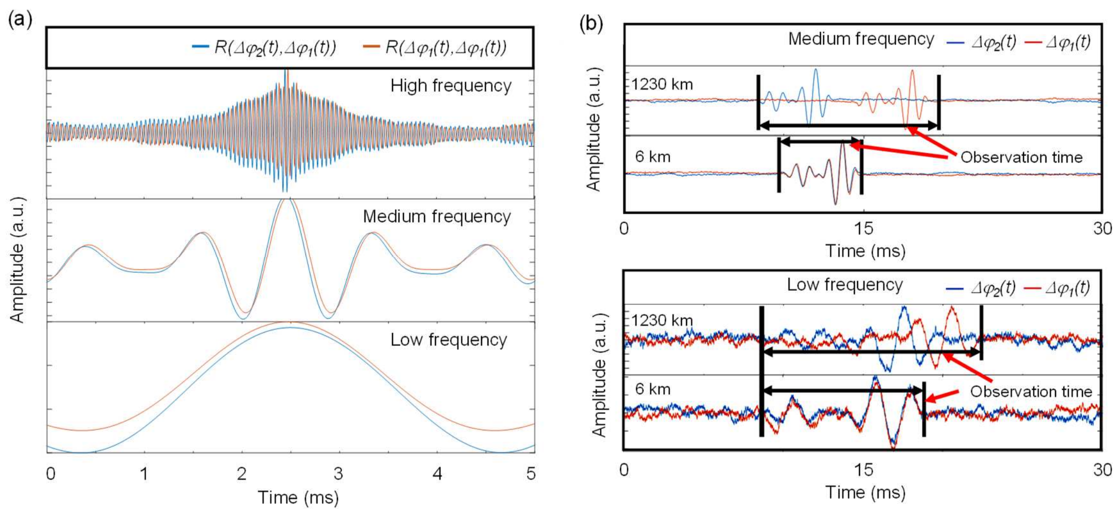

Figure 3.7 (a) Cross-correlation curves when three different vibrations are applied near the middle of the fiber link. (b) Comparisons of the observation time of low-frequency signals and medium-frequency signals when vibrations are applied at the beginning and end of the fiber link (1230 km) and at the middle of the fiber link (6 km), respectively.

Since the localization in this work relies on the determination of the time delay between two constructed differential signals, it is essential to investigate the scenarios when the time delay is small. To address this issue, we put the PZT at the middle of the fiber link. The same vibration signals are used to drive the PZT. Fig. 3.7(a) shows the cross-correlation curves of three vibrations. It is easy to observe the time delay between two correlation curves when vibration frequency is larger than 1 kHz, even though the fiber length is very short. However, one can see that for lower frequency vibrations, two correlation curves almost overlap. For the medium-frequency and low-frequency cases in our experiment, the decrease of the time delay between two differential signals leads to the decrease of the effective observation time, as shown in Fig.

3.7(b). As a result, the BT value decreases, which may result in a degraded localization performance, as shown in Fig. 3.8. The calculated mean of the fiber length for high-frequency vibrations is 6095.8 m with a difference of 2.7 m. The measurement result has accounted for the time delay caused by 1 km sensing fiber, 5 km TDF, an EDFA and an AOM. The calculated mean of the fiber length for medium-frequency vibration is 6153.4 m with a difference of 247.9 m. The calculated mean of the fiber length for low-frequency vibration is 5737.3 m with a difference of 4225.1 m. Results confirm that less than 5 m location accuracy can be obtained when vibration frequency is larger than 10kHz. The location accuracy for vibrations of around 1 kHz is less than 250 m. The location accuracy for vibrations of a few hundred Hz is less than 5 km.

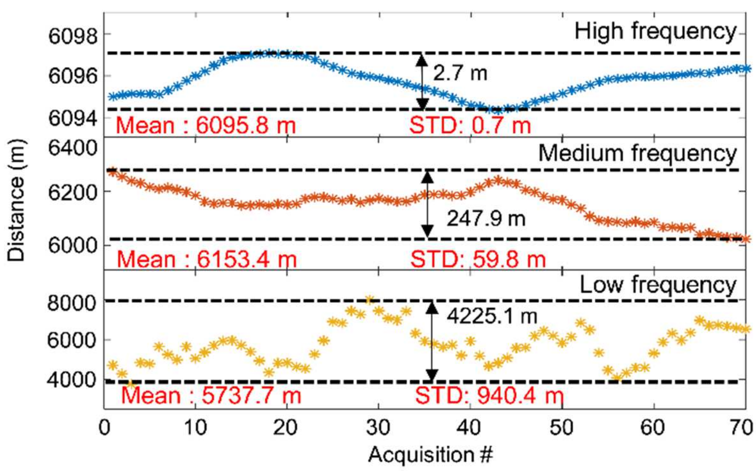

Figure 3.8 Location results when three different vibrations are applied near the middle of the fiber link. STD: standard deviation.

In order to investigate the lower bound of the frequency response of the sensing system, sinusoidal vibrations of different frequencies with a peak-to-peak voltage of 30 V were applied at the beginning and end of the fiber link. It is worth noting that both the demodulated phase signals and the constructed differential phase signals can be used to analyze the frequency component of the vibration in our system. For example, referring to Eq.(3.11) or Eq. (3.13), the measured phase variation caused by external vibrations is actually the sum of $\varphi_v(t)$ and $\varphi_v(t-\tau_{AB})$, where τ_{AB} is the time for light to propagate from point A to point B along the transmission path. Therefore, one can directly use the demodulated phase of the light to determine low-frequency components of vibrations, and the measured results are shown in Fig. 3.9. The detectable frequency can decrease to 5 Hz with an SNR of more than 10 dB. The phase noise of the fiber link was measured by removing the vibration from the fiber link as well. It is obvious that there exist several resonance peaks in the spectrum of the phase noise. We found it was due to the noises induced by the fans of two EDFA cluster mainframes we used in our experiment. As shown in Fig. 3.9 (b), the phase noise of the fiber link with different lengths was investigated. The resonance peaks exist in the spectra of the phase noise (shown as solid lines in Fig.3.9 (b) until the EDFA modules are removed (shown as the dashed lines in Fig. 3.9(b)). In this sensing scheme, sub Hz frequency detection can be reached by using ultra-stable lasers [130].

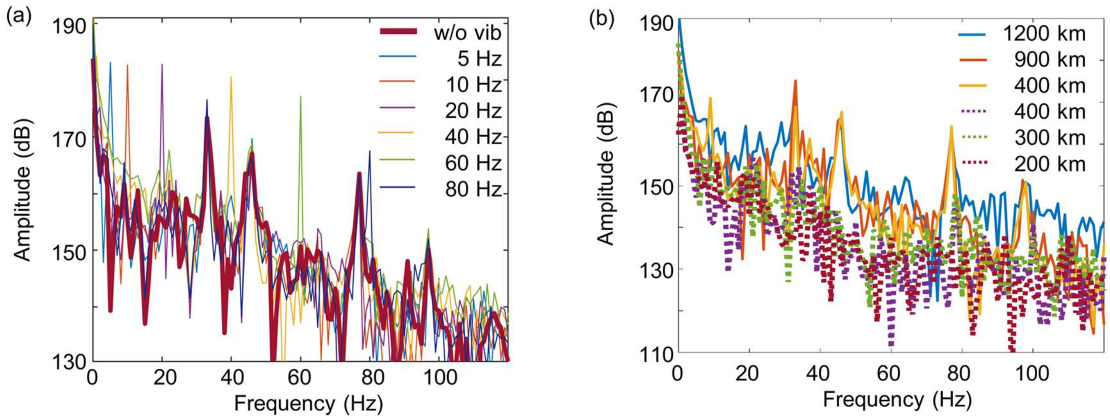

Figure 3.9 (a) The retrieved frequency spectra after FFT of the phase signals when vibrations with different frequencies are applied at the beginning and end of the fiber link; (b) the retrieved background noise spectra of fiber link with different lengths after FFT of the phase signals with (solid line) or without (dashed line) HUAWEI EDFAs.

3.7 Discussions

3.7.1 Advantages of the proposed sensing scheme

There are several advantages of the proposed scheme.

1) Ultrabroad frequency sensing range

In the proposed DOFVS, the demodulated phase signals, containing the cumulative phase information $\varphi_v(t)+\varphi_v(t-\tau_{AB})$, which is much more sensitive to low-frequency vibrations, are used to extend the system response to lower frequencies. Besides, since the vibration signal is continuously sampled, the upper bound of the detectable frequency is only limited by the bandwidth of the photodetector and the sampling rate set by the oscilloscope. Therefore, ultrabroad frequency response can be realized in such a sensing system.

2) Ultralong sensing distance

Because the sensing light is unidirectionally forward transmitted in the sensing fiber, the RBN problem is eliminated. Besides, the intensity of the forward transmitting signal is much stronger than the backscattering signal, and optical amplification can be easily realized using EDFAs, which enables ultralong haul sensing.

3) Large dynamic range

In the φ-OTDRs, the phase unwrapping failure is a problem if the vibration has both high frequency and large amplitude. Such failure is no more a problem in the proposed DOFVSs as the phase of the light is continuously sampled and retrieved. Besides, since the intensity signal is not linearly related to the external vibration in intensity detection-based optical fiber interferometers, undesirable higher-order harmonics occur when the vibration amplitude is very large, resulting in incorrect measurement. The proposed sensing scheme solves this problem as the phase of light, which is proportional to the vibration amplitude, is used to detect external vibrations.

4) Immune to the polarization fading effect

Polarization fading effect can be avoided because polarization diversity is used.

3.7.2 The need for location calibration

In this sensing system, EDFAs, BPFs, and variable optical attenuators (VOAs) are used in each span. Consequently, the measured length of the FUT has accounted for the lengths of all the EDFAs, BPFs, VOAs, TDF, AOM, couplers and fiber jumpers. As a result, it is necessary to calibrate the total length of the FUT prior to deployment. We measured the lengths of the 15 fiber spans using an OTDR with ±6m distance accuracy (100-km range). The measured lengths of the 15 fiber spans are 70.509 km, 75.377 km, 75.811 km, 68.859 km, 90.468 km, 92.554 km, 90.506 km, 99.134 km, 70.512 km, 100.951 km, 90.435 km, 69.121 km, 69.794 km, 90.959 km, and 74.805 km, respectively. Therefore, the total length of these 15 fiber spans is 1229795 km. In particular, EDFAs typically use 10-50 m of EDF for optical amplification and the use of BPFs and VOAs may contribute 1-2 m fiber length to each fiber span. Finally, the computed total length of the FUT is around 1235.372 km in our experiment. To accurately obtain the location information, the computed result is needed to be calibrated. The proposed DVS uses a fiber pair as the sensing part and hence the sensing range is half of the length of sensing fiber while the spatial resolution is defined as half of the location accuracy. That means the sensing range in this experiment is 615 km. The spatial resolution for vibrations of larger than 10kHz is less than 2.5 m. The spatial resolution for vibrations of around 1 kHz is less than 125 m, and the spatial resolution for vibrations of a few hundred Hz is less than 2.5 km.

3.7.3 Location accuracy of low-frequency vibrations

In our experiment, because of the differential effect, the increasing power of the low-frequency noise and the lack of effective observation time of the low-frequency vibration (limited by the memory of ADC), the spatial resolution of vibrations with a few hundred Hz degrades dramatically. However, low-frequency detection is an important part of the distributed vibration sensor because in some practical cases, e.g. for the submarine cables and buried cables, because of the attenuation of vibration signal during the transmission progress, only the low-frequency signals can be detected. Some methods can be used to improve the location accuracy of low-frequency vibrations. Referring to Eq. (3.27), the differential effect can be weakened by increasing the length of TDF. Therefore, the SNR of the low-frequency differential signals can be enhanced by using longer TDF. It is worth noting that the length of TDF is constrained by the system phase noise. If the length of TDF is too long, the correlativity between two differential signals will deteriorate as the phase noise caused signal variation is not neglectable, leading to an inaccurate location. Therefore, an ultra-stable laser with narrower line width [130] helps to extend the length of TDF by reducing the carrier phase noise. In practical applications, the length of TDF and the linewidth of the light source should be determined specifically, and the coherent length of the light source has to be larger than the length of TDF. Besides, for a certain sensing system, the noise floor is fixed, the SNR is linearly related to the amplitude of the external perturbation, better sensing performance can be obtained if the vibration signal has a larger amplitude. Meanwhile, according to the time delay estimation theory, longer effective signal observation time also contributes to better location accuracy.

3.7.4 The null points in the frequency spectrum

Due to the influence of the differential effect, vibration signals with lower than 100 Hz frequencies cannot be demodulated using the constructed differential phase signal in this work. In that case, only the demodulated phase signal, which is the summation of $\varphi_v(t)$ and $\varphi_v(t-\tau_{AB})$, can be used for lower than 100 Hz vibration sensing. In section 2.1.4, it is mentioned that there are a series of null points in the frequency spectrum of the signal that is formed by the sum of two signals with a certain time delay. Considering the vibration signal a sinusoidal wave with a frequency of f_{vib}, the accumulation phase signal $\varphi_v(t)+\varphi_v(t-\tau_{AB})$ can be derived as

$$\begin{aligned}\varphi_v(t)+\varphi_v(t-\tau_{AB}) &= \varphi_0\sin(2\pi f_{vib}t)+\varphi_0\sin(2\pi f_{vib}(t-\tau_{AB})) \\ &= 2\varphi_0\sin(2\pi f_{vib}(t-\tau_{AB}/2))\cos(\pi f_{vib}\tau_{AB})\end{aligned}. \tag{3.28}$$

When the following condition , K is an integer, is satisfied, the phase change caused by external vibrations will be zero. That means in the frequency spectrum of the phase signal, there exist a series of null frequency points, which satisfy . The existence of null frequencies makes the detection of vibrations with certain frequencies invalid. Besides, the interval of the null frequency points is inversely proportional to the time delay. That means the number of null frequency points will be larger if the vibration occurs closer to the beginning and end of the fiber link.

However, when the vibration frequency is larger than 100 Hz, the differential phase signal can be used for sensing. For the differential phase signal, according to Eq.(3.27), when $f_{vib}\Delta\tau$ is an integer, $\Delta\varphi_2(t)$ will be zero. That means in the frequency spectrum of the constructed differential signal, there also exist a series of null frequency points, which satisfy $f_{null,diff} = M / \Delta\tau$, M is an integer. The frequency interval between two consecutive null points is $\Delta f_{null,sum} = 1/\Delta\tau$. Since the length of TDF is fixed, the null frequencies of the differential phase signals are fixed.

At some special locations, the null frequency points can simultaneously exist in the frequency spectrum of the phase signal and the frequency spectrum of the constructed differential signal when the following conditions are satisfied.

$$\begin{aligned} & (K+1/2)/\tau_{AB} = M/\Delta\tau \\ & \rightarrow (K+1/2)/(nL_f/c) = M/\Delta\tau \\ & \rightarrow L_f = (K+1/2)c\Delta\tau/nM \end{aligned} \tag{3.29}$$

Therefore, except for these special locations, the null frequency point cannot simultaneously exist in frequency spectra of $\varphi_b(t)$ (or $\varphi_{IF}(t)$) and $\Delta\varphi_2(t)$ (or $\Delta\varphi_1(t)$). Therefore, the occurrence of the null frequency points is largely reduced, which makes the detection of vibration frequencies much more reliable.

3.7.5 The system's sensitivity

In the proposed scheme, the measurand is the integration of the phase change induced by the external vibration when light propagates through the whole vibration area. The phase change can be written as

(3.30)

where $\Delta\varepsilon_v$ is the vibration induced change of the fiber strain, which is linearly related to the amplitude of the vibration event; L_v is the distribution range of the vibration event. Eq.(3.30) indicates that when the vibration influenced range is wider, the system's sensitivity is higher.

Since the integration of the phase change is used for sensing, this sensing system can only tell the location of the vibration while it cannot tell the distribution range of the vibration. But it can tell whether the event is moving by comparing the location results over time.

3.7.6 The location of multi-point vibration

In this work, the sensing performance of single-point vibration was investigated. In real systems, multi-point vibrations are inevitable to occur simultaneously over such an ultralong sensing range. Since the cross-correlation-based time delay estimation is used to determine the locations, multiple vibration points can only be distinguished in case these vibration signals are uncorrelated. A proof of concept experiment on multi-point sensing was also conducted. Two PZTs, which are driven by two random noise signals generated separately by two arbitrary waveform generators (Agilent 33120A and BK Precisions 4065B) both with peak to peak voltages of 20 V, are placed at different positions (60 km apart). Experimental results of these two independent vibrations occurring at different places simultaneously are shown in Fig. 3.10. The sampling rate was set as 400 MSa/s. It is obvious that there are two peaks in the cross-correlation curve. The measured time delay is 4.5592775 ms and 3.9676825 ms, corresponding to fiber lengths of 929821 m and 809171 m, respectively. The fiber length difference is 120650 m, which means the distance between two vibration locations is 60325 m. With the decrease of the interval between two vibration locations, peaks shown in the cross-correlation curve will get closer and finally cannot be distinguished. Besides, if the power difference between different vibration signals is very big, the correlation peak corresponding to the weaker will be buried, leading to the failure of the detection of weaker signals.

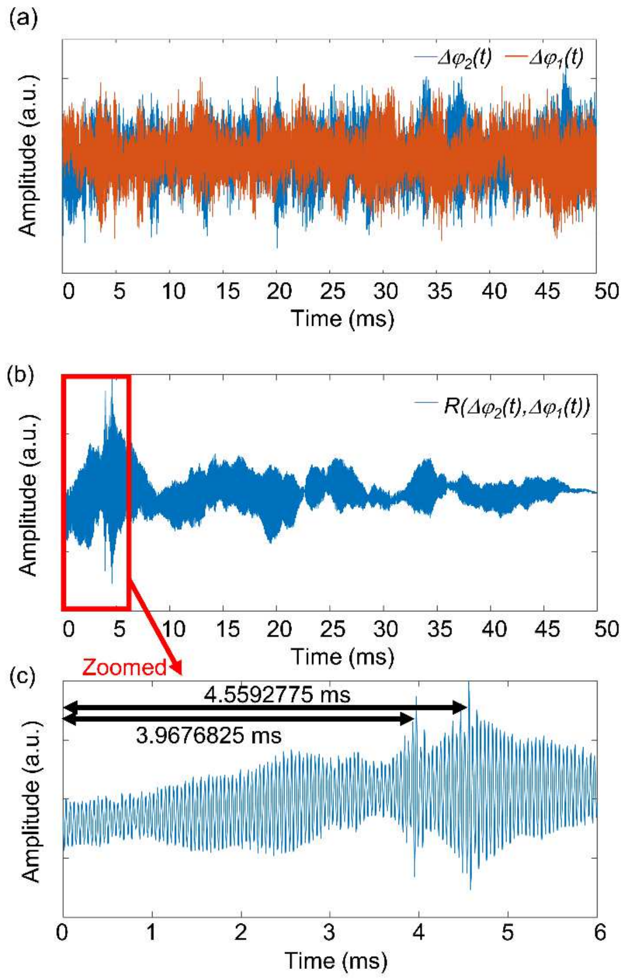

Figure 3.10 (a) Two constructed differential phase curves and (b) the cross-correlation curve when two independent noise vibration signals are applied at two different locations of the fiber link. (c) a zoomed section of (b).

3.7.7 The influence of the ASE noise

In the real environment, multiple channels based on WDM can be carried on such an ultralong fiber link. In that case, the bandwidth of the BPF should be increased to cover all the channels, which means the increase of in-band ASE noise in terms of the sensing signal. The in-band ASE noise will be repeatedly amplified during forward transmission. Therefore, the optical SNR degrades with the increase of the sensing distance, which sets an upper limit of the sensing distance. However, due to CW operation, the bandwidth of the sensing signals can be very small, which helps to maintain an excellent SNR at the receiver, making it possible to further extend the sensing range.

3.8 Summary

In this chapter, we have demonstrated a novel optical vibration sensing technique based on forward transmission and coherent detection using a pair of optical fibers deployed at the same location with a loop-back configuration. An FS-ODL structure with an AOM and a TDF is used for event localization. Ultra-broad-frequency detection from infrasound to ultrasound can be realized in this sensing scheme. Less than 125 m spatial resolution over 615 km sensing range can be obtained when vibrations of larger than 1 kHz occur on the fiber link. Compared with reported distributed vibration sensors, the proposed scheme has a much simpler structure and enables ultra-long distributed vibration sensing. The sensor has excellent localization performance of vibrations containing larger than 1 kHz frequency components. In real applications, events like train running on a railway track, knocking and hammering will induce vibrations of more than 1 kHz on the sensing fiber. That means the proposed sensing scheme has powerful application potential for these sensing cases.

Chapter 4

Simplified unidirectional ultra-long DOFVS

In this chapter, the sensing structure of unidirectional transmission-based DOFVS proposed in chapter 3 is further simplified by removing the FS-ODL structure. The loop-back configuration in this sensing system is formed by directly splicing the far ends of two sensing fibers. Since the sensing system works at the baseband, the data processing load is largely reduced. Besides, by analyzing the null point in the frequency spectrum of the extracted phase signal, the localization of multi-point vibration can be easily realized. The sensing performance of both single-point vibrations and multi-point vibrations is analyzed in detail in this chapter. The localization of single-point and multi-point vibrations with measurement errors of less than ±100 m and ±200 m, respectively, over a 500 km sensing range is demonstrated.

4.1 Introduction

In chapter 3, a new ultralong distance DOFVS scheme based on unidirectional forward transmission light and polarization diversity coherent detection has been proposed and demonstrated. The sensing distance has been extended to over 600 km. Although multi-point vibration can be realized through time delay estimation in that sensing scheme, it is only valid when following conditions: 1). vibration positions are far away; 2). vibration signals are uncorrelated and 3) the power difference between different vibration signals is not very big; are satisfied simultaneously. Besides, the sampling rate of the proposed sensing system must be at least twice as high as the frequency shift induced by the AOM due to the use of FS-ODL, which largely increases the load of data processing. Since the location information is contained in the frequency spectrum of the phase signal due to the existence of null frequency points, the multi-point location can be easily acquired by analyzing the null frequency. Therefore, in this chapter, the sensing structure is further simplified and the location performance based on analyzing the null frequency is investigated.

4.2 Location methods

The sensing scheme is shown in Fig. 4.1. Instead of using the FS-ODL, the far ends of two sensing fibers are spliced together to form a loop-back arrangement.

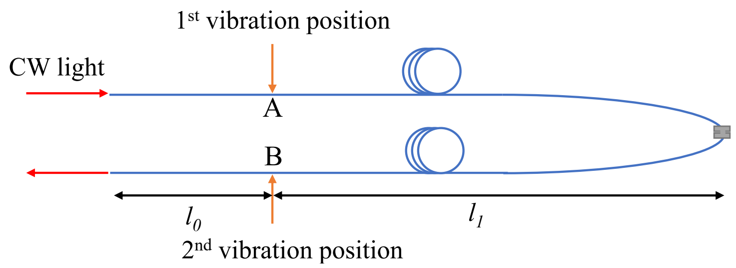

Figure 4.1 Schematic diagram of the sensing principle.

Through the analysis in chapter 3, we have the null frequency point determined by

, (4.1)

where l_1 is the distance from the vibration point to the loop center of the sensing fiber. The frequency interval between two consecutive null points can be derived as

$$\Delta f_{null} = c / 2nl_1 \tag{4.2}$$

Therefore, the distance l_1 can be obtained by determining the frequency interval between two consecutive null points. As the total length of the sensing fiber is already known, the location of the vibration can be finally determined. The frequency component of the demodulated phase signal, which is the baseband phase signal here, can be analyzed by applying FFT. We denote the FFT of $\varphi_b(t)$ as $\hat{\varphi}_b(f)$, which can be derived as

$$\hat{\varphi}_b(f) = \left[\hat{\varphi}_{nb}(f) - \hat{\varphi}_{LO}(f)\right] + \hat{\varphi}_v(f)(1 + e^{-j2\pi f \tau_{AB}}) \tag{4.3}$$

There are two ways to determine the frequency interval Δf_{null}. Referring to Eq.(4.1) and Eq.(4.2), the frequency interval can be determined by

$$\Delta f_{null} = f_{K^{th}null} / (K + 0.5) \tag{4.4}$$

Therefore, one method is to determine the frequency of the K^{th} null point first. Then the frequency interval Δf_{null} can be calculated using Eq.(4.3). The detailed processing procedures are:

1) Applying an adaptive digital low pass filter to remove the high-frequency noise of the frequency signal $\hat{\varphi}_b(f)$ and then obtain a smooth frequency curve where null points are clearly displayed;
2) Roughly determine the frequency interval Δf_{rough} by subtracting the frequency values of two consecutive null points;
3) Choose a null point with sharp dip and find out the corresponding frequency value $f_{K^{th}null}$;
4) Determine the integer K by rounding the value calculated by ($f_{K^{th}null} / \Delta f_{rough}$ - 0.5);
5) Finally determine the frequency interval using Eq.(4.4).

According to Eq.(4.1), the measured location can be expressed as

$$l_1 = c(K+0.5)/2n\, f_{k^{th}null} \tag{4.5}$$

The measurement variance of the location can then be written as

$$\Delta l_1 = c\Delta f_{K^{th}null}(K+0.5)/2nf^2_{K^{th}null} = c\Delta f_{K^{th}null}/2n\Delta f_{null} f_{K^{th}null} \tag{4.6}$$

where $\Delta f_{K^{th}null}$ is the measurement variance of the K^{th} null frequency.

The other method is using the double FFT algorithm [131], in which a second time FFT is applied to the frequency spectrum of the phase signal. The frequency interval between two consecutive null points is determined by figuring out the peak in the second time FFT spectrum. In our case, the detailed processing procedures are

1) A section of the sensing signal is obtained from the scope; the spectral component of the demodulated phase signal $\hat{\varphi}_b(f)$ is calculated.
2) Because the power of the phase noise is inversely proportional to the noise frequency, there is a downtrend on the calculated frequency signal $\hat{\varphi}_b(f)$. Therefore, the downtrend $D(f)$ is first obtained by fitting the curve $\hat{\varphi}_b(f)$.
3) Remove the downtrend by subtracting $D(f)$ from $\hat{\varphi}_b(f)$.
4) A section of $\hat{\varphi}_b(f)$ after removing the downtrend that contains the effective information is intercepted.
5) To enhance the resolution of the second time FFT spectrum, zeros are padded to the end of the intercepted first time FFT signal.
6) Apply second-time FFT to the processed first-time FFT signal.
7) Estimate the value of the spectral peak shown in the second time FFT spectra.

In the double FFT method, assuming that the frequency range of the first time FFT signal after zero padding is F, and the value of the peak in the second time FFT spectra is P, the corresponding frequency interval between two consecutive null points should be

$$\Delta f_{null} = F / P \tag{4.7}$$

According to Eq.(4.2) and Eq.(4.7), the vibration location should be

$$l_1 = cP / 2nF \ . \tag{4.8}$$

That means the measurement variance of the location is

$$\Delta l_1 = c\Delta P / 2nF \ . \tag{4.9}$$

where ΔP is the measurement variance of P. To estimate the peak value more precisely, Gaussian fitting can be applied on the second time FFT curve. In this work, both of these two location methods were used to investigate the sensing performance and comparisons between these two methods were conducted as well. Fig.4.2 shows the data processing procedures of these two methods.

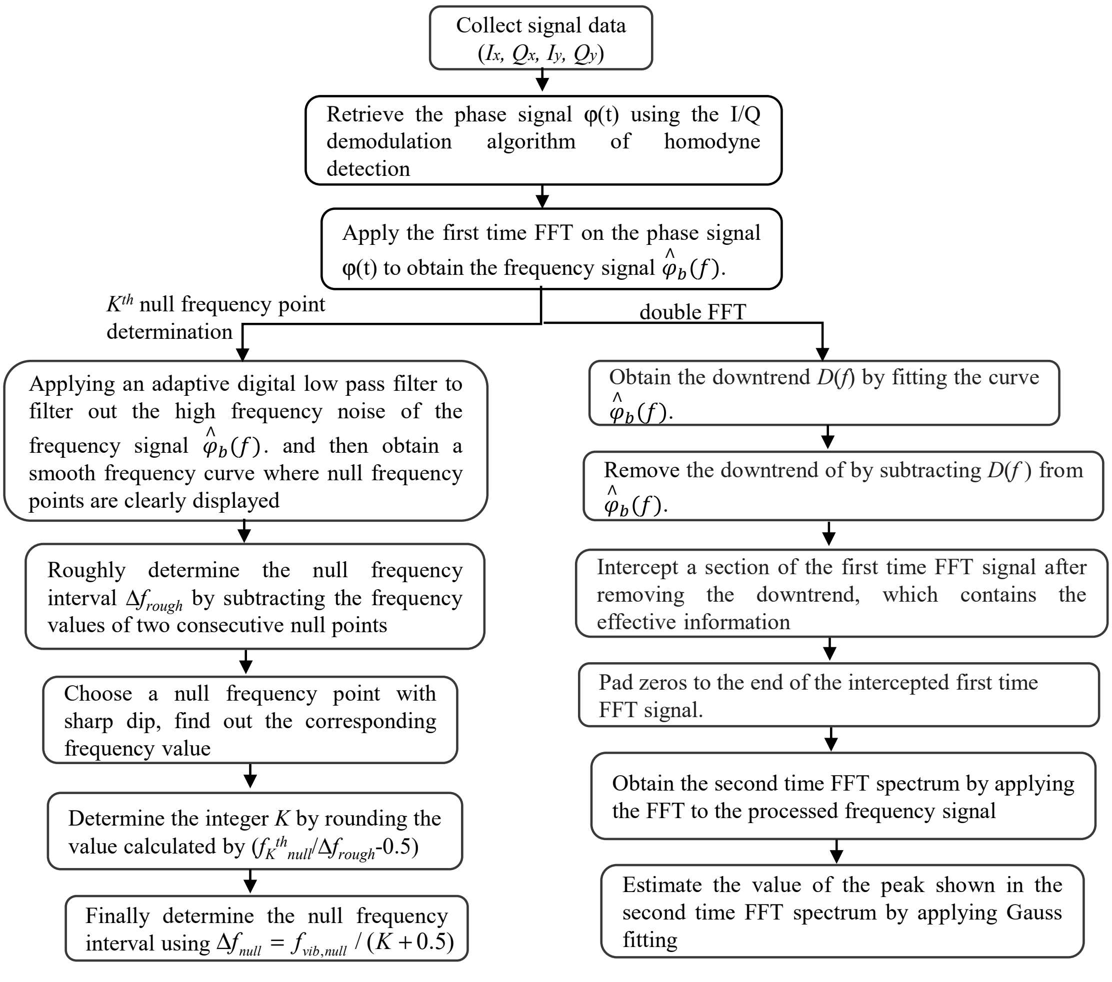

Figure 4.2. The flow chart of the data processing procedures of two location methods.

4.3 Experiment setup and Results

4.3.1 Experimental setup

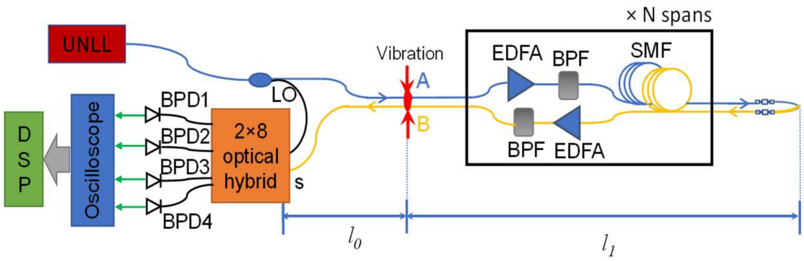

Figure 4.3 Experiment setup of the proposed ultra-long distributed vibration sensing scheme. UNLL: ultra-narrow linewidth laser; EDFA: erbium doped fiber amplifier; BPF: band-pass filter; SMF: single mode fiber; LO: local oscillator; BPD: balanced photodetector; DSP: digital signal processing.

The experimental setup of the simplified ultralong DOFVS based on unidirectional forward transmission light is schematically shown in Fig. 4.3. The output of an ultra-narrow-linewidth CW tunable laser operating at 1550 nm was split into two branches. The upper branch was launched into the FUT directly for sensing. The lower branch was served as an LO. The FUT was a 1000 km fiber link, consisting of 14 spans of SSMF (G.652D). An EDFA and a 4-nm BPF were utilized in each span to compensate for the loss induced by the fiber and to remove the out-of-band ASE noise, respectively. Two sensing fibers were placed close to each other to ensure the same external vibration-induced phase change of the propagation light. Without loss of generality, parts of two fibers, where the external vibrations were applied, were glued together to simplify the experiment procedure. The far ends of two fibers are spliced together to form a loop-back arrangement. After propagating through the 1000 km fiber link, a phase and polarization-diversity homodyne coherent receiver consisting of a polarization-diversity optical 90° hybrid mixer and four BPDs with 500 MHz bandwidth were used to detect the beating signals between the output signal light and LO. By using a digital oscilloscope, the detected analog signal was digitized and then transferred to a computer for further signal processing.

4.3.2 Location result of single-point vibration

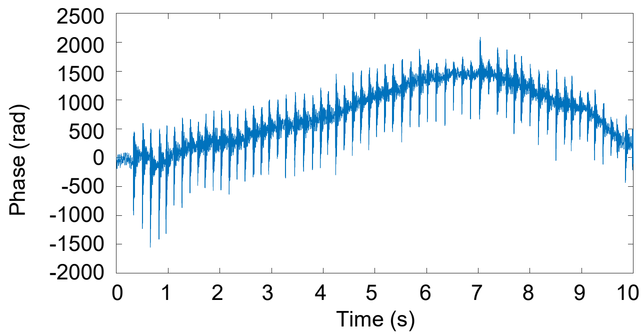

Figure 4.4 The demodulated phase signal when hammering disturbance is applied at the position of 200 km.

Firstly, single-point vibration was investigated. In order to emulate the practical circumstance, vibrations were separately applied at three different positions, i.e., 500km, 200 km, and 12.5 km from the loop center of the fiber link. To emulate the intrusion event, the vibration signal was introduced by continuously hammering a fiber spool, which is wrapped by two 10 m single-mode fibers that are glued together. The collection time was 10 s for a single shot sampling and the sampling rate was set as 4.8 MSa/s. The phase signal retrieved from the collected data is shown in Fig. 4.4, where obvious phase changes can be found when external vibrations occur. As the hammering continues, a series of peaks can be observed on the phase curve, whose intervals are corresponding to the hammering period. One may also find from Fig. 4.4 that the phase of the received signal slowly fluctuates even before vibration was applied. This may be attributed to the following causes: 1) environment temperature fluctuation, which may induce length variations of the optical path; 2) acoustic noise along the propagation path and, 3) the carrier phase noise. By applying FFT to the demodulated phase signal, the frequency spectrum can be obtained. Fig. 4.5 shows the frequency spectra of the demodulated phase signals after FFT when vibrations were applied at three different positions. A series of dips (null points) appear in the spectra. The key point of locating the external vibration is to determine the frequency interval between two consecutive null points precisely.

For the K^{th} null point determination method [referring to Eq.(4.6)], the measurement error of the K^{th} null frequency will have a dramatic impact on the accuracy of the localization.

Therefore, an adaptive low pass filter was used to remove the high-frequency noise to decrease the measurement error. Figs.4.5(d-f) show the finally obtained null-frequency curves after removing the high-frequency noise. Since the measurement accuracy is inversely proportional to the value of K^{th} null frequency, a large value of K^{th} null frequency helps to reduce the measurement error. Besides, from Fig.4.5 (e) and (f), the first time FFT signals have high SNRs near the frequency of 9 kHz. Therefore, the value of K^{th} null frequency in this experiment is chosen around 9 kHz.

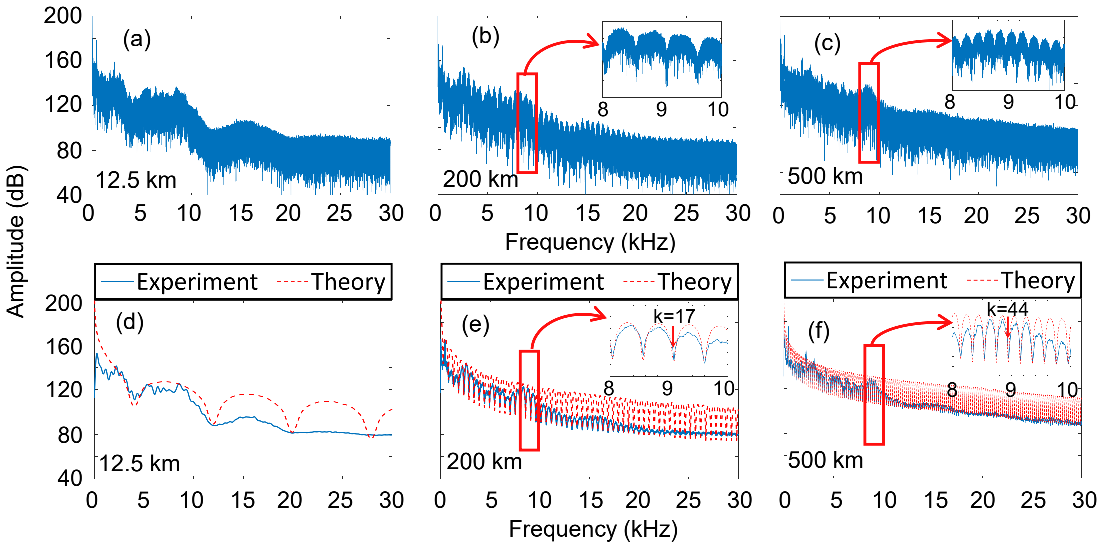

Figure 4.5 Original frequency spectra of the demodulated phase signals when disturbance is applied at positions of (a) 12.5 km, (b) 200 km and (c) 500km, respectively. (d), (e) and (f) are frequency spectra obtained by applying a low pass filter on (a), (b) and (c), respectively.

As shown in Fig. 4.5 (f), for the position of 500 km, the 45th null point (K=44) was chosen to determine the frequency interval. As shown in Fig. 4.5 (e), for the position of 200 km, the 18th null point (K=17) was chosen. When the vibration occurs at the position of 12.5 km, as shown in Fig. 4.5(d), there are just two null points in the spectrum and only the first null point is sharp and clear, so the first null point was chosen for the localization. To investigate the location error of this sensing scheme, the hammering tests on the above-mentioned three different positions of the fiber link were all repeated 100 times. Fig. 4.6 shows the location results. Each vibration position was measured by a commercially available OTDR with a resolution of 5 m as a reference. Compared with the results obtained by using OTDR, one can see that the location error is less than ± 100 m.

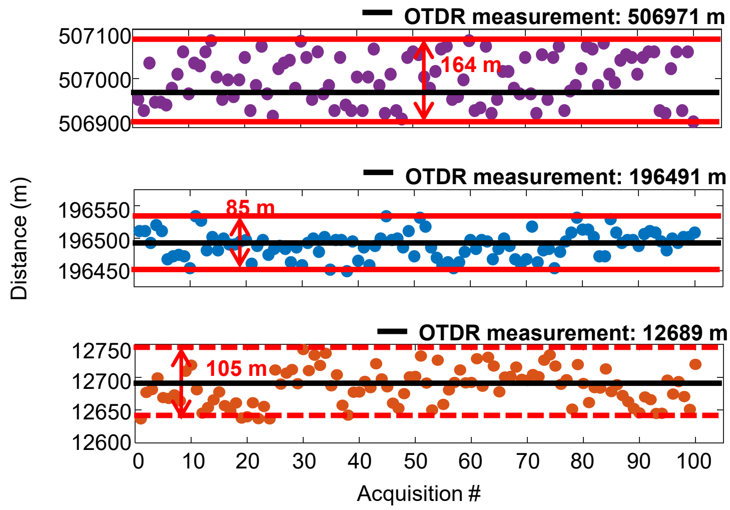

Figure 4.6 The location results obtained by using the K^{th} null frequency determination method when vibrations occur at three different vibration positions.

Next, the double FFT algorithm was used to process the data as well. In this work, the frequency range of the intercepted signal was from 0 Hz to 30 kHz. Equation (4.9) indicates that the location accuracy is inversely proportional to the frequency range of the first time FFT signal after zero padding. Therefore, the frequency range of the first time FFT signal is extended to 0 Hz-1MHz to ensure a good location estimation. Fig. 4.7 shows the obtained spectra after the second time FFT when vibrations occur at three different positions. From Fig. 4.7 (c), one can see that the peak in the second time FFT spectrum for vibrations occur at the position of 12.5 km is not obvious. That is because there are only 3 null points in the frequency range of 30 kHz, which is not enough for the second time FFT. One can therefore deduce that the double FFT algorithm is valid when 1) a long acquisition time is applied; and/or 2) vibrations are occurring farther away from the loop center. As shown in Figs. 4.7 (a) and (b), by applying Gaussian fitting, the value of the peak in the second time FFT spectrum can be determined. The location can thus be calculated using Eq.(4.8). Fig. 4.7(d) shows the location results obtained by using the double FFT algorithm. The location error of the double FFT algorithm is less than ± 200 m.

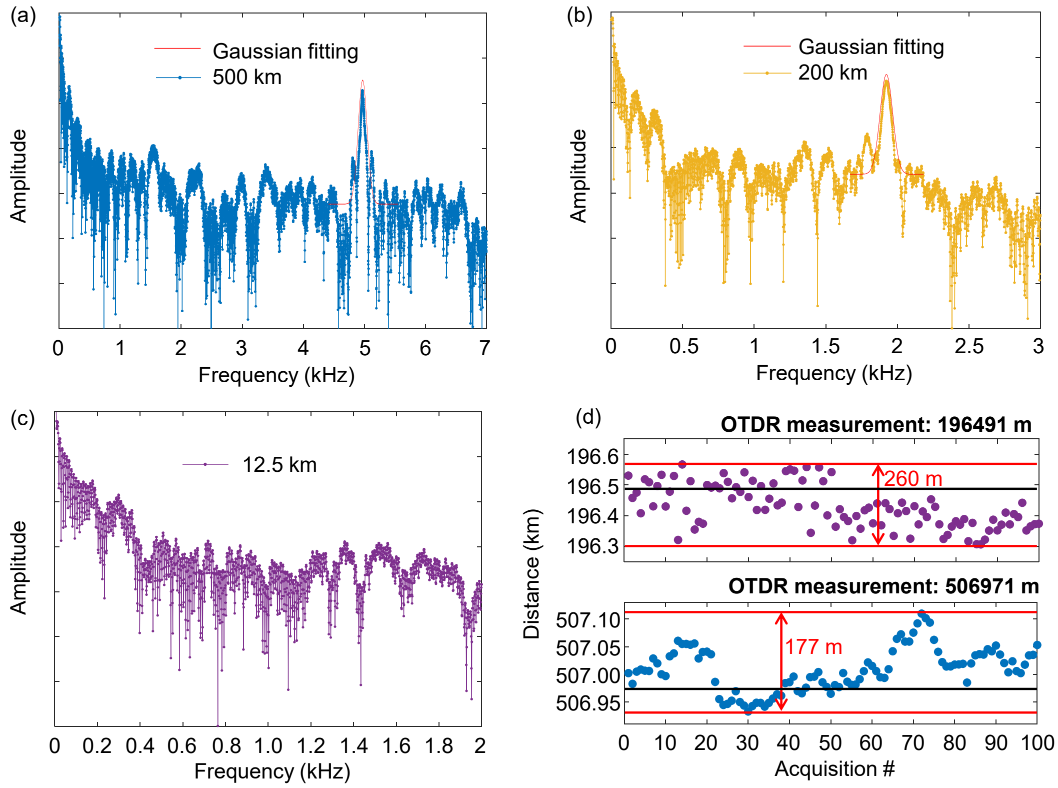

Figure 4.7 The second time FFT spectra obtained by applying the FFT on the first time FFT signals $\hat{\varphi}(f)$ when single-point vibrations occur at three different positions (a) 500 km, (b) 200 km and (c) 12.5 km, respectively. (d) Location results obtained by using the double FFT algorithm when vibrations occur at positions of 200 km and 500 km.

4.3.3 Location result of multi-point vibrations

For single-point vibration cases, the location can be easily obtained by finding out the frequency interval between two consecutive null points as mentioned above. However, in practical ultra-long sensing systems, multiple vibrations may occur simultaneously at different positions along the sensing fiber. For multi-point vibration cases, the demodulated phase is the superimposing of multiple vibration signals. In that case, the frequency spectrum of the demodulated phase after FFT should be written as

(4.10)

where U represents the U^{th} vibration position and V is the total number of vibration positions.

To investigate the multi-point vibration sensing performance, two PZTs are placed at positions of 45 km and 165 km from the loop center of the fiber link. Two 10 m fibers are wrapped around these two PZTs, separately. Vibrations are introduced by driving the PZTs using two random Gaussian-noise-like electrical signals both with a peak to peak voltage of 10 V. Fig.4.8 (a) shows the frequency spectrum when two vibrations occur simultaneously. Because the retrieved phase signal is a superposition of two vibration signals, the null points in the spectrum are indistinctive. In such cases, only the double FFT algorithm can be used to determine the frequency interval effectively.

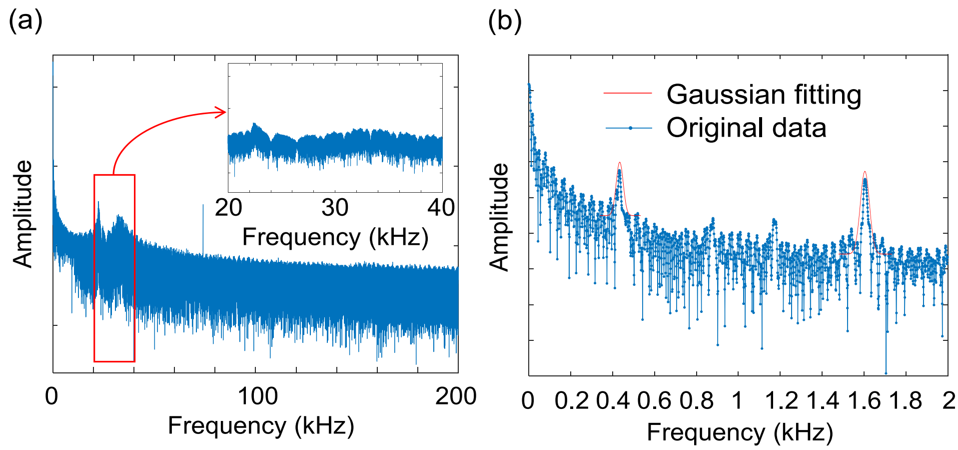

Figure 4.8. (a) A zoomed region of the frequency spectra of the demodulated phase signals when vibrations occur at two different points simultaneously. (Inset) the whole spectra. (b) The second time FFT spectra.

Here, a section of data with a frequency range from 0 Hz to 200 kHz was acquired, and the frequency range was extended to 0 Hz-1 MHz as well. Fig. 4.8 (b) shows the result after the second time FFT. There are two peaks shown in the spectra, representing two vibration positions. The exact value of each peak is determined by using Gaussian fitting. The values for these two peaks are 436.338 and 1618.698, respectively. According to Eq.(4.8), the corresponding locations are 44493 m and 165094 m, respectively. Fig. 4.9 shows the location results of 100 times repetitive tests. The location error is less than ± 200 m. The location accuracy of multi-point vibrations is higher than that of single-point vibration. That is because a larger effective frequency range of 200 kHz is obtained in the multi-point case. It should be noted that the location error can be further decreased if the vibration signal has a wider effective frequency span. Localization of two-point vibrations has been verified in this work and it is obvious that the double FFT method can be used for multi-point (larger than two) vibrations as well.

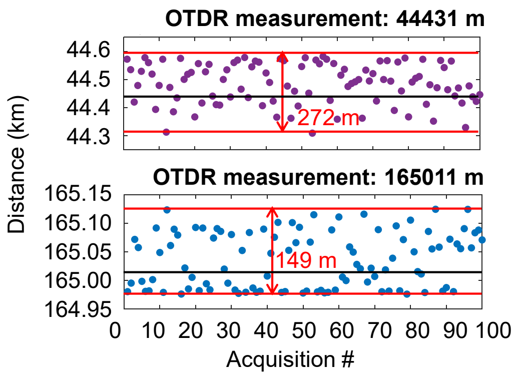

Figure 4.9 The location results obtained by using the double FFT algorithm when vibrations occur simultaneously at positions of 45 km and 165 km.

4.4 Discussions

In this work, two methods have been used to determine the location of external vibrations. For the K^{th} null frequency determination method, referring to Eq.(4.6), it is obvious that the location accuracy is linearly related to the measurement variance $\Delta f_{K^{th}null}$, however, inversely proportional to Δf_{null} and the frequency of K^{th} null point. Therefore, the higher location accuracy can be obtained when the null frequency dip is clearer and sharper, the null frequency interval is larger and the frequency of the K^{th} null point is higher. As the value of $f_{K^{th}null}$ is fixed in our case, i.e. around 9 kHz, comparing the location results of positions of 500 km and 200 km, the location accuracy of the vibration position of 200 km is higher. Besides, as for the location results of vibrations occurring at the 12.5 km position, even though the null frequency dip is not sharp, because the null frequency interval is very large, the measurement error is not very big, even smaller than that of vibrations occurring at the position of 500 km. From the location results of both the single-point vibrations and multi-point vibrations using the double FFT algorithm, it is obvious that the location accuracy deteriorates when the vibration position moves towards the loop center of the fiber link. That is because the vibration occurring farther away from the loop center has a higher SNR of the spectral peak shown in the second time FFT spectra. For the double FFT algorithm, the location error is larger than that using the K^{th} null frequency determination method. The reason is that the location accuracy obtained using the double FFT algorithm is related to the effective frequency span of the vibration signal. A small frequency span of the hammering events, which is 30 kHz in our case, leads to a large location error. Besides, the double FFT algorithm is not effective for vibration events occurring close to the loop center of the fiber link. Comparing the K^{th} null frequency determination method and the double FFT algorithm, it is obvious that the K^{th} null frequency determination method is more appropriate for the single-point vibration detection. However, for multi-point vibrations, the K^{th} null frequency determination method is invalid. Only the twice FFT can be used to locate the vibration.

In this work, since the vibration location is determined by analyzing the null frequency shown in the frequency spectrum of the phase signal, the phase noise of the system will influence the sensing performance significantly. In order to reduce the phase noise, a light source with coherent length longer than the length of sensing fiber has to be used.

The proposed sensing scheme realizes the ultralong-distance vibration sensing using a simple sensing structure. The use of the double FFT algorithm makes the location of multi-point vibration much easier. Besides thanks to the use of the baseband signal, the load of data processing is largely reduced.

4.5 Summary

In this chapter, we have proposed and experimentally demonstrated a unidirectional ultra-long distance distributed optical vibration sensing technique using coherent detection, where a pair of optical fibers are deployed at the same location with a loop-back configuration. Both the K^{th} null frequency determination method and double FFT algorithm have been used to investigate the sensing performance. Less than ± 100 m location error of single point vibrations and less than ± 200 m location error of multi-point vibrations have been realized over a 500 km sensing range. The proposed sensing structure is much simpler than other reported long-haul and ultralong haul sensing systems. All these make the proposed scheme a good candidate for ultra-long DOFVSs.

Chapter 5

Dynamic BOTDA based on SEFDM

BOTDA plays an important role in dynamic DOFSs due to its capability of detecting low-frequency dynamic signals with large dynamic range. As discussed in chapter 2, the spatial resolution of OFDM-BOTDA is limited because of the tradeoff between the spatial resolution and subcarrier spacing. Therefore, to alleviate the limitation, a dynamic BOTDA employing the SEFDM technique is proposed in this chapter. SEFDM is a multi-carrier signaling technique, through which subcarriers are packed closer by compromising the orthogonality of OFDM. Due to the violation of the orthogonality between subcarriers, the length of an SEFDM symbol can be much shorter than an OFDM symbol, taking the same subcarrier spacing into consideration. As a result, the spatial resolution can be largely improved. By using the SEFDM signal as the probe wave, the time-consuming frequency sweeping process is eliminated, which makes dynamic sensing possible. The interference caused because of the overlapping between two symbols, which is known as the ISI, influences the performance of SEFDM systems greatly. Therefore, in this chapter, both numerical simulation and experiments are conducted to demonstrate the influence of ISI in SEFDM BOTDAs. After that, the sensing performance of the SEFDM BOTDA is experimentally investigated. Results show that a 3.1 m spatial resolution with 1.294 MHz measurement accuracy is reached over a 10 km sensing range. A dynamic measurement with a vibration frequency of 26 Hz is demonstrated.

5.1 The design of the SEFDM symbol for BOTDA applications

SEFDM, which is also known as the non-orthogonal frequency division multiplexing was first proposed in 2003 [132] to further improve the spectral efficiency of an optical communication system. The orthogonality between subcarriers in SEFDM systems is intentionally violated so that the frequency interval between adjacent subcarriers can be much compressed [133]. That means the period of the SEFDM symbol can be much shorter than that of the OFDM symbol with the same subcarrier spacing. As a result, the tradeoff between the spatial resolution and the frequency resolution imposed by the orthogonality between subcarriers in OFDM-BOTDA can be overcome. Similar to OFDM-BOTDAs as introduced in chapter 2, in SEFDM BOTDAs, consecutive but pulsed SEFDM frames are used as the probe light. Figure 5.1 shows the time-domain structure of an SEFDM probe signal. The first frame is used for time synchronization. Before each SEFDM symbol, a CP, i.e. a zero-suffix, is added to act as a guard interval to reduce the ISI. Therefore, each SEFDM frame is composed of an SEFDM symbol and a CP. The spatial resolution of an SEFDM-BOTDA is limited by the duration of each SEFDM frame.

Figure 5.1 The time-domain structure of an SEFDM signal.

The time-domain SEFDM signal is expressed as

$$s_{SEFDM}(t) = \sum_{x=0}^{S-1} c_x \exp(j2\pi x \Delta f_c t) \tag{5.1}$$

Discretize $s_{SEFDM}(t)$ in Eq. (5.1) by samples with a symbol duration T_{SEFDM}, we have [134]

(5.2)

where is the bandwidth compression factor (BCF). If , meaning the orthogonality condition is met and , becomes an OFDM signal. For SEFDM signals, , or , meaning that the orthogonality condition is violated and the symbol duration T_{SEFDM} is shorter compared with that of OFDM signals ($1/\Delta f_c$). Essentially, one can see from Eq. (5.2) that the SEFDM signal can be generated by discarding $S-S_1$ samples after S-point IDFT. The spatial resolution is limited by the symbol duration; hence a smaller ξ would produce a higher spatial resolution. Like OFDM-BOTDA, the BGS of an SEFDM-BOTDA is also obtained by channel estimation. As equi-powered and equi-spaced pilots are usually optimal for channel estimation [135], it is imperative to design the SEFDM symbol so that the subcarriers used for channel estimation remain quasi-flat even when a small ξ is used. The partial Zadoff-Chu (ZC) sequence provides such feasibility. Let us first define a complex-valued ZC sequence as [136]

$$z(a) = \exp(-j\frac{\pi a^2}{N_{ZC}}), \quad 0 \le a \le N_{ZC}-1, \quad N_{ZC} \text{ is even} \tag{5.3}$$

where N_{ZC} is the length of the ZC sequence. Then the partial ZC sequence is defined as data bits clipped from the complete ZC sequence, which can be expressed as

$$z_p(b) = \exp(-j\frac{\pi(b+y)^2}{N_{ZC}}), \quad b = 0,...,N_{pZC}-1, \quad y \in [0,\ N_{ZC}-N_{pZC}] \tag{5.4}$$

where y determines the starting point of the interception and N_{pZC} is the length of the partial ZC sequence. We define N_{pZC}/N_{ZC} as the partial percentage. $z_p(b)$ is then mapped to the subcarriers used for BGS estimation and transformed to the time domain via IDFT. It has been demonstrated in [137] that $z_p(b)$ is characterized as a centralized pulse in the time domain. Moreover, the time-domain signal gets more centralized when the partial percentage gets smaller. Therefore, the BCF ξ of the SEFDM signal can be decreased while the majority of the signal power is maintained along with the partial percentage, leading to a higher spatial resolution. In the proposed sensing scheme, since the IM/DD scheme is applied, Hermitian symmetry is applied to the subcarriers so that the time-domain SEFDM signals after IDFT can be real-valued. Therefore, the symbol used for IDFT can be written as

$$c_x = \begin{cases} z_p(x-w)\,, & w \le x \le w+N_{pZC}-1 \\ z_p^*(S-w-x), & S-w-N_{pZC}+1 \le x \le S-w; \quad 0 \le w < \dfrac{S}{2}-L \text{ and } 0 < N_{pZC} \le \dfrac{S}{2} \\ 0, & \text{elsewhere} \end{cases} \tag{5.5}$$

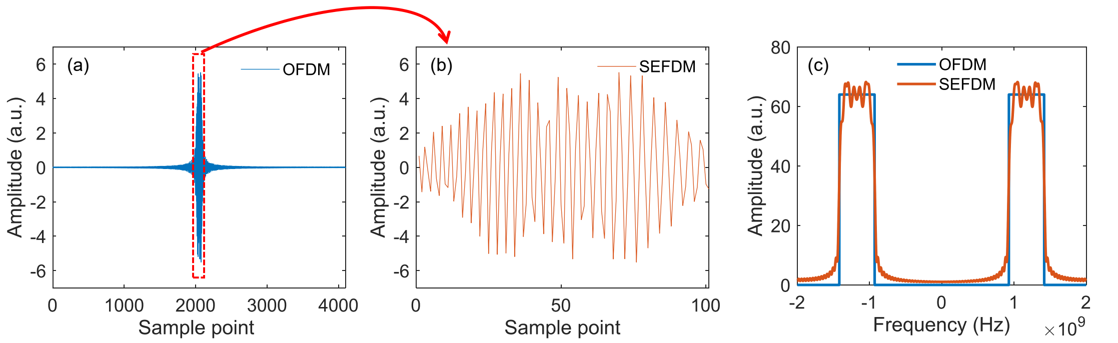

Figure 5.2 (a) the real-valued time-domain OFDM signal, (b) the corresponding intercepted SEFDM signal, and (c) frequency spectra of both signals.

Figure 5.2 (a) shows a real-valued time-domain OFDM symbol generated by loading a 500-bit partial ZC sequence on a subband of 500 subcarriers with 1 MHz frequency spacing (S=4096, T_s=0.25 *ns*, N_{ZC}=24576, y=12542, w=952, N_{pZC} =500). A 101-sample SEFDM symbol is generated by discarding the sidelobes of the pulse (S_1 = 101, $\xi = S_1 / S = 0.025$), as shown in Fig.5.2 (b). The frequency spectra of both OFDM and SEFDM signals are shown in Fig.5.2 (c). The SEFDM signals are padded with $S - S_1$ zeros to form an S- point signal before FFT is applied. One can see that the interception only causes slight energy variation within the signal band, companied by slight energy leakage to out of the signal band, which makes the shape of the spectrum be maintained to a large extent. These properties make the designed SEFDM symbol applicable for BOTDA systems. The generation procedure of the SEFDM signal is summarized as shown in Fig.5.3.

First, a N_{ZC}-bit ZC sequence is generated. Then a N_{pZC}-bit partial ZC sequence is clipped from the ZC sequence. In order to realize a real-value output of the SEFDM symbol, Hermitian symmetry is applied to the partial ZC sequence. Then an S-point data sequence is generated, after which IDFT is used to generate the time-domain discrete OFDM symbol. The centralized OFDM symbol is then clipped to be an SEFDM symbol. A Y-bit zero sequence is padded before each SEFDM symbol serving as the guard interval. After P/S conversion, the generated SEFDM signal is digital to analog converted to serve as the probe signal. During the generation of the SEFDM signal, the partial percentage should be tuned according to the length of the SEFDM symbol to ensure a good centralization of the OFDM signal.

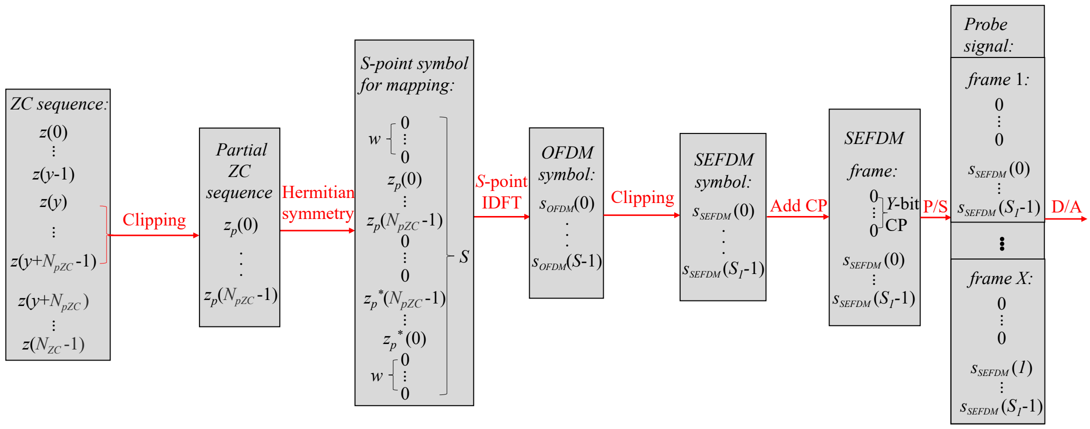

Figure 5.3 The generation procedure of the SEFDM signal.

5.2 Sensing principle

5.2.1 Channel estimation based Brillouin spectrum demodulation

In optical fiber communication systems, channel estimation using pilot signals that are already known by both the transmitter and receiver is normally applied to compensate for the channel impairments. At the receiver side, the electrical field of the received signal can be written as [61]

$$E_{re}(t) = h(t) \otimes E_{tr}(t) \tag{5.6}$$

where $E_{tr}(t)$ is the electrical field of the signal at the transmitter side; $h(t)$ is the impulse response of the fiber channel and represents the convolution operator. In the frequency domain, Eq.(5.6) becomes

(5.7)

is the channel response of the FUT. Obviously, can be calculated by

$$H(f) = E_{re}(f) / E_{tr}(f) \tag{5.8}$$

The SEFDM-BOTDA system can be regarded as a special optical fiber communication system, where the transmitted data is the already-known SEFDM probe signal. After transmitting through the FUT, the probe wave interacts with the counter-propagated pump light through SBS process, leading to the amplification of some frequency components of the SEFDM signal, considering the Brillouin gain scheme. The frequency-domain gain profile is related to the BGS of the fiber as discussed in section 2.2.3-A. Therefore, in the SEFDM-BOTDA system, the sensing fiber can be seen as a special channel, which contains the SBS information. The channel response can be written as

$$H_s(f) = H_0(f) H_{SBS}(f) \tag{5.9}$$

where $H_0(f)$ represents the inherent channel distortion of the FUT, which can be estimated using the received symbols that are not affected by the SBS process; $H_{SBS}(f)$ represents the channel response induced by the SBS process, which can be used for the BFS measurement. Therefore, through channel estimation, the Brillouin spectrum of the FUT can be retrieved.

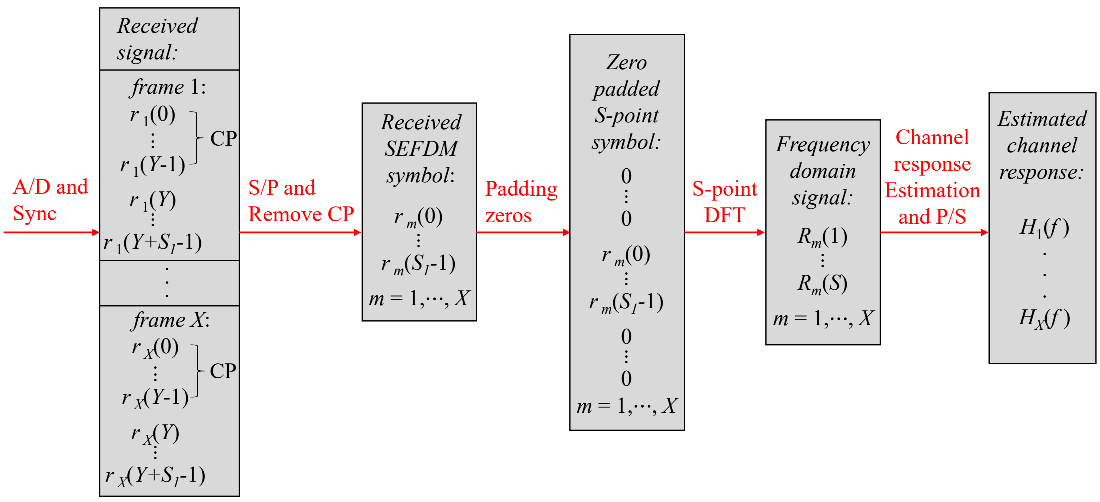

Figure 5.4 The procedure of estimating the channel response.

The procedure of estimating the channel response is shown in Fig. 5.4. After analog to digital convention and synchronization, the digitized time-domain SEFDM signal is first serial to parallel (S/P) converted and the added CP is removed. Then each SEFDM symbol is padded with $S-S_1$ zeros. FFT is applied to the resultant S-point time-domain SEFDM symbol to retrieve the frequency-domain signal, after which the channel response of the FUT can be estimated through Eq.(5.8). By demodulating the channel response of FUT with and without the SBS process, the complex Brillouin spectrum (CBS) can be finally retrieved through Eq. (5.9). After combining the measurement results of all the SEFDM frames, the distributed information of CBS along the FUT can be obtained finally.

5.2.2 Influence of the ISI

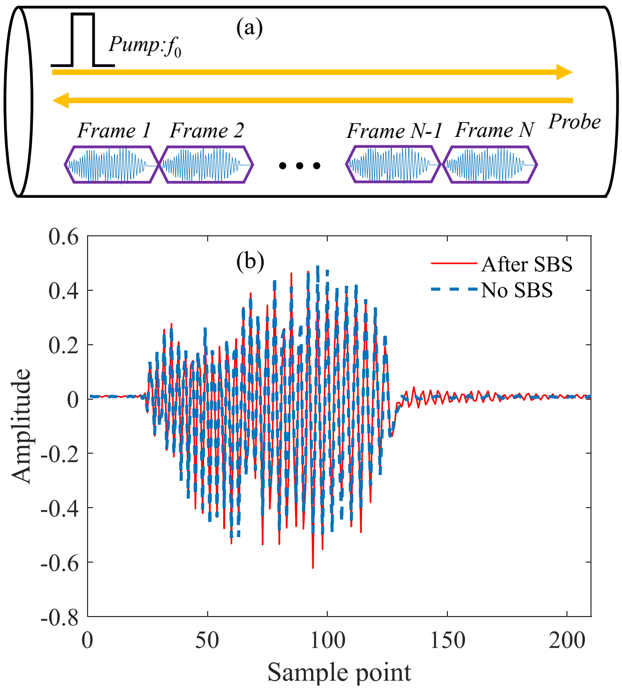

Figure 5.5 (a) The schematic diagram of the SBS process in SEFDM BOTDA, and (b) the time-domain SEFDM symbol before and after the SBS interaction.

Figure 5.5 (a) schematically shows the interaction process between the SEFDM probe signal and the pump pulse. The pump pulse first interacts with the symbol in *Frame 1* through the SBS process. Due to the SBS interaction and other factors like the channel imperfection and dispersion, the SEFDM symbol in *Frame 1* is broadened and spills over to the adjacent symbol. Figure 5.5 (b) shows the time-domain SEFDM symbols before and after the SBS interaction. It is obvious that the SEFDM symbol after the SBS interaction is broadened. Therefore, when the pump pulse encounters *Frame 2*, the SBS process actually occurs between the pump pulse and the interfered symbol, leading to the symbol in *Frame 2* spilling over to the adjacent symbol. The phenomenon of the symbol spreading and merging with the adjacent symbol is called the ISI. The SBS interaction between the pump pulse and the interfered symbol as well as the ISI between two succeeding symbols continuously occur with the propagation of the pump pulse. Due to the ISI, the retrieved BGS is distorted. In optical fiber communication systems, a long enough CP is used to provide a guard interval to eliminate the ISI. However, since the proposed SEFDM-BOTDA turns to be a quasi-distributed system with the extension of the length of CP, the length of CP has to be as short as possible to ensure the distributed measurement. Therefore, it is important to analyze the influence of ISI by adjusting the length of CP.

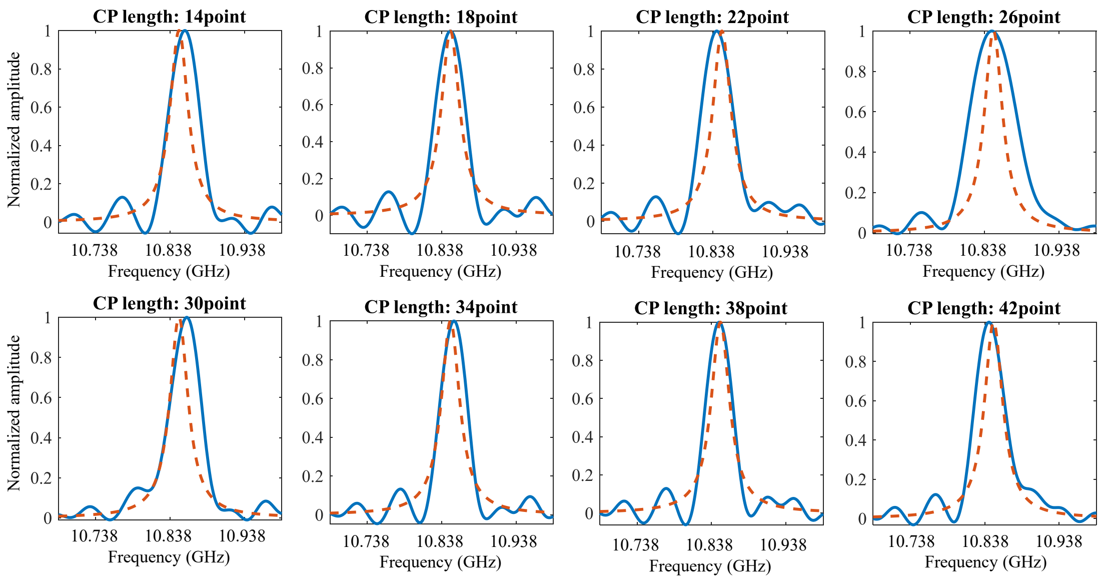

Figure 5.6 Simulation results of the BGS when the fiber is not stretched and heated. Blue solid line: the simulated BGS affected by ISI. Red dashed line: the ideal BGS with Lorentz line shape.

First, the case that the sensing fiber does not suffer from any strain and temperature variation is considered. Figure 5.6 shows the numerical results of the retrieved BGS affected by ISI when different lengths of CP are applied. The SEFDM symbol as shown in Fig. 5.2 (b) is used. The Lorentz line width is set to 30 MHz and the BFS is set to 10.84 GHz. Results show that due to the influence of ISI, the simulated BGS is asymmetric. For example, the spectrum right deviates when the length of CP is 14 points. However, when the length of CP is increased to 18 points, the spectrum is symmetric. With the increase of the CP length, the spectrum first left deviates, then becomes symmetric and then right deviates. That means as long as the length of CP is not long enough to eliminate the ISI completely, the BGS will right or left deviate for most cases. However, with some special CP lengths, i.e. 18 points, the BGS is symmetric and the BFS can be correctly obtained through searching the peak of the spectrum. Besides, due to the influence of ISI, the retrieved BGS is broadened to be no more a Lorentz line shape.

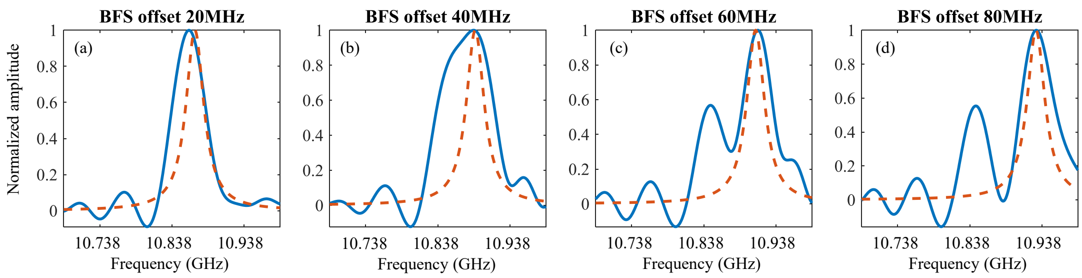

Figure 5.7 Simulation results of the BGS when the fiber is not stretched and heated. Blue solid line: the simulated BGS affected by ISI. Red dashed line: the ideal BGS with Lorentz line shape.

Next, let us consider the second case that a section of the fiber, with the length that equals the spatial resolution, is stretched or heated. The simulation result is shown in Fig. 5.7. The CP length is set to 18 points. Due to the influence of the ISI, the BFS offset is no more linearly related to the change of the strain or temperature the fiber suffered. If the BFS offset is small, i.e. 20MHz, the simulation result indicates that the measured BFS is smaller than the real value. When the BFS offset increases to 40 MHz, the measured BFS just equals the real value. However, when the BFS offset increases to 60 MHz, the measured BFS is larger than the real value. But when the BFS offset is large enough, i.e. larger than 80 MHz, the frequency component from the neighboring symbol, which is the secondary peak shown in Fig. 5.7(d), no more influences the measured BFS. In that case, the BFS offset is linearly related to the fiber strain or temperature. It should be noted that when the length of the stretched or heated fiber is much longer than the spatial resolution of the SEFDM-BOTDA system, the analysis of the beginning (or end) symbol that is influenced by the strain (or temperature) is like the second case as discussed above, in which the symmetry of BGS is greatly distorted because of the interference of the neighboring symbol. However, the analysis of the residual symbols that are influenced by the strain (or temperature) is like the first case as discussed above, in which the BGS is symmetric. Therefore, such a case is no more discussed in this work. The above analysis tells us that an optimal CP length has to be determined to ensure the linearity between the measurand and BFS, as well as a well-distributed measurement in real applications.

5.2.3 Complementary Golay coding technique

In BOTDA systems, due to the optical fiber nonlinear effects, including self-phase modulation (SPM), SRS and modulation instability, etc., when the peak power of the pump light is too high, it will cause the nonlinear energy transfer between the pump light and probe light, thus deteriorating the system's performance. The use of the rectangular pump pulse helps to minimize SPM. Therefore, SRS and modulation instability are the main factors that limit the sensing performance of BOTDAs. Optical pulse coding technique has been proposed and widely investigated in DOFSs to improve the SNR of the measurands. By sending a series of coded pulse sequences into the sensing fiber, which is equivalent to increasing the power of the pump light injected into the fiber, the SBS interaction is enhanced, resulting in the improvement of the SNR. There are two general coding schemes. One is the correlation coding and the other is the linear combination coding. In this work, the Golay complementary code, which belongs to the correlation coding, is used. A set of Golay complementary code contains two bipolar sequences, which obeys the following relationship [138]

(5.10)

(5.11)

where * represents the correlation operation and I represent the coding bits. Golay complementary code can be generated using the iterative algorithm as the follow

$$\begin{Bmatrix} A \\ B \end{Bmatrix} \rightarrow \begin{Bmatrix} A \mid B \\ A \mid \overline{B} \end{Bmatrix} \tag{5.12}$$

$$\text{i.e. } \begin{Bmatrix} 1 \\ 1 \end{Bmatrix} \rightarrow \begin{Bmatrix} 1 & 1 \\ 1 & \text{-}1 \end{Bmatrix} \rightarrow \begin{Bmatrix} 1 & 1 & 1 & \text{-}1 \\ 1 & 1 & \text{-}1 & 1 \end{Bmatrix} \tag{5.13}$$

where $\overline{B}$ means the negation operation of B. But the amplitude of light is positive, therefore two pairs of unipolar sequences (C_1,C_2) and (D_1,D_2) are needed for simulating the bipolar coding, which can be written as

$$C_1 = \begin{cases} 1, & A_k = 1 \\ 0, & A_k = -1 \end{cases} \qquad C_2 = \begin{cases} 0, & A_k = 1 \\ 1, & A_k = -1 \end{cases} \qquad A_k = C_1 - C_2 \tag{5.14}$$

$$D_1 = \begin{cases} 1, & B_k = 1 \\ 0, & B_k = -1 \end{cases} \qquad D_2 = \begin{cases} 0, & B_k = 1 \\ 1, & B_k = -1 \end{cases} \qquad B_k = D_1 - D_2 \tag{5.15}$$

After launching the coded pulse sequences into the sensing fiber, four coded channel responses (R_{C1}, R_{C2}, R_{D1}, R_{D2}) can be obtained. The coded channel response is the convolution of the coding sequence and the single pulse channel response. Therefore, the single pulse channel response is demodulated through the correlation operation as

$$h_{coding} = (R_{C1} - R_{C2}) * (C_1 - C_2) + (R_{D1} - R_{D2}) * (D_1 - D_2) = 2Ih_o \tag{5.16}$$

where h_o is the channel response obtained without pulse coding. Eq(5.16) tells us that the channel response has been increased by $2I$ times. However, since the noise also increases due to two minus calculations, two correlation calculations and one addition calculation, the SNR is increased by a factor of   . Besides, as four cycles of data transmission are needed to complete one-time measurement, the actual enhancement of the SNR is   , comparing the measurement with four times averaging. Therefore, optical pulse coding provides a time-saving way to largely improve the SNR.

5.3 Experiment setup

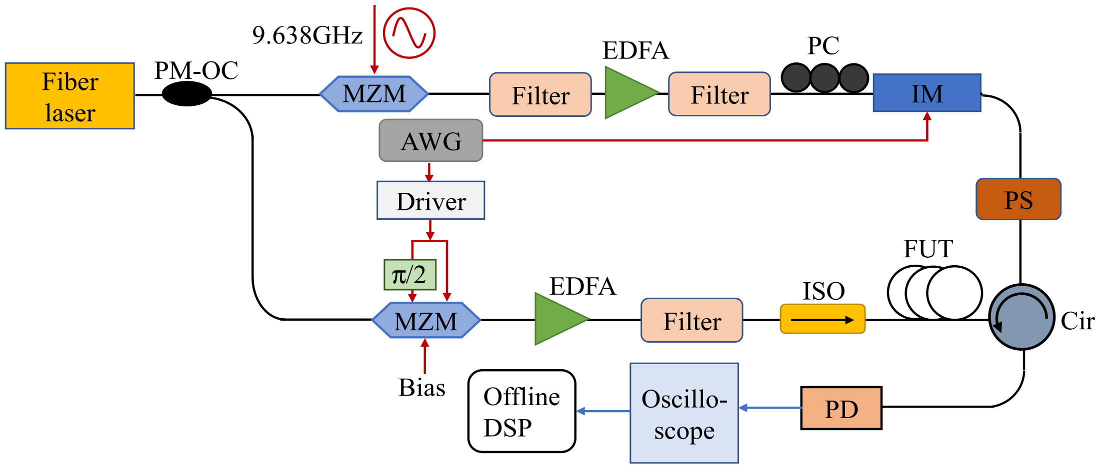

Figure 5.8 The experimental setup of the proposed SEFDM-BOTDA. PM-OC: polarization maintaining optical coupler; MZM: Mach Zehnder modulator; EFDA: erbium doped fiber amplifier; PC: polarization controller; IM: intensity modulator; PS: polarization scrambler; ISO: isolator Cir: circulator; PD: photodetector.

The experiment setup of the proposed SEFDM-BOTDA is shown in Fig.5.8. A 50/50 polarization maintaining coupler is used to divide the output of a fiber laser with center wavelength of 1550.12 nm (NKT X15 with 100 Hz linewidth) into two branches as the probe and pump respectively. The lower branch is fed into a dual-drive Mach Zehnder modulator (MZM), where the single sideband modulation scheme is applied for the SEFDM signal generation. The MZM is biased at the quadrature point. An AWG (Keysight M8190) is used to generate the real-valued RF SEFDM signal at a sampling rate of 4GSa/s. The RF SEFDM signal from the AWG was amplified using an electrical driver and fed into a 90° hybrid which generated a Hilbert signal pair. The two outputs of the electrical hybrids were fed into the two RF ports of the dual-drive MZM biased at the quadrature point. The designed frequency range of the SEFDM signal was set from 950 MHz to 1.45 GHz to align with the bandwidth of the electrical hybrid. The subcarrier spacing is set as 1 MHz to ensure the recovery accuracy of the BGS. After the dual-drive MZM, an EDFA followed by a 0.8 nm BPF is used to amplify the probe signal to an average power of -3 dBm. The probe signal is finally injected into the 10 km FUT through an isolator. To generate the pump pulses, the upper branch is first fed into an

MZM driven by a 9.638 GHz microwave signal to generate a carrier suppressed dual sideband signal. The USB is filtered out by a 0.2 nm narrow bandwidth filter and then is amplified by an EDFA followed by a 0.8 nm BPF before launched into an intensity modulator to generate pump pulses. To boost the Brillouin gain and improve the SNR of the sensing system, 128-bit complementary Golay codes are used to generate the pulse sequences. The peak power of the pulse is around 15 dBm and the pulse width is 15 ns with a cycle duty of 11%. A polarization scrambler is used to alleviate the polarization-dependent fluctuation of the SBS interaction efficiency. Pump pulses are injected into the FUT through an optical circulator. At the receiver, a PD (Newport 1544) is used for the signal detection and an oscilloscope (Keysight MSOS404A Infiniium) working at 4 GSa/s sampling rate is used to realize the ADC.

5.4 Results and discussions

5.4.1 Experimental demonstration of the ISI

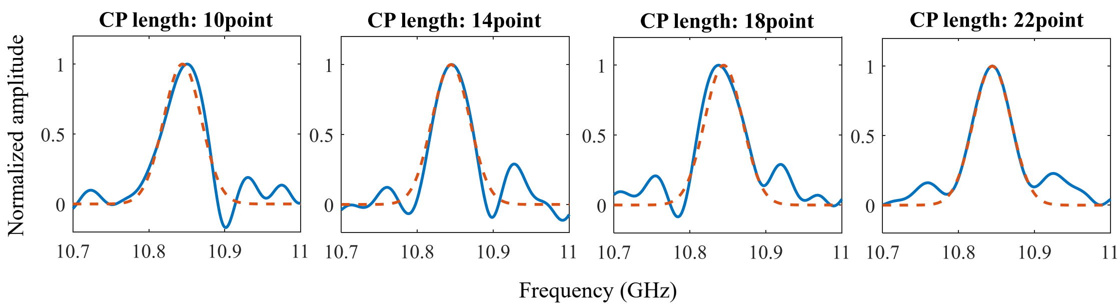

Figure 5.9 Experimental results of the ISI with different CP lengths in case the sensing fiber is neither stretched nor heated. (blue solid line: the retrieve BGS; red dashed line: Gaussian fitting curve)

To experimentally demonstrate the influence of ISI in SEFDM-BOTDA systems, the 101-point SEFDM symbol as shown in Fig.5.2 (b) is used for the study. The received signals are first averaged 20 times to enhance the SNR. After that, the channel estimation algorithm followed by the complementary pulse decoding algorithm is applied to retrieve the BGS of each SEFDM frame. For the first case, the fiber is neither stretched nor heated. Figure 5.9 shows the result when different lengths of CP are applied. One can see that the retrieved BGS right deviates when CP length is only 10 points. With the increase of the CP length, the retrieved BGS becomes symmetric and then left deviates. The BGS becomes symmetric again when the CP length is 22 points.

In the second case, a section of fiber with a length comparable to the spatial resolution (about 3 m in this case) is stretched. Since the retrieved BGS is symmetric when the CP length is 14 points or 22 points, these two CP lengths are selected for the investigation. The strain applied to the fiber is gradually strengthened. Experimental results are shown in Fig. 5.10. It can be seen that when the strain is applied to the fiber, the BFS shifts. But when the CP length is 14 points, the ISI is so strong that two peaks appear in the retrieved BGS corresponding to the stretched fiber. As a result, the BFS cannot be correctly estimated. When the CP increases to 22 points, the influence of ISI is very small. Therefore, the retrieved BGS corresponding to the stretched fiber can keep symmetric. In that case, the linearity between the BFS and the fiber strain can be maintained. It can be seen from both Fig. 5.9 and Fig. 5.10 as well that due to the influence of the ISI the retrieved BGS is broadened. It should be noted that when the CP length is long enough, i.e. 200 points, the influence of ISI can be completely eliminated, in that case, the retrieved BGS will become a Lorentz line shape.

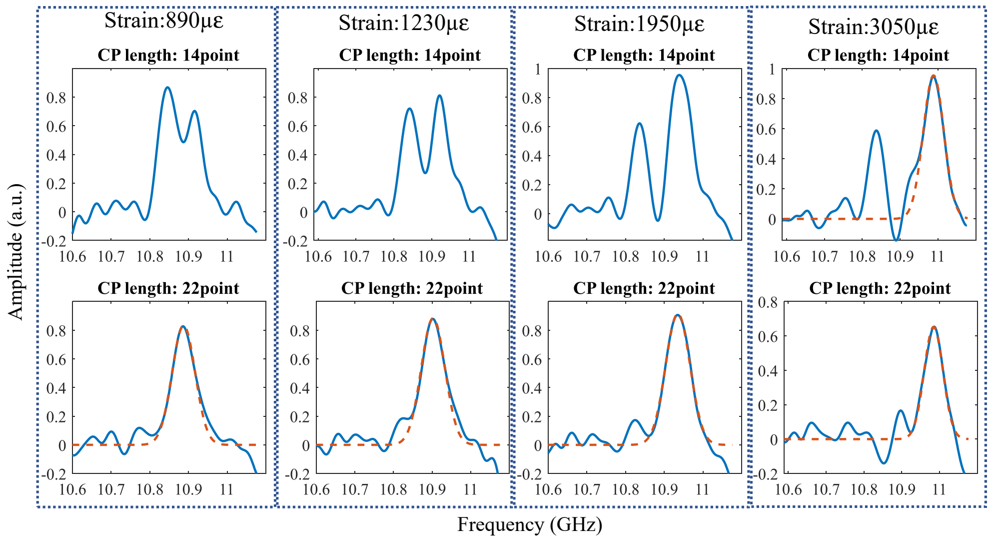

Figure 5.10 Experimental results of the ISI when 14-points and 22-points lengths of CP are used and a 3 m sensing fiber is stretched. (blue solid line: the retrieve BGS; red dashed line: Gaussian fitting curve)

5.4.2 Investigation of the sensing performance

To reduce the influence of ISI, the 101-point SEFDM symbol with 22-point CP is used as the probe signal. Fig. 5.11 (a) shows the reconstructed Brillouin spectrogram. Obviously, the spatial resolution is limited by the SEFDM frame duration, which is 3.1 m. It should be noted that since the subcarrier spacing used in this work is 1 MHz, the corrsponding spatial resolution would be 102.4 m in an OFDM-BOTDA. To enhance the estimation accuracy of the BFS, the Gaussian curve fitting is applied to the BGS for determining the peak value. Static measurement was conducted first. The measured relationship between BFS and fiber strain via linear fitting is shown in Fig. 5.11 (b). The calculated strain coefficient for the FUT is 0.046 MHz/με and the coefficient of determination R^2 is 0.9987.

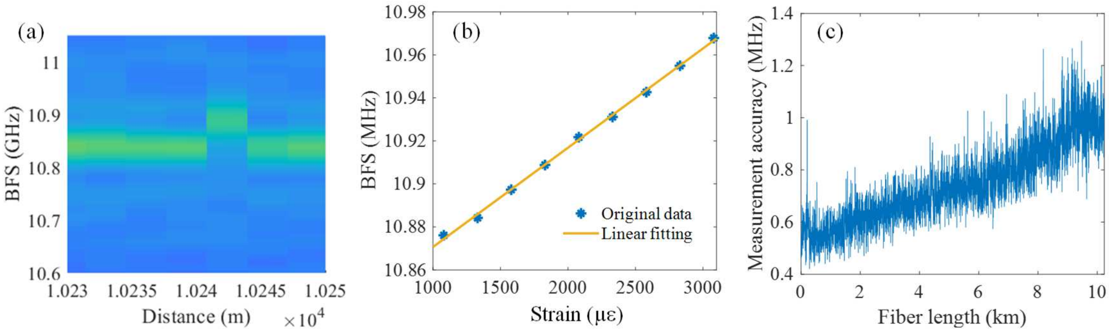

Figure 5.11(a) The reconstructed Brillouin spectrogram, and (b) Result of the strain measurement.

To test the measurement accuracy, 100 data sets were consecutively acquired. The measurement accuracy along the fiber length was obtained by calculating the standard deviations of the 100 measurement data for all the SEFDM frames. Results are shown in Fig. 5.11 (c). One can see that the measurement accuracy fluctuates along the fiber length. The reason is that the power of the SEFDM signal is nonuniformly distributed, which will cause the low Brillouin gain at some positions and consequently a low measurement accuracy. The nonuniform distribution of the SEFDM signal can be evaluated using a parameter called peak to average power ratio (PAPR), which is defined as

$$PAPR = 10\log_{10}\left(\frac{\max\left[\left|s_{SEFDM}(t)\right|^2\right]}{E\left[\left|s_{SEFDM}(t)\right|^2\right]}\right) \tag{5.16}$$

where $s_{SEFDM}(t)$ is the baseband SEFDM signal. High PAPR means the large distribution variations of the SEFDM signal power, which influences the estimation accuracy of the BFS. As shown in Fig.5.11 (c), the lowest measurement accuracy obtained in this experiment is 1.294 MHz.

Table 5.1 The details of three different SEFDM signals

Frame duration	20.25 ns	23.75 ns	30.75 ns
CP length	16 points	14 points	22 points
Symbol length	65 points	81 points	101
Spatial resolution	2 m	2.4 m	3.1 m

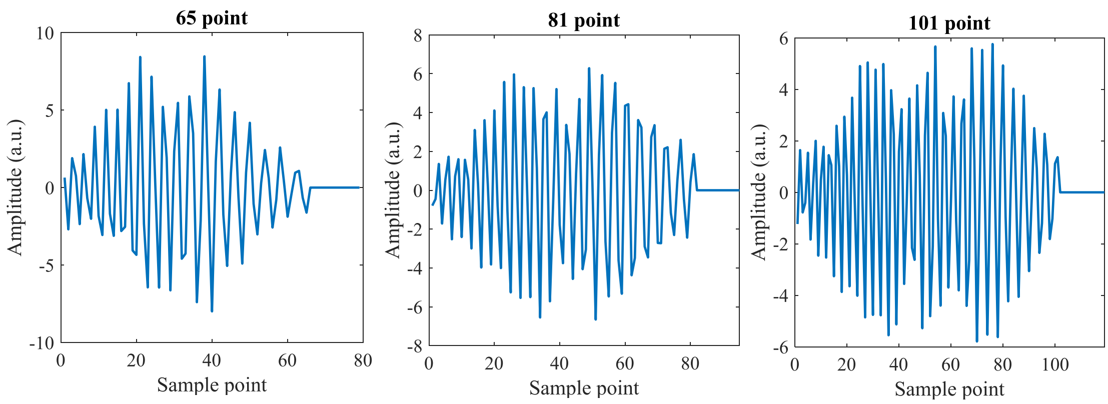

Figure 5.12 Time-domain waves of three SEFDM signals with different symbol lengths.

To further narrow the spatial resolution, another two SEFDM symbols with shorter symbol lengths are designed to serve as the probe signal. Figure 5.12 shows the time-domain signal waves of three SEFDM symbols. Table.1 lists the details of the three SEFDM signals used in our experiment. The basic criteria of determining the CP lengths for the 65-point and 81-point cases is to ensure a good symmetry of the retrieved BGS. To compare the influence of the symbol length, all the other operational parameters, i.e., the average power of the SEFDM symbol, the peak power of the pump pulse and the coding sequence are kept the same during the experiment.

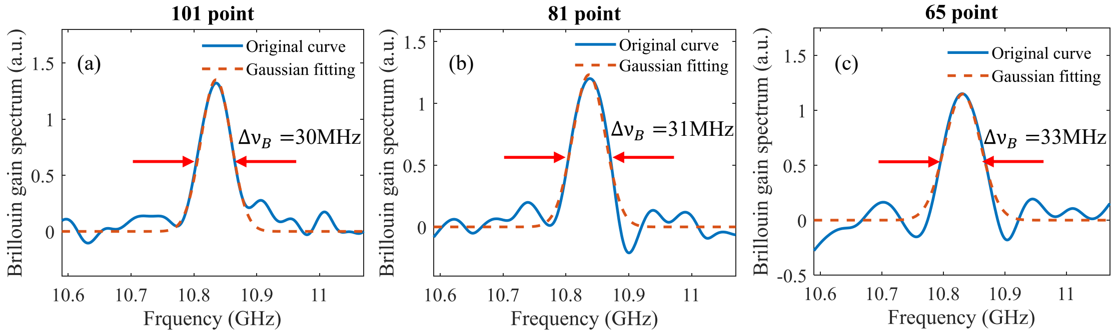

Figure 5.13 The retrieved BGS and the corresponding fitting curves when (a) 101 point symbol, (b) 81 point symbol and (c) 65 point symbol are used.

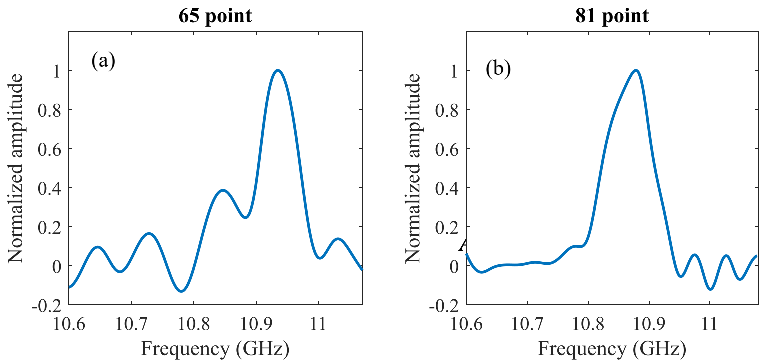

Figure 5.14 The retrieved BGS when a 3 m sensing fiber is stretched (a) for the 65-point case and (b) for the 81-point case.

Fig. 5.13 shows the retrieved BGS and the corresponding fitting curves of these three cases. It can be seen that with the decrease of the symbol length, the linewidth of the retrieved BGS increases, which indicates that the ISI becomes severer. Although ISI can be alleviated using a longer CP, the increased length of CP leads to the degradation of the spatial resolution. Therefore, the CP length of 16 points was chosen for the 65-point SEFDM signal and the CP for the 81-point SEFDM signal is 14 points. Due to the more serious ISI, the phenomenon of the secondary peak and BGS distortion when the sensing fiber is stretched becomes more obvious for the 65-point and 81-point cases, as shown in Fig.5.14. Therefore, with the decrease of the spatial resolution, the difficulty of ensuring the linear relationship between the fiber strain (or temperature) and the measured BFS greatly increases.

As the time-consuming frequency sweeping procedure is eliminated, fast measurement can be realized in the proposed sensing scheme. To investigate the dynamic sensing performance, a periodical vibration signal produced by an electric-motor-driven eccentric wheel was applied to stretch a 3 m fiber at the end of the FUT. Since 20 times averaging and complementary pulse coding was used, the event sampling rate of this system is 125 Sa/s. Fig. 5.15 shows the BFS variations of the stretched fiber when a 3-V voltage is applied to the driving motor. The vibration signal can be well retrieved and the measured variation frequency is 26 Hz.

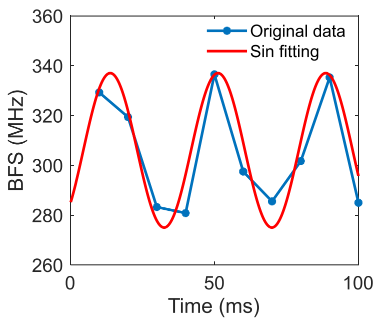

Figure 5.15 The retrieved vibration signal and the corresponding fitting curve.

In this sensing scheme, in order to make the sensing system as simple as possible, polarization scrambling with averaging is used to reduce the polarization-induced SBS power fluctuation. It should be noted that the polarization diversity scheme [54] can be applied to reduce the number of averages such that the event sampling rate of the BOTDA system can be largely enhanced even though the system complexity increases accordingly. It is also worth noting that the influence of the PAPR can be weakened by using a larger number of averages and simultaneously a large number of averages can enhance the system's SNR. As a result, the measurement accuracy can be improved. But the increase of averages means the decrease of the event sampling rate. Therefore, to ensure the frequency response of the system, only 20 times of averaging is applied in this work.

Due to ISI, the length of CP influences the measurement accuracy greatly. Since the

Brillouin gain coefficient, Brillouin bandwidth and the intrinsic channel response of different fibers are different, the ISI is different for different cases. Therefore, in real applications, the CP length has to be determined specifically by testing the ISI with different CP lengths to ensure good measurement accuracy.

To conclude, the proposed SEFDM-BOTDA has the following advantages. The spatial resolution is greatly improved while the good measurement accuracy is maintained compared with the OFDM technique. Besides, a large dynamic range can be easily realized using more subcarriers without compromising the spatial resolution or the measurement accuracy compared with the OCC technique. The elimination of the use of high-speed equipment makes the proposed sensing system much more cost-effective.

5.5 Conclusions

A novel fast BOTDA based on the SEFDM technique has been proposed and experimentally demonstrated. A partial ZC-sequence based SEFDM symbol has been designed for the BOTDA. Complementary pulse coding has been used to further enhance the SNR. Due to the dramatic reduction of the symbol duration, the spatial resolution can be significantly improved. We have analyzed the BGS broadening and distortion due to ISI. Through carefully adjusting the length of the CP, the influence of the ISI can be alleviated. Finally, a spatial resolution of 3.1 m with a measurement accuracy of 1.294 MHz has been achieved when 101-point SEFDM symbol with 22-point CP was used. A dynamic vibration measurement with a vibration frequency of 26 Hz has also been successfully demonstrated. The proposed SEFDM technique provides great application potential of BOTDAs in both static and dynamic distributed fiber sensing areas.

Chapter 6

Conclusions and Future works

In this Chapter, conclusions of the thesis are given and prospected works for dynamic DOFS are discussed.

Conclusions

Dynamic DOFSs have attracted great research attention in the past decades due to their broad application prospects in the field of safety monitoring of large infrastructures, perimeter security monitoring, seismic detection, etc. However, it is very difficult to realize ultralong range sensing using the reported dynamic distributed sensing technique due to the weak signal intensity of the backscattering light as well as the influence of the RBN in distributed optical fiber interferometers. Besides, as for the SBS-based dynamic DOFSs, the spatial resolution is a problem when OFDM is used to eliminate the time-consuming sweeping process. Inspired by the similarities between the optical fiber communication systems and DOFSs, the dynamic DOFSs assisted by the optical communication techniques are proposed in this thesis to further improve the sensing performance.

A novel ultralong haul distributed vibration sensor using the unidirectional forward transmitted light and coherent detection is studied. It has been demonstrated that through using two sensing fibers placed close to each other and an FS-ODL structure at the far end of these two sensing fibers, the external vibration can be localized by estimating the time delay between two constructed differential phase signals. Due to the differential effect and the inversely proportional relationship between the phase noise and frequency, the location accuracy decreases with the decrease of the vibration frequency. Experimental results show that a spatial resolution of 125m is reached over a 615 km sensing range when the vibration frequency is higher than 1 kHz. The sensing distance is largely extended because the unidirectional forward transmission solves the Rayleigh backscattering-induced noise problem, and the ability to use EDFAs in forward transmission compensates the signal loss, which enables a good SNR at the receiver. The ultrabroad frequency response from infrasound to ultrasound is achieved as well thanks to the use of CW light.

The multi-point sensing problem is addressed through an improved unidirectional forward transmission based sensing scheme. The sensing structure is further simplified as the FS-ODL is eliminated. The vibration is localized by analyzing the null points displayed in the spectrum of the retrieved phase signals. When the single-point vibration occurs, the vibration location can be determined both by the K^{th} null frequency point determination method and double FFT method. However, when multi-point vibrations occur, only the double FFT method can be used for determining the vibration location. Compared with the time delay estimation algorithm, the double FFT method is a more convenient and efficient way to detect multi-point vibrations because different vibration locations can be easily distinguished through searching the peaks shown in the second time FFT spectrum. Results show that a location error of less than ± 100 m is achieved for the single-point vibration while the location error of multi-point vibrations is less than 200 m.

Aiming to remove the limitation of spatial resolution in OFDM-BOTDAs, a novel SEFDM BOTDA is proposed and studied. SEFDM is a promising candidate to overcome the spatial resolution constraint in OFDM-BOTDAs because the frequency tones in SEFDM systems do not obey the orthogonal condition. The partial ZC sequence based SEFDM symbol is designed for the BOTDA. The BGS is reconstructed using the channel estimation algorithm. Complementary Golay coding technique is also used to improve the SNR. Theoretical and experimental investigation shows that due to the limited length of CP, ISI is a significant factor that influences the sensing performance of the proposed scheme. Good measurement accuracy can be reached only when an optimized CP length is used. It is demonstrated that the measurement accuracy of 1.294 MHz is obtained when the spatial resolution is set to 3.1 m, corresponding to the use of a 101-point symbol with 22-point CP. Dynamic measurement of a 26 Hz vibration signal is verified as well. The tradeoff between spatial resolution and measurement accuracy is largely alleviated in SEFDM-BOTDAs, but still exists due to the influence of ISI. Since the length of SEFDM symbol can be tuned by adjusting the partial percentage of the partial ZC sequence while the frequency spacing can be maintained, the proposed scheme provides higher flexibility for BOTDAs to be used in a wider application area.

6.2 Future works

The research work presented in the thesis focuses on improving the sensing performance of dynamic DOFSs with the help of optical communication techniques. As an extension of the research works described in previous chapters, additional techniques can be investigated to further improve the performance and explore new applications of dynamic DOFSs in the future work. Suggestions are illustrated as follows.

The research work described in chapter 4 tries to solve the problem of multi-point detection in unidirectional forward transmission dynamic DOFSs. The double FFT method enables multi-point detection, however, the null-frequency induced problems, like the inability to detect some frequency components, the requirement for wideband vibration signals and the dead zone of localization, remain to be solved. The use of the FS-ODL structure can largely reduce the number of null points in the spectrum, which makes the detection of vibrations more reliable. But the weakness is the multi-point detection. Referring to the scheme of φ-OTDR, in which multi-point detection can be easily realized, a modified structure can be used to significantly strengthen the multi-point sensing ability of unidirectional forward transmission based DOFSs. The loopback configuration proposed in chapter 3, which is formed by two closely placed sensing fibers and an FS-ODL structure, servers as a basic unit. Several basic units can be cascaded to form a sensing chain to ensure multi-point vibration detection. At the transmitter, a chirped pulse chain instead of a CW carrier is transmitted. A power splitter can be used at the far end of each basic unit, where a portion of the power is fed into the succeeding basic unit and the other portion is coupled into the FS-ODL of the former unit to form a return path. The number of frequency bins used at the transmitter is equal to the number of basic units. The frequency tuning step is fixed and at the same time, the sensing distance of each basic unit and the duration of each pulsed light are related. This sensing scheme can be regarded as a combination of optical frequency domain reflectometry and the unidirectional forward transmission system. If multiple vibrations occur simultaneously at different units, the vibration location can be easily distinguished. But if the multiple vibrations occur at the same unit, which is the case in chapter 3, it is difficult to distinguish these vibrations. It should be noted that the occurrence possibility of multiple vibrations is much lower in a short sensing range. Therefore, the suggested structure solves the multi-point detection problem to a large extend.

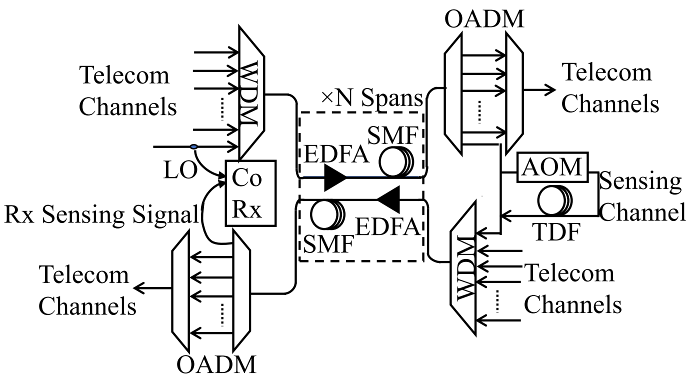

Figure 6.1 The configuration of the integrated optical sensing and communication system.

More research efforts can be made to investigate the possible integration of distributed sensing and optical communications systems. The work described above that uses unidirectional forward transmission light to carry out long-haul distributed vibration sensing is a good attempt to explore the feasibility of extracting sensing information directly from an operating optical communication system. Since the sensing light is unidirectionally transmitted in the optical fiber, which shares similarities with the optical communication systems, it is easy to integrate the unidirectional forward transmission-based sensing system with the optical communication system. Figure 6.1 gives a preliminary configuration of the integration system of optical fiber sensing and optical fiber communication. The sensing signal and communication signals are simultaneously transmitted in the same fiber link. By using the wavelength division multiplexing and demultiplexing technique, the interference between sensing and communication signals can be negligible due to the narrow bandwidth of the CW sensing light. As a result, high sensing and communication performance can be simultaneously realized in a single fiber system. On the other hand, various advanced optical communication DSP algorithms have been developed, it will also be interesting to use the mature DSP algorithms to enhance the performance of dynamic DOFSs.

Spatial division multiplexing using multicore and few-mode fiber has been studied extensively for optical communication, which also has a very promising potential for dynamic DOFSs. Here common parameter variation can easily be removed and detection of differential parameter variation allows many innovative sensing systems to be realized. Other efforts may include combining different detection techniques to enhance system performance. For example, φ-OTDR is capable of detecting the sub-Hz vibration signals as well as multi-point vibrations with a high spatial resolution while the proposed unidirectional forward transmission technique can solve the sensing range, dynamic range and high-frequency vibration detection problem. Therefore, it is a good try to combine the forward transmission-based sensing scheme with the φ-OTDR to realize the distributed vibration measurements with a wide-frequency range and large amplitude in the future.

In chapter 5, we have demonstrated that the bottleneck for OFDM-BOTDA to achieve a high spatial resolution can be mitigated using the SEFDM technique. However, results show that severe ISI distorts the retrieved BGS, leading to the nonlinear relationship between the BFS and the change of the environmental parameter. The influence of ISI is inevitable if the spatial resolution needs to be further improved. In that case, the nonlinear relationship has to be pre-measured to ensure good measurement accuracy. Therefore, the nonlinear relationship as well as the degree of the ISI distortion should be investigated deeply in the future. In addition, a long enough CP can be used to eliminate the influence of ISI, but the use of zero-suffix makes the system be a quasi-distributed sensing system. The region of the zero-suffix can be filled by other SEFDM symbols with different carrier frequencies. In the other words, frequency division multiplexing can be used to solve the problem of ISI as well as to ensure the distributed measurement with a much higher spatial resolution.

Publications Arising from the Thesis

Journal paper

[1] **Y. Yan**, F. N. Khan, B. Zhou, A. P. T. Lau, C. Lu and C. Guo, "Forward Transmission Based Ultra-Long Distributed Vibration Sensing With Wide Frequency Response," in *Journal of Lightwave Technology*, vol. 39, no. 7, pp. 2241-2249, 2021.

[2] **Y. Yan**, H. Zheng, Z. Zhao, C. Guo, X. Wu, J. Hu, A. P. T. Lau and C. Lu, "Distributed optical fiber sensing assisted by optical communication techniques," in *Journal of Lightwave Technology,* vol 39, no. 12, pp. 3654-3670, 2021.

[3] **Y. Yan**, H. Zheng, C. Guo A. P. T. Lau and C. Lu, “Unidirectional Ultra-Long Distributed Optical Fiber Sensor”, in *Photonics Journal,* vol. 13, no. 4, pp. 1-7, 2021.

[4] **Y. Yan**, H. Zheng, C. Lu and C. Guo, “Dynamic BOTDA based on spectrally efficient frequency-division multiplexing.” (submitted)

[5] H. Zheng, **Y. Yan**, Y. Wang, X. Shen, and C. Lu, “Deep learning enhanced long-range fast BOTDA for vibration measurement”, in *Journal of Lightwave Technology* (accepted).

[6] H. Zheng, **Y. Yan**, Z. Zhao, T. Zhu, J. Zhang, N. Guo and C. Lu, “Accelerated fast BOTDA assisted by compressed sensing and image denoising”, in *IEEE Sensors*, (accepted)

[7] K. Zhu, B. Zhou, H. Wu, C. Shang, L.Lu, M. Adeel, **Y. Yan**, Z. Zhao, H.-Y. Tam and C. Lu, “Multipath distributed acoustic sensing system based on phase-sensitive optical time-domain reflectometry with frequency division multiplexing technique,” *Optics and Lasers in Engineering*, vol. 142, 2021.

[8] Z. Zhao, H. Wu, J. Hu, K. Zhu, Y. Dang, **Y. Yan**, M. Tang and C. Lu, "Interference

fading suppression in φ-OTDR using space-division multiplexed probes," *Opt. Express*, vol. 29, 2021.

Conference paper

[1] W. Wang, Y. Liu, X. Du, **Y. Yan**, C. Yu and X. Chen, "A Novel Demodulation Method of Fiber Bragg Grating Sensor Array Based on Wavelength-to-Time Mapping and Multiloop Optoelectronic Oscillator," *2020 Optical Fiber Communications Conference and Exhibition (OFC)*, 2020.

Bibliography

[1] S. Shimada, "Systems engineering for long-haul optical-fiber transmission", *Proc. IEEE*, vol. 68, no. 10, pp. 1304-1309, 1980.

[2] D. M. Fye, "Low-current 1.3-μm edge-emitting LED for single-mode fiber subscriber loop applications", *J. Lightwave Technol.*, vol. 4, no. 10, pp. 1546-1551, 1986.

[3] S. Yamamoto, N. Edagawa, H. Taga, Y. Yoshida, H. Wakabayashi, "Analysis of laser phase noise to intensity noise conversion by chromatic dispersion in intensity modulation and direct detection optical-fiber transmission," *J. Lightwave Technol.* vol. 8, no.11, pp. 1716-1722, 1990.

[4] T. Okoshi, "Recent progress in heterodyne/coherent optical fiber communications", *J. Lightwave Technol.*, vol. 2, no. 4, pp. 341-346, Aug. 1984.

[5] T. Minami, "Optical Amplification and Modulation Techniques for Multigigabit IM/DD Long-Haul Transmission Systems", *Technical Digest of ICC'90*, pp. 183-188, 1990.

[6] R. Noé, D. Sandel, M. Yoshida-Dierolf, S. Hinz, V. Mirvoda, A. Schopflin, C. Glingener, E. Gottwald, C. Scheerer, G. Fischer, T. Weyrauch, W. Haase, "Polarization mode dispersion compensation at 10, 20, and 40 Gb/s with various optical equalizers ," *J. Lightwave Technol.*, vol. 17, no. 9, 1602-1616, 1999.

[7] G. Li, "Recent advances in coherent optical communication", *Advances Opt. Photon.*, vol. 1, no. 2, pp. 279-307, 2009.

[8] E. Udd, "An overview of fiber optic sensors", *Rev. Sci. Instrum.*, vol. 66, no. 8 pp. 4015-4030, 1995.

[9] C. E. Campanella, A. Cuccovillo, C. Campanella, A. Yurt and V. M. N. Passaro, "Fibre Bragg Grating based strain sensors: Review of technology and applications", *Sensors*, vol. 18, no. 9, pp. 3115, 2018.

[10] B. Lee, "Review of the present status of optical fiber sensors", *Optical Fiber Technol.*,

vol. 9, no. 2, pp. 57-79, 2003.

[11] J. P. Dakin, D. J. Pratt, G. W. Bibby and J. N. Ross, "Distributed optical fibre Raman temperature sensor using a semiconductor light source and detector", *Electron. Lett.*, vol. 21, no. 13, pp. 569-570, 1985.

[12] A. Ukil, H. Braendle and P. Krippner, "Distributed temperature sensing: Review of technology and applications", *IEEE Sens. J.*, vol. 12, no. 5, pp. 885-892, 2012.

[13] S.M.I. Shatarah and R.Olbrycht, "Distributed temperature sensing in optical fibers based on Raman scattering: theory and applications", *Measur. Automat. Monit.*, vol. 63, no. 2, 2017.

[14] A. Azad, L. Wang, N. Guo, C. Lu, and H. Y. Tam, "Temperature sensing in BOTDA system by using artificial neural network," *Electron. Lett.*, vol. 51, no. 20, pp. 1578–1580, 2015.

[15] Y. S. Muanenda et al., "Advanced Coding Techniques for Long-Range Raman/BOTDA Distributed Strain and Temperature Measurements," *J. Lightwave Technol*., vol. 34, no. 2, pp. 342-350, 2016.

[16] B. Wang, L. Wang, N. Guo, Z. Zhao, C. Yu and C. Lu, "Deep neural networks assisted BOTDA for simultaneous temperature and strain measurement with enhanced accuracy", *Opt. Express*, vol. 27, pp. 2530-2543, 2019.

[17] T. Kurashima, T. Horiguchi, H. Izumita, S. Furukawa and Y. Koyamada, "Brillouin optical-fiber time-domain reflectometry", *IEICE Trans. Commun.*, vol. E76B, no. 4, pp. 382-390, 1993.

[18] K. Shimizu, T. Horiguchi and Y. Koyamada, "Measurement of distributed strain and temperature in a branched optical fiber network by use of Brillouin optical time-domain reflectometry", *Opt. Lett.*, vol. 20, no. 5, pp. 507-509, 1995.

[19] N. Natsuki, M. Tateda and T. Omatsu, "Spatial resolution enhancement in BOTDR by spectrum separation method", *Optical Rev.*, vol. 9, no. 2, pp. 49-53, 2002.

[20] P. J. Winzer and R. J. Essiambre, "Advanced modulation formats for high-capacity

optical transport networks,", *J. Lightwave Technol.,* vol. 24, no. 12, pp. 4711-4728, 2006.

[21] E. Ip and J. M. Kahn, "Digital equalization of chromatic dispersion and polarization mode dispersion," *J. Lightwave Technol.,* vol. 25, no. 8, pp. 2033-2043, 2007.

[22] E. M. Ip and J. M. Kahn, "Fiber Impairment Compensation Using Coherent Detection and Digital Signal Processing," *J. Lightwave Technol.,* vol. 28, no. 4, pp. 502-519, 2010.

[23] S. J. Savory, "Digital coherent optical receivers: Algorithms and subsystems", *IEEE J. Sel. Topics Quantum Electron.*, vol. 16, no. 5, pp. 1164-1179, 2010.

[24] K. Kikuchi, "Fundamentals of Coherent Optical Fiber Communications," *J. Lightwave Technol.,* vol. 34, no. 1, pp. 157-179, 2016.

[25] M. A. Soto and F. Di Pasquale, "Distributed Raman Sensing," in Handbook of Optical Fibers, Springer Nature: Singapore, 2018.

[26] M. A. Soto and L. Thevenaz, "Going beyond limits in Brillouin distributed fibre sensors: Challenges and possible approaches," in *IEEE 5th International Conference on Photonics (ICP)*, pp. 47–52. 2014.

[27] Z. He, and Q. Liu, "Optical Fiber Distributed Acoustic Sensors: A Review," *J. Lightwave Technol.,* 2021.

[28] Y. L. Lu, T. Zhu, L. A. Chen, and X. Y. Bao, "Distributed Vibration Sensor Based on Coherent Detection of Phase-OTDR," *J. Lightwave Technol.,* vol. 28, no. 22, pp. 3243-3249, 2010.

[29] Z. G. Qin, T. Zhu, L. Chen, and X. Y. Bao, "High Sensitivity Distributed Vibration Sensor Based on Polarization-Maintaining Configurations of Phase-OTDR," *IEEE Photon. Technol. Lett.,* vol. 23, no. 15, pp. 1091-1093, 2011.

[30] F. Peng, H. Wu, X. H. Jia, Y. J. Rao, Z. N. Wang, and Z. P. Peng, "Ultra-long high-

sensitivity Phi-OTDR for high spatial resolution intrusion detection of pipelines," *Opt. Express,* vol. 22, no. 11, pp. 13804-10, 2014.

[31] Z. Pan, K. Liang, Q. Ye, H. Cai, R. Qu and Z. Fang, "Phase-sensitive OTDR system based on digital coherent detection", *Proc. SPIE*, vol. 8311, pp. 83110S1-S6, 2011.

[32] S. Wang, X. Y. Fan, Q. W. Liu, and Z. Y. He, "Distributed fiber-optic vibration sensing based on phase extraction from time-gated digital OFDR," *Opt. Express,* vol. 23, no. 26, pp. 33301-33309, 2015.

[33] Z. Wang et al., "Coherent ϕ-OTDR based on I/Q demodulation and homodyne detection," *Opt. Express*, vol. 24, no. 2, pp. 853–858, 2016.

[34] Y. Fu, N. Xue, Z. Wang, B. Zhang, J. Xiong, and Y. Rao, "Impact of I/Q Amplitude Imbalance on Coherent ϕ -OTDR," *J. Lightwave Technol.,* vol. 36, no. 4, pp. 1069-1075, 2018.

[35] J. Jiang et al., "Coherent kramers-kronig receiver for ϕ-OTDR", *J. Lightw. Technol.*, vol. 37, no. 18, pp. 4799-4807, 2019.

[36] A. Mecozzi, C. Antonelli and M. Shtaif, "Kramers-Kronig coherent receiver", *Optica*, vol. 3, no. 11, pp. 1220-1227, 2016.

[37] M. Ren, P. Lu, L. Chen and X. Bao, "Theoretical and experimental analysis of Φ-OTDR based on polarization diversity detection", *IEEE Photon. Technol. Lett.*, vol. 28, no. 6, pp. 697-700, 2016.

[38] Q. Yan, M. Tian, X. Li, Q. Yan and Y. Xu, " Coherent ϕ-OTDR based on polarization-diversity integrated coherent receiver and heterodyne detection ", *Proc. 25th Opt. Fiber Sensors Conf. (OFS)*, pp. 1-4, 2017.

[39] C. Dorize, E. Awwad and J. Renaudier, "High sensitivity φ-OTDR over long distance with polarization multiplexed codes," *IEEE Photon. Technol. Lett.*, vol. 31, no. 20, pp.

1654–1657, 2019.

[40] S. Guerrier, C. Dorize, E. Awwad, and J. Renaudier, "Introducing coherent MIMO sensing, a fading-resilient, polarization-independent approach to ϕ-OTDR," *Opt. Express*, vol. 28, no. 14, pp. 21081–21094, 2020.

[41] M. Dossou, D. Bacquet, and P. Szriftgiser, "Vector Brillouin optical time-domain analyzer for high-order acoustic modes," (in English), *Opt Lett,* vol. 35, no. 22, pp. 3850-3852, Nov 15 2010, doi: Doi 10.1364/Ol.35.003850.

[42] A. Zornoza, M. Sagues, and A. Loayssa, "Self-Heterodyne Detection for SNR Improvement and Distributed Phase-Shift Measurements in BOTDA," *J. Lightwave Technol.,* vol. 30, no. 8, pp. 1066-1072, 2012.

[43] X. Lu, M. A. Soto, M. G. Herraez and L. Thévenaz, "Brillouin distributed fibre sensing using phase modulated probe", *Proc. SPIE*, vol. 8794, pp. 87943P-1-87943P-4, 2013.

[44] J. Urricelqui, M. Sagues, and A. Loayssa, "BOTDA measurements tolerant to non-local effects by using a phase-modulated probe wave and RF demodulation," *Opt. Express,* vol. 21, no. 14, pp. 17186-17194, 2013.

[45] J. Urricelqui, M. Sagues, and A. Loayssa, "Synthesis of Brillouin frequency shift profiles to compensate non-local effects and Brillouin induced noise in BOTDA sensors," *Opt. Express,* vol. 22, no. 15, pp. 18195-18202, 2014.

[46] H. Iribas, J. Urricelqui, J. Mompó, J. Mariñelarena and A. Loayssa, "Non-local effects in Brillouin optical time-domain analysis sensors", *Appl. Sci.*, vol. 7, no. 8, pp. 761, 2017.

[47] X. Tu, Q. Sun, W. Chen, M. Chen and Z. Meng, "Vector Brillouin optical time-domain analysis with heterodyne detection and IQ demodulation algorithm", *IEEE Photon. J.*, vol. 6, no. 2, pp. 1-8, 2014.

[48] Z. L. Li, L. S. Yan, L. Y. Shao, W. Pan, and B. Luo, "Coherent BOTDA sensor with intensity modulated local light and IQ demodulation," *Opt. Express,* vol. 23, no. 12, pp. 16407-16415, 2015.

[49] J. Fang *et al.*, "Complex Brillouin Optical Time-Domain Analysis,"*J. Lightwave Technol.,* vol. 36, no. 10, pp. 1840-1850, 2018.

[50] D. W. Zhou *et al.*, "Slope-assisted BOTDA based on vector SBS and frequency-agile technique for wide-strain-range dynamic measurements," *Opt. Express,* vol. 25, no. 3, pp. 1889-1902, 2017.

[51] G. Y. Yang, X. Y. Fan, and Z. Y. He, "Strain Dynamic Range Enlargement of Slope-Assisted BOTDA by Using Brillouin Phase-Gain Ratio," *J. Lightwave Technol.,* vol. 35, no. 20, pp. 4451-4458, 2017.

[52] H. Zheng *et al.*, "Distributed vibration measurement based on a coherent multi-slope-assisted BOTDA with a large dynamic range," *Opt. Lett.,* vol. 44, no. 5, pp. 1245-1248, 2019.

[53] R. Bernini, A. Minardo, and L. Zeni, "Dynamic strain measurement in optical fibers by stimulated Brillouin scattering," *Opt. Lett.,* vol. 34, no. 17, pp. 2613-2615, 2009.

[54] A. Lopez-Gil, A. Dominguez-Lopez, S. Martin-Lopez, and M. Gonzalez-Herraez, "Simple Method for the Elimination of Polarization Noise in BOTDA Using Balanced Detection and Orthogonal Probe Sidebands," *J. Lightwave Technol.,* vol. 33, no. 12, pp. 2605-2610, 2015.

[55] A. Loayssa, F. Lopez-Fernandino, J. Urricelqui, and M. Sagues, "Polarization Diversity Scheme for BOTDA Sensors Based on a Double Orthogonal Pump Interaction," *J. Lightwave Technol.,* vol. 33, no. 12, pp. 2633-2638, 2015.

[56] L. Wang *et al.*, "Coherent BOTDA Using Phase- and Polarization-Diversity Heterodyne Detection and Embedded Digital Signal Processing," *IEEE Sensors*

Journal, vol. 17, no. 12, pp. 3728-3734, 2017.

[57] C. Jin *et al.*, "Scanning-free BOTDA based on ultra-fine digital optical frequency comb," *Opt. Express,* vol. 23, no. 4, pp. 5277-5284, 2015.

[58] C. Jin *et al.*, "Single-measurement digital optical frequency comb based phase-detection Brillouin optical time domain analyzer," *Opt. Express,* vol. 25, no. 8, pp. 9213-9224, 2017.

[59] J. Fang, W. Shieh and P. Xu, "Single-shot Brillouin optical time domain analysis for distributed fiber sensing", *Proc. IEEE Conf. Sens.*, pp. 1-3, 2016.

[60] J. Fang, P. Xu, Y. Dong, and W. Shieh, "Single-shot distributed Brillouin optical time domain analyzer," *Opt. Express,* vol. 25, no. 13, pp. 15188-15198, 2017.

[61] C. Zhao *et al.*, "BOTDA using channel estimation with direct-detection optical OFDM technique," *Opt. Express,* vol. 25, no. 11, pp. 12698-12709, 2017.

[62] C. Zhao, M. Tang, R. Liao, H. Wu and S. Fu, "SNR-enhanced fast BOTDA combining channel estimation technique with complementary pulse coding", *IEEE Photon. J.*, vol. 10, no. 5, Oct. 2018.

[63] C. Pan, X. R. Liu, H. Zhu, X. K. Shan, and X. H. Sun, "Distributed optical fiber vibration sensor based on Sagnac interference in conjunction with OTDR," *Opt. Express,* vol. 25, no. 17, pp. 20056-20070, 2017.

[64] H. He *et al.*, "Multiple vibrations measurement using phase-sensitive OTDR merged with Mach-Zehnder interferometer based on frequency division multiplexing," *Opt. Express,* vol. 24, no. 5, pp. 4842-4855, 2016.

[65] S. Liang, X. Sheng, S. Lou, Y. Feng and K. Zhang, "Combination of phase-sensitive OTDR and michelson interferometer for nuisance alarm rate reducing and event identification", *IEEE Photon. J.*, vol. 8, no. 2, pp. 1-2, 2016.

[66] X. L. Li, Q. Z. Sun, J. H. Wo, M. L. Zhang, and D. M. Liu, "Hybrid TDM/WDM-Based Fiber-Optic Sensor Network for Perimeter Intrusion Detection," *J. Lightwave Technol.,* vol. 30, no. 8, pp. 1113-1120, 2012.

[67] M. Kondrat, M. Szustakowski, N. Pałka, W. Ciurapiński and M. Życzkowski, "A Sagnac-Michelson fibre optic interferometer: Signal processing for disturbance localization", *Opto-Electron. Rev.*, vol. 15, no. 3, pp. 127-132, 2007.

[68] T. Zhu, Q. He, X. H. Xiao, and X. Y. Bao, "Modulated pulses based distributed vibration sensing with high frequency response and spatial resolution," *Opt. Express,* vol. 21, no. 3, pp. 2953-2963, 2013.

[69] Y. Shi, H. Feng and Z. M. Zeng, "Distributed fiber sensing system with wide frequency response and accurate location", *Opt. Lasers Eng.*, vol. 77, pp. 219-224, 2016.

[70] J. H. Park, W. K. Lee and H. F. Taylor, "A fiber optic intrusion sensor with the configuration of an optical time domain reflectometer using coherent interference of Rayleigh backscattering", *Proc. SPIE*, vol. 3555, pp. 49-56, 1998.

[71] J. C. Juarez, E. W. Maier, K. N. Choi, and H. F. Taylor, "Distributed fiber-optic intrusion sensor system," *J. Lightwave Technol.,* vol. 23, no. 6, pp. 2081-2087, 2005.

[72] J. C. Juarez and H. F. Taylor, "Field test of a distributed fiber-optic intrusion sensor system for long perimeters," *Appl. Optics,* vol. 46, no. 11, pp. 1968-1971, 2007.

[73] Z. Y. Zhang and X. Y. Bao, "Distributed optical fiber vibration sensor based on spectrum analysis of Polarization-OTDR system,", *Opt. Express,* vol. 16, no. 14, pp. 10240-10247, 2008.

[74] N. Linze, P. Megret and M. Wuilpart, "Development of an intrusion sensor based on a polarization-OTDR system", *IEEE Sens. J.*, vol. 12, no. 10, pp. 3005-3009, 2012.

[75] Q. Cui, S. Pamukcu, W. Xiao and M. Pervizpour, "Truly distributed fiber vibration

sensor using pulse base BOTDA with wide dynamic range", *IEEE Photon. Technol. Lett.*, vol. 23, no. 24, pp. 1887-1889, 2011.

[76] Y. Peled, A. Motil, I. Kressel, and M. Tur, "Monitoring the propagation of mechanical waves using an optical fiber distributed and dynamic strain sensor based on BOTDA," *Opt Express,* vol. 21, no. 9, pp. 10697-10705, 2013.

[77] M. Taki, Y. Muanenda, C. J. Oton, T. Nannipieri, A. Signorini, and F. Di Pasquale, "Cyclic pulse coding for fast BOTDA fiber sensors," *Opt. Lett.,* vol. 38, no. 15, pp. 2877-2880, 2013.

[78] X. Liu, B. Jin, Q. Bai, Y. Wang, D. Wang and Y. Wang, "Distributed fiber-optic sensors for vibration detection", Sensors, vol. 16, pp. 1164, Jul. 2016.

[79] D. W. Stowe, D. R. Moore and R. G. Priest, "Polarization fading in fiber interferometric sensors", *IEEE J. Quantum Electron.*, vol. 18, no. 10, pp. 1644-1647, 1982.

[80] A. D. Kersey, M. J. Marrone, and M. A. Davis, "Statistical Modeling of Polarization Induced Fading in Interferometric Fiber Sensors," *Electronics Letters,* vol. 27, no. 6, pp. 481-483, 1991.

[81] A. Dandridge, A. B. Tveten, and T. G. Giallorenzi, "Homodyne demodulation scheme for fiber optic sensors using phase generated carrier," *IEEE J. Quantum Electron.*, vol. 18, no. 10, pp. 1647–1653, 1982.

[82] Y. Li, Z. B. Liu, Y. Liu, L. Ma, Z. W. Tan, and S. S. Jian, "Interferometric vibration sensor using phase-generated carrier method," *Appl. Optics,* vol. 52, no. 25, pp. 6359-6363, 2013.

[83] K. P. Koo, A. B. Tveten, and A. Dandridge, "Passive Stabilization Scheme for Fiber Interferometers Using (3x3) Fiber Directional-Couplers," *Appl. Phys. Lett.,* vol. 41, no. 7, pp. 616-618, 1982.

[84] Q. Z. Sun, D. M. Liu, H. Wang, and H. R. Liu, "Distributed fiber-optic vibration sensor using a ring Mach-Zehnder interferometer," *Opt. Commun.,* vol. 281, no. 6, pp. 1538-1544, 2008.

[85] B. Chiu and M. C. Hastings, "Digital demodulation for passive homodyne optical fiber interferometry based on a 3 x3 coupler," *Proc. SPIE*, vol. 2292, pp. 371-382, 1994.

[86] S. J. Spammer, A. A. Chtcherbakov and P. L. Swart, "Distributed dual wavelength Sagnac impact sensor", *Microw. Opt. Technol. Lett.*, vol. 17, no. 3, pp. 170-173, 1998.

[87] J. P. Dakin, D. A. J. Pearce, A. P. Strong and C. A. Wade, "A novel distributed fiber sensing system enabling location of disturbances in a Sagnac loop interferometer", *Proc. SPIE*, vol. 838, pp. 325-328, 1987.

[88] S. J. Russell, K. R. C. Brady, and J. P. Dakin, "Real-time location of multiple time-varying strain disturbances, acting over a 40-km fiber section, using a novel dual-Sagnac interferometer," *J. Lightwave Technol.,* vol. 19, no. 2, pp. 205-213, 2001.

[89] W. W. Lin, "Novel distributed fiber optic leak detection system", *Opt. Eng.*, vol. 43, no. 2, pp. 278-279, 2004.

[90] S. J. Spammer, P. L. Swart, and A. Booysen, "Interferometric distributed optical-fiber sensor," *Appl. Optics,* vol. 35, no. 22, pp. 4522-4525, 1996.

[91] B. J. Vakoc, M. J. F. Digonnet, and G. S. Kino, "Demonstration of a folded Sagnac sensor array immune to polarization-induced signal fading," *Appl. Optics,* vol. 42, no. 36, pp. 7132-7136, 2003.

[92] W. Yuan, B. Pang, J. Bo and X. Qian, "Fiber-optic sensor without polarization-induced signal fading", *Microw. Opt. Technol. Lett.*, vol. 56, no. 6, pp. 1307-1313, 2014.

[93] G. Luo, et al. , "Distributed fiber optic perturbation locating sensor based on dual Mach-Zehnder interferometer.," *International Symposium on Photoelectronic Detection and*

Imaging 2007: Laser, Ultraviolet, and Terahertz Technology. Vol. 6622. International Society for Optics and Photonics, 2008.

[94] C. Y. Ma *et al.*, "Long-Range Distributed Fiber Vibration Sensor Using an Asymmetric Dual Mach-Zehnder Interferometers," *J. Lightwave Technol.,* vol. 34, no. 9, pp. 2235-2239, 2016.

[95] D. Tu, S. Xie, Z. Jiang and M. Zhang, "Ultra long distance distributed fiber-optic system for intrusion detection", *Proc. SPIE*, vol. 8561, 2012.

[96] S. R. Xie, Q. L. Zou, L. W. Wang, M. Zhang, Y. H. Li, and Y. B. Liao, "Positioning Error Prediction Theory for Dual Mach-Zehnder Interferometric Vibration Sensor," *J. Lightwave Technol.,* vol. 29, no. 3, pp. 362-368, 2011,.

[97] Q. N. Chen *et al.*, "An Elimination Method of Polarization-Induced Phase Shift and Fading in Dual Mach-Zehnder Interferometry Disturbance Sensing System," *J. Lightwave Technol.,* vol. 31, no. 19, pp. 3135-3141, 2013.

[98] Q. N. Chen *et al.*, "An Improved Positioning Algorithm With High Precision for Dual Mach-Zehnder Interferometry Disturbance Sensing System," *J. Lightwave Technol.,* vol. 33, no. 10, pp. 1954-1960, 2015.

[99] X. B. Hong, J. Wu, C. Zuo, F. S. Liu, H. X. Guo, and K. Xu, "Dual Michelson interferometers for distributed vibration detection," *Appl. Optics,* vol. 50, no. 22, pp. 4333-4338, 2011.

[100] Q. M. Chen *et al.*, "A distributed fiber vibration sensor utilizing dispersion induced walk-off effect in a unidirectional Mach-Zehnder interferometer," *Opt. Express,* vol. 22, no. 3, pp. 2167-2173, 2014.

[101] B. R. W., "Nonlinear optics," Academic Press, 2008. 391-393.

[102] M. Nakazawa, "Rayleigh backscattering theory for single-mode optical fibers", *J. Opt.*

Soc. Amer., vol. 73, no. 9, pp. 1175-1180, 1983.

[103] M. K. Barnoski and S. M. Jensen, "Fiber waveguides: A novel technique for investigating attenuation characteristics", *Appl. Opt.*, vol. 15, no. 9, pp. 2112-2115, 1976.

[104] P. Healey, "Fading in heterodyne OTDR", *Electron. Lett.*, vol. 20, no. 1, pp. 30-32, 1984.

[105] K. Aoyama, K. Nakagawa and T. Itoh, "Optical time domain reflectometry in a single-mode fiber", *IEEE J. Quantum Electron.*, vol. 17, NO. 6, pp. 862-868, 1981.

[106] G. Ripamonti, M. Ghioni, and A. Lacaita, "No Dead-Space Optical Time-Domain Reflectometer," *J. Lightwave Technol.*, vol. 8, no. 9, pp. 1278-1283, 1990.

[107] R. W. Boyd, Chapter 9, Nonlinear Optics, third edition [M]. 2009.

[108] A. Motil, A. Bergman and M. Tur, "State of the art of Brillouin fiber-optic distributed sensing", *Opt. Laser Technol.*, vol. 78, no. Part A, pp. 81-103, 2016.

[109] K. Shimizu, T. Horiguchi, Y. Koyamada, and T. Kurashima, "Coherent Self-Heterodyne Brillouin Otdr for Measurement of Brillouin Frequency-Shift Distribution in Optical Fibers," *J. Lightwave Technol.,* vol. 12, no. 5, pp. 730-736, 1994.

[110] X. Bao, J. Dhliwayo, N. Heron, D. J. Webb, and D. A. Jackson, "Experimental and Theoretical-Studies on a Distributed Temperature Sensor-Based on Brillouin-Scattering," *J. Lightwave Technol.,* vol. 13, no. 7, pp. 1340-1348, 1995.

[111] Y. Koyamada, Y. Sakairi, N. Takeuchi and S. Adachi, "Novel technique to improve spatial resolution in Brillouin optical time-domain reflectometry", *IEEE Photon. Technol. Lett.*, vol. 19, no. 23, pp. 1910-1912, 2007.

[112] Q. Bai *et al.*, "Recent advances in Brillouin optical time domain reflectometry", *Sensors*, vol. 19, no. 8, P. 1862, 2019.

[113] T. Horiguchi and M. Tateda, "BOTDA-Nondestructive measurement of single-mode optical fiber attenuation characteristics using Brillouin interaction: Theory", *J. Lightwave Technol.*, vol. 7, no. 8, pp. 1170-1176, 1989.

[114] C. A. Galindez-Jamioy and J. M. Lopez-Higuera, "Brillouin distributed fiber sensors: An overview and applications", *J. Sensors*, vol. 2012, pp. 204121-204121, 2012.

[115] D. X. Ba *et al.*, "Distributed measurement of dynamic strain based on multi-slope assisted fast BOTDA," *Opt. Express,* vol. 24, no. 9, pp. 9781-9793, 2016.

[116] Z. H. Liang *et al.*, "Spatial resolution improvement of single-shot digital optical frequency comb-based Brillouin optical time domain analysis utilizing multiple pump pulses," *Opt. Lett.,* vol. 43, no. 15, pp. 3534-3537, 2018.

[117] D. Zhou et al., "Single-shot BOTDA based on an optical chirp chain probe wave for distributed ultrafast measurement", *Light Sci. Appl.*, vol. 7, no. 1, p. 32, 2018.

[118] Y. K. Dong *et al.*, "150 km fast BOTDA based on the optical chirp chain probe wave and Brillouin loss scheme," *Opt. Lett.,* vol. 43, no. 19, pp. 4679-4682, 2018.

[119] J. D. Zhang, H. Zheng, H. T. Wu, N. Guo, G. L. Yin, and T. Zhu, "Vector optical-chirp-chain Brillouin optical time-domain analyzer based on complex principal component analysis," *Opt. Express,* vol. 28, no. 20, pp. 28831-28842, 2020.

[120] S. A. Nezamalhosseini, L. R. Chen, Q. Zhuge, M. Malekiha, F. Marvasti, and D. V. Plant, "Theoretical and experimental investigation of direct detection optical OFDM transmission using beat interference cancellation receiver," *Opt. Express,* vol. 21, no. 13, pp. 15237-15246, 2013.

[121] W. R. Peng *et al.*, "Spectrally efficient direct-detected OFDM transmission employing an iterative estimation and cancellation technique," *Opt. Express,* vol. 17, no. 11, pp. 9099-9111, 2009.

[122] Q. H. Song, H. K. Peng, S. F. Zhou, P. W. Zhou, Q. Xiao, and B. Jia, "A Novel Weak-Scattering Michelson Interferometer Based on PBS for Long-Distance Disturbance Localization," *J. Lightwave Technol.,* vol. 38, no. 6, pp. 1543-1549, 15 2020.

[123] Z. Y. Zhao, M. Tang, L. Wang, N. Guo, H. Y. Tam, and C. Lu, "Distributed Vibration Sensor Based on Space-Division Multiplexed Reflectometer and Interferometer in Multicore Fiber," *J. Lightwave Technol.,* vol. 36, no. 24, pp. 5764-5772, 2018.

[124] S. L. Jansen, I. Morita, T. C. W. Schenk and H. Tanaka, "121.9-Gb/s PDM-OFDM transmission with 2-b/s/Hz spectral efficiency over 1000 km of SSMF", *J. Lightwave Technol.*, vol. 27, no. 3, pp. 177-188, 2009.

[125] W. Shieh, Q. Yang, and Y. Ma, "107 Gb/s coherent optical OFDM transmission over 1000-km SSMF fiber using orthogonal band multiplexing," *Opt. Express,* vol. 16, no. 9, pp. 6378-6386, 2008.

[126] D. S. Ly-Gagnon, K. Katoh and K. Kikuchi, "Unrepeatered optical transmission of 20 Gb/s quadrature phase-shift keying signals over 210 km using homodyne phase-diversity receiver and digital signal processing", *Electron. Lett.*, vol. 41, no. 4, pp. 59-60, 2005.

[127] J. Dong, J. C. Huang, T. Li, and L. Liu, "Observation of fundamental thermal noise in optical fibers down to infrasonic frequencies," *Appl. Phys. Lett.,* vol. 108, no. 2, p. 021108, 2016.

[128] L. Duan, "Thermal noise-limited fiber-optic sensing at infrasonic frequencies", *IEEE J. Quantum Electron.*, vol. 51, no. 2, pp. 1-6, 2015.

[129] J. P. Iannello, "Time delay estimation via cross-correlation in the presence of large estimation errors", *IEEE Trans. Acoust. Speech Signal Process.*, vol. ASSP-30, pp. 998-1003, 1982.

[130] G. Marra et al., "Ultrastable laser interferometry for earthquake detection with

terrestrial and submarine cables", *Science*, vol. 361, no. 6401, pp. 486-496, 2018.

[131] H. Wang, Q. Z. Sun, X. L. Li, J. H. Wo, P. P. Shum, and D. M. Liu, "Improved location algorithm for multiple intrusions in distributed Sagnac fiber sensing system," *Opt. Express,* vol. 22, no. 7, pp. 7587-7597, 2014.

[132] M. R. D. Rodrigues and I. Darwazeh, "A spectrally efficient frequency division multiplexing based communication system", *Proc. Int. OFDM Workshop*, pp. 48-49, 2003.

[133] I. Darwazeh, T. Xu, T. Gui, Y. Bao and Z. Li, "Optical SEFDM system; bandwidth saving using non-orthogonal sub-carriers", *IEEE Photon. Technol. Lett.*, vol. 26, no. 4, pp. 352-355, 2014.

[134] B. X. Yu *et al.*, "150-Gb/s SEFDM IM/DD transmission using log-MAP Viterbi decoding for short reach optical links," *Opt. Express,* vol. 26, no. 24, pp. 31075-31084, 2018.

[135] I. Barhumi, G. Leus and M. Moonen, "Optimal training design for MIMO OFDM systems in mobile wireless channels", *IEEE Trans. Signal Process.*, vol. 51, no. 6, pp. 1615-1624, 2003.

[136] Y. S. Shinakov, "Ambiguity functions of zadoff-chu signals for 5-g synchronization systems", *2018Systems of Signal Synchronization Generating and Processing in Telecommunications (SYNCHROINFO)*, pp. 1-7, 2018.

[137] C.-L. Wang, H.-C. Wang, and Y.-Y. Chen, "A synchronization scheme based on partial Zadoff-Chu sequences for cooperative MIMO OFDM systems, " in *Proc. 2012 IEEE Wireless Communications and Networking Conference (WCNC 2012)*, Paris, France, 2012.

[138] M. Nazarathy, S. A. Newton, R. P. Giffard, D. S. Moberly, F. Sischka, W. R. Trutna Jr., et al., "Real-time long range complementary correlation optical time domain

reflectometer", *J. Lightwave Technol.*, vol. 7, no. 1, pp. 24-38, 1989.